In compliance with the
Canadian Privacy Legislation
some supporting forms
may have been removed from
this dissertation.

While these forms may be included
in the document page count,
their removal does not represent
any loss of content from the dissertation.

Design and Behavioural Control of a Dynamic Quadruped with Active Wheels

Charles F. Steeves III

Department of Mechanical Engineering

McGill University, Montreal, Canada

November 2002

A thesis submitted to the Faculty of Graduate Studies and Research in partial fulfillment of the requirements of the degree of

Master of Engineering

© Charles F. Steeves III, 2002

National Library of Canada

Acquisitions and Bibliographic Services

395 Wellington Street
Ottawa ON K1A 0N4
Canada

Bibliothèque nationale du Canada

Acquisisitons et services bibliographiques

395, rue Wellington
Ottawa ON K1A 0N4
Canada

Your file Votre référence
ISBN: 0-612-88388-4
Our file Notre référence
ISBN: 0-612-88388-4

The author has granted a non-exclusive licence allowing the National Library of Canada to reproduce, loan, distribute or sell copies of this thesis in microform, paper or electronic formats.

The author retains ownership of the copyright in this thesis. Neither the thesis nor substantial extracts from it may be printed or otherwise reproduced without the author's permission.

L'auteur a accordé une licence non exclusive permettant à la Bibliothèque nationale du Canada de reproduire, prêter, distribuer ou vendre des copies de cette thèse sous la forme de microfiche/film, de reproduction sur papier ou sur format électronique.

L'auteur conserve la propriété du droit d'auteur qui protège cette thèse. Ni la thèse ni des extraits substantiels de celle-ci ne doivent être imprimés ou aturement reproduits sans son autorisation.

Canada

Abstract

To capitalize on the efficiency and simplicity of wheeled robots, as well as the adaptability and maneuverability of legged robots, many hybrid leg-wheel designs have been developed. To date, none of these platforms have possessed the ability to execute dynamic maneuvers and thus have major shortcomings in their speed, efficiency and obstacle negotiating capabilities. A hybrid leg-wheel quadruped capable of such dynamic behaviour is introduced. Using an accurate model of this platform, a variety of dynamic behaviours and examples of their utility were successfully simulated. Passive leg compliance and the placement of wheels at the foot of the legs proved invaluable in achieving such high energy maneuvers on this power autonomous platform. A full systems design of a testbed capable of executing the presented dynamic behaviour was completed. From both a mechanical and control stand-point, it is a simple and robust robot. This prototype will prove the feasibility of such behavioural feats for autonomously powered platforms, demonstrate their wide utility and pave the way for their realization on ruggedized platforms.

Résumé

Pour profiter de l'efficacité et de la simplicité des robots à roues, aussi bien que de l'adaptabilité et de la manoeuvrabilité des robots marcheurs, beaucoup de conceptions hybrides de jambe et de roue ont été développées. Jusqu'ici, aucun de ces plateformes n'a possédé la capacité d'exécuter des manoeuvres dynamiques et ils ont ainsi des imperfections principales dans leurs capacités de vitesse, d'efficacité et de négociation des obstacles. Une quadrupède marcheur avec des roues capable d'un tel comportement dynamique est présentée. En utilisant le modèle précis de ce système, une variété de fonctionnements dynamiques ont été simulés. La souplesse passive des jambes et le placement des roues au pied des jambes ont été très important pour la réalisation de ces manoeuvres à énergie élevée. Une conception d'un banc d'essai capable d'exécuter le comportement dynamique présenté a été compléter. Des points de vue mécanique et de contrôle, c'est un robot simple et robuste. Ce prototype prouvera la praticabilité des fonctionnements dynamiques pour les systèmes autonomes, démontra leur utilité, et ouvrira la voie à d'autres systèmes plus robustes.

Acknowledgments

I would like to thank and extend my appreciation to the following people for their support throughout the course of my research.

- Professor Martin Buehler, my supervisor, for his guidance, criticism and support throughout my degree. His knowledge of robotics, particularly legged locomotion, has been invaluable to both my research and my personal exploration of this field. I especially thank him for the frequent encouragement and wise perspectives that often refuelled my motivation and curiosity.
- Dr. Chris Brosinsky for setting up and fostering McGill's partnership with DRES for the ANT project and Steve Penzes for his informative advice on simulation modelling and for his guidance in directing the project to its successful completion.
- James Smith for his unwavering fairness and exceptional soft skills that respond to the concerns of any ARL member with communally pleasing solutions, every time. Without exception, he has never been *"too busy"* to address my questions with an articulated and refreshingly humble response. I also thank him for carefully proofreading parts of this thesis.
- Ioannis Poulakakis for his partnership in the course projects, the many mathematics lessons, help with the dynamic model and for his pleasant company as my night comrade.
- Evgeni Kiriy for maintaining the ARL computer network and sharing his laughter during those long nights.

- Dave McMordie, the other green racer, for all his electronic assistance, for developing the motor driver board and for always being up for a stimulating argument.
- Don Campbell for his patient help with anything electrical, especially the PC stack and the I/O card, as the electronic design of the prototype was made possible with his efforts.
- Matt Smith, whom I cannot thank enough for his invaluable mechanical advice. I am indebted to his tremendous design talents on so many aspects of the prototype. He also helped me break up those long days with breaks of *fresh air*.
- Genvieve Vinois, our lab administrator, for keeping the lab running smoothly and allowing us to pretend that paperwork doesn't exist.
- Jan Binder and Danny Chouinard, the CIM systems administrators, for maintaining the computer network at CIM so we can focus on our research.
- Marlene Gray and Cynthia Davidson, the CIM administration staff, for keeping CIM operating smoothly and acting as our liaison to the slow bureaucracy.
- Chris Prahacs for all his SolidWorks help.
- Ned Moore, Gish Abou-Samah and Aki Sato for bouncing around ideas and making the lab a more interesting place to work.
- Christine Georgiadis and Neil Neville for carefully proofreading parts of this thesis.

Most of all, I would like to thank my parents for their unconditional love and support, especially over the duration of my degree. They have always stood by me and have been willing to help in any way they can. I thank them for always believing in me and for helping me to keep my spirits high.

Table of Contents

List of Figures

List of Tables

Dedicated to my parents.

Chapter 1

Introduction

1.1. Overview and Motivation

The ultimate goal of the field of robotics is to develop machines capable of duplicating, or even surpassing, humans' interaction with their environment. Such machines have a wide range of application ranging from eliminating the human element in menial tasks to removing humans from dangerous workplaces. Under the umbrella of this broad discipline is the field of mobile robotics, which concentrates on developing highly autonomous platforms that embody high mobility in even the most unstructured environments. Towards this end, an exhaustive number of wheeled and tracked robots have been developed. These platforms are favourable attempts owing to their simplicity, power efficiency and most of all, their inherent static stability. However, even after many years of maturity, these machines still fall short of the mobility of humans or animals.

The relatively young field of legged robotics is working to exploit the maneuverability and dexterity of legs to traverse highly unstructured terrain. Although still in its infancy, the research in this discipline has had sufficient success to demonstrate the substantial increases in mobility gained through the implementation of legs. Imitating the superior terrain negotiating capabilities of animals has not yet been realized, but the field is steadily progressing towards this goal as the many researchers focus on various subsets of the enormous array of hurdles.

There are many quadruped animals that have ideal mobility traits, thus a large number of quadruped robots have been built in an effort to emulate nature's proven techniques. An attractive aspect of such a platform is that they can achieve static stability by planting at least three of their legs on the ground and maintaining their center of mass over this three leg tripod. With such a gait, the robot may stop and hold its position at any instant of its execution without losing stability. These robots are inherently slow and have poor power efficiencies not only from the requirement of static stability, but also owing largely to the many degrees of freedom in their legs. Their legs' complexity, coupled with the large mass of many actuators, limit the robot's behaviour and lend the robots to frequent breakdowns.

To realize faster speeds, increase efficiency and to widen the scope of negotiable obstacles, legged robots capable of dynamic motion were developed. Dynamically stable platforms are designed to maintain stability even when the center of mass is outside the area of support formed by the legs contacting the ground. Although the motion or gait is stable as a whole, each of the phases that constitute the cyclic motion may be unstable. As such, these robots are not able to simply stop and hold their position during the execution of a dynamic gait without losing stability, making their control much more difficult. However, these gaits often contain flight phases, which enables faster speeds and the ability to jump or leap. Thus, a smaller robot with dynamic capabilities can use its kinetic energy to increase its effective size and outperform a larger platform. Generally speaking, dynamic robots mimic animal behaviour more closely and have increased mobility due to less restrictive movements. However, these behaviours usually require the expenditure of large amounts of energy, making them difficult to implement on an untethered, autonomously powered platform.

To capitalize on the efficiency and simplicity of wheeled robots, as well as the adaptability and maneuverability of legged robots, many hybrid leg-wheel designs have been developed. However, these platforms have been rather bulky, complex machines that traverse terrain quite slowly. To date, none of them have been able to venture into the dynamic realm and thus have major shortcomings in their speed, efficiency and obstacle negotiating capabilities. The focus of this research was to develop a means for hybrid leg-wheel platforms to realize dynamic maneuvers, as well as to design a testbed that could demonstrate these highly energetic behaviours. The work also had a more generalized target of expanding the currently narrow scope of feasible dynamic behaviour for autonomously powered platforms. From both a mechanical and control stand-point, it was aimed to develop a simple and robust robot. With high reliability and power autonomy, it will allow the platform to be easily adopted for *real world* operation.

1.2. Background

The first section below is an overview of the many hybrid leg-wheel robots that have been developed. It is meant to outline the development of these machines, from their introduction to the present, to give an overall impression of their progress in the context of mobile robotics. It should also be apparent that none of these robots have been able to venture into the dynamic realm. The second section provides background on dynamic quadrupeds. Specifically, the section addresses the other quadrupeds' behavioural capabilities so as to place the performance increases with the active wheel, introduced here, in context. The last section is a brief history of the Ambulatory Robotics Lab (ARL), which is included because the platform presented in this work is a successor of the ideas, concepts and robots previously developed at the ARL.

1.2.1. Hybrid Leg-Wheel Platforms

High cross-country ability and maneuverability are the major requirements for mobile robots intended for operation on natural terrain. Many wheeled and tracked platforms have been developed in an attempt to satisfy these requirements, but a few decades ago many researchers began investigating alternative means of locomotion to obtain higher mobility. Researchers realized that while legged platforms have good terrain negotiating capability, wheeled locomotion was more efficient at higher speeds. By combining legged and wheeled locomotion, they aimed to gain effective natural terrain mobility with a large velocity range. These hybrid machines have the potential of improved stability over rugged terrain, since the wheels can maintain contact with the ground for a large percentage of the time. The following material summarizes the progression of the hybrid concept and will familiarize the reader with their current level of development.

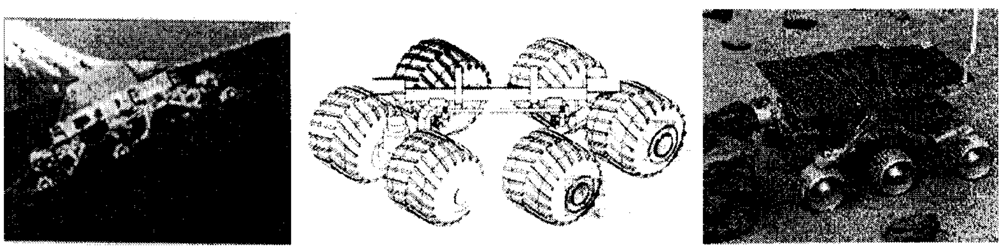

Fig 1.1. Planetary explorer (left), Polar Rover Chassis (center) and Mars Pathfinder (right).

Many leg-wheel platforms have been developed within the framework of arctic and planetary exploration (i.e. Earth, Mars). Fig 1.1.left shows a six-wheeled experimental mock-up with a 320 kg rigid frame, utilizing a Chebyshev mechanism [1]. It is able to move in wheel-walking modes with continuous or discontinuous walking (wheel mode - 0.9 km/hr, walking mode - 0.15 km/hr). Since 1995, the polar rover chassis (Fig. 1.1.center) has been a widely adopted platform for artic exploration [1][2]. The Mars Pathfinder, shown in Fig 1.1.right, is probably the most widely recognized hybrid platform as its operation on Mars was broadcasted internationally over many days [3]. Most of the planetary rovers use novel kinematic mechanisms to passively adapt to the terrain and are still quite far from merging true legged locomotion into the platforms.

As early as 1982, Ichikawa developed a five-legged machine for the purpose of remote maintenance in nuclear power plants [4]. Seen in Figure 1.2, the robot had five legs actuated with screw shafts and steerable driving wheels. The wheels were located such that any four could hold static stability. Touch sensors on the leg, as well as slope sensors, enabled stepping over obstacles, going up and down stairs (100 mm height, 150 mm depth) and maintaining stability on slopes. Route planning and obstacle geometry were downloaded to the robot from an operator. In 1984, Oomichi proposed a 14 DOF design with four legs and six wheels – four on the ends of corresponding legs and two on the active body joint (Fig. 1.3) [5]. The prototype built for Mitsubishi Heavy Industries Ltd. successfully negotiated uneven ground and stairs. In 1988, Belforte introduced a platform (Fig. 1.4) that also successfully climbed over obstacles and moved up and down stairs [6]. It was an octopod that had four legs with wheels (two driven, two passive) and two additional couples of legs. The wheels were actuated with D.C. motors while the legs used pneumatic cylinders for lifting. The robot could reach a maximum speed of 0.3 m/s and could climb a typical staircase (300 mm height, 150 mm depth).

In 1991, Kimura developed a *disaster preventing* robotic platform for Kobe Steel Ltd. under the auspices of the Advanced Robot Technology Research Association (Fig. 1.5) [7]. It was designed to operate in extreme environments (high temperature and radiation) and was equipped with two manipulator arms. The 600 kg robot had six legs with two degrees of freedom (thigh and knee joint) and was equipped with a steering and wheel drive. The prototype moved at a maximum speed of 10 km/h (wheel mode) and the time required for stepping over an obstacle (250 mm height, 225 mm width) was 17.6 seconds. The support vehicle and the robot were connected via a fireproof cable used for communication and power supply. The research and development was concluded at the elemental development stage for reasons relating to the downsizing of the platform.

Developed by Hirose at the Tokyo Institute of Technology (1996 to present), the Roller-Walker (Fig. 1.6) achieves wheeled locomotion by *roller skating* with passive wheels [8]. Hirose fitted the TITAN VIII robot with special foot mechanisms that rotate 90 degrees to change from a sole for walking to a passive wheel for skating. Two legs powered the skating while braking was achieved by changing the tangential angle of the wheels. The entire robot weighed approximately 24 kg. and reached a speed of 0.8 m/s in skating mode – doubling TITAN VIII's walking speed. Although it was successfully implemented, it had low energy efficiency due to the cyclic thrusting required to skate.

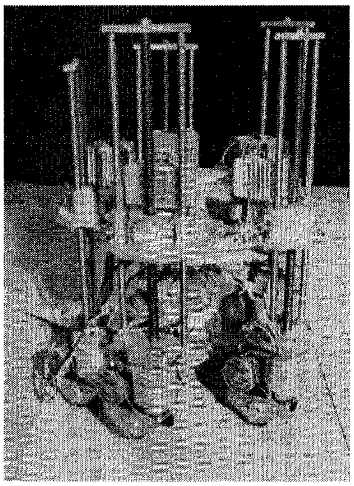

Fig. 1.2. Ichikawa's hybrid (1982).

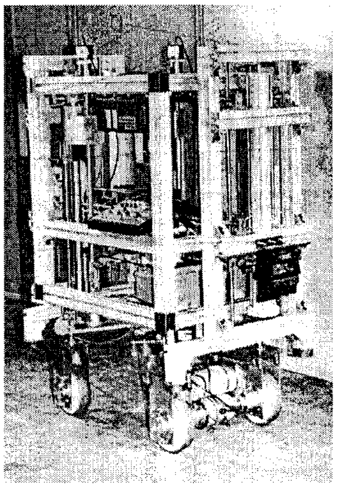

Fig. 1.4. Belforte's prototype (1988).

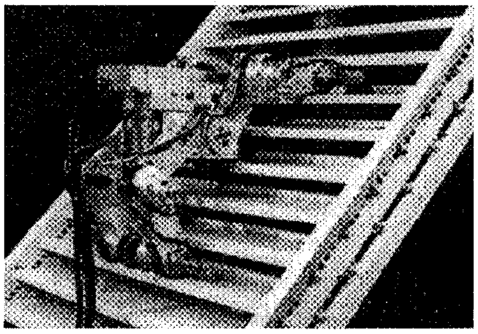

Fig. 1.3. Oomichi's prototype (1984).

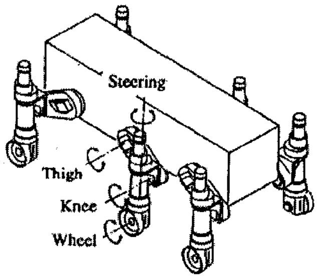

Fig. 1.5. Kimura's prototype (1991).

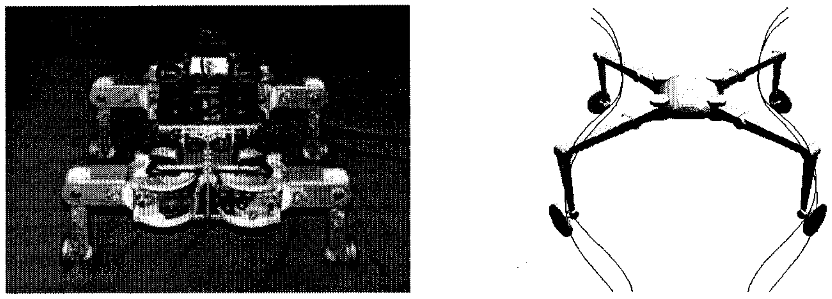

Fig. 1.6. Hirose's Roller-Walker (1996).

In 1999, Adachi designed a mobile outdoor robot called Walk'n Roll [9]. This robot's front legs have three joints and a passive wheel while the rear legs have one joint and an active wheel (Fig. 1.7). An operator controls the majority of robot's motion with two joysticks (speed & direction) and an autonomous step controller.

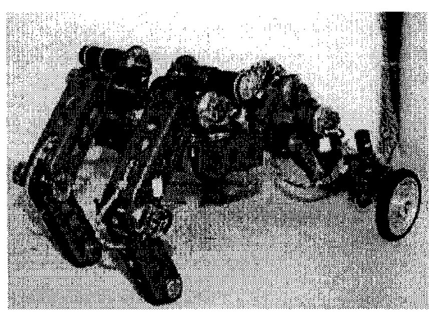

Fig. 1.7. Adachi's Walk'n Roll (1999).

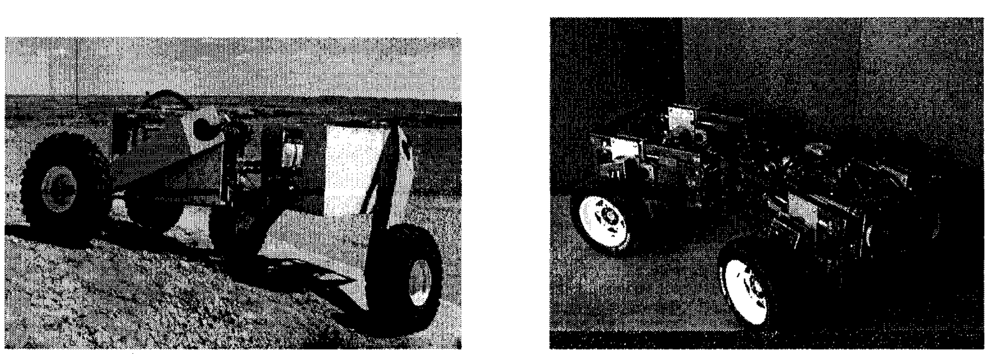

Fig. 1.8. DRES's ANT Testbeds (early '90's left, late '90's right).

In the early 1990's, the Defence Research Establishment Suffield (DRES) under the Canadian Defence R&D program, began to develop an Articulated Navigation Testbed (ANT), see Fig. 1.8 [10][11]. The main focus of the project was to design a vehicle that had a high degree of intrinsic mobility, thereby decreasing the perception and computation requirements. The hydraulic vehicles have articulated bodies with simple one degree of freedom legs (450 degrees of rotation). The recent testbed is designed to be modular with a minimal configuration of 2x2, but can be increased to 3x2, 4x2, etc. and is capable of such maneuvers as stepping, bridging or crawling. To date, ANT is controlled via supervised teleoperation with some degree of autonomous manipulation.

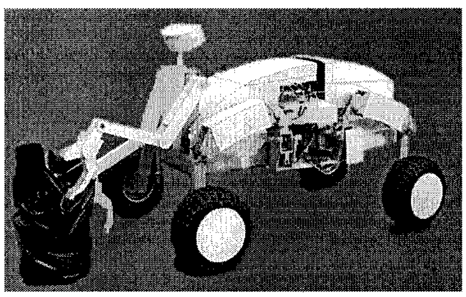

Fig. 1.9. WorkPartner Platform (1998).

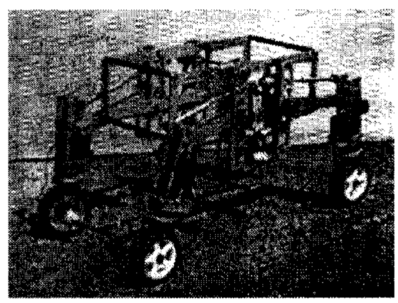

Fig. 1.10. Mini-rover prototype (2000).

One of the more advanced hybrid vehicles to date is WorkPartner, developed by Helsinki University of Technology. The HYBTOR (Hybrid Tractor) platform (Fig. 1.9) is designed to be a moveable workstation in the forest [12]. The active joint frame with four legs is able to move in walking, hybrid or wheel (12 km/h) mode depending on surface conditions. Its control fuses sensing of both the vehicle's states (via potentiometers) and perceptions of the environment. The latter is accomplished mainly using sensors that measure the force applied to the wheel to deduce the shape of the ground simply by running the wheel over it. A mini-rover platform currently being developed by Benamar and Budanov (Fig. 1.10) also employs three-axes force sensing of the wheel to adaptively configure itself to the terrain [13]. Aside from the steerable wheels, each leg on the rover has two additional degrees of freedom (electrically actuated ball screws) used to adjust the kinematic leg.

The Autonomous Systems Lab (ASL) at the Swiss Federal Institute of Technology Lausanne has developed a platform to negotiate terrain with a passive adaptation mechanism [14]. The ASL's Shrimp prototype, see Fig. 1.11, is a 6-wheeled rover whose only actuation is its motorized wheels. It adapts passively with its unique parallel architecture of the wheel forks, which always maintains the instantaneous center of rotation below the wheel axis. This rover is able to overcome steps of twice its wheel diameter with decent off road abilities. The rover can overcome uneven terrain with a frontal inclinations of up to 40 degrees.

Over the years a few researchers have utilized leg-wheel locomotion solely for the purpose of stair climbing. The best example of such a platform is Matsumoto's planar biped with active wheels (Fig. 1.12) [15], which was able to climb up and down shallow stairs following reference trajectories that kept the robot in quasi static equilibrium.

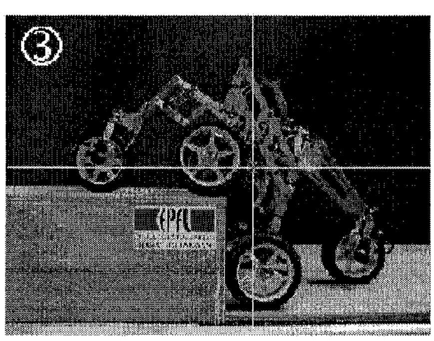

Fig. 1.11. ASL's Shrimp (2000).

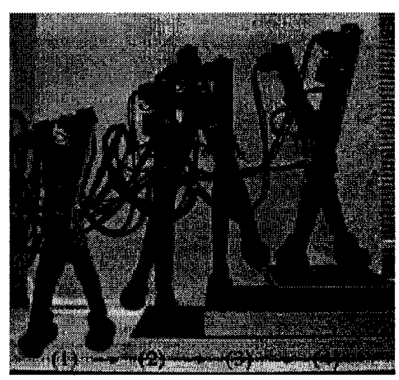

Fig. 1.12. Matsumoto's robot (1995).

1.2.2. Dynamically Stable Quadruped Platforms

Raibert pioneered the field of dynamically stable legged robots with the introduction of a series of hopping robots [16]. In 1982, MIT's Leg Laboratory, founded by Raibert, developed a planar one-legged hopping robot that travelled at speeds up to 1.2 m/s, tolerated moderate disturbances and jumped over small obstacles. The platform, see Fig. 1.13, was able to perform such seemingly complex dynamic feats through the use of rather simple controllers compared to those typically adopted at the time. The control was simplified mainly by separating the task of forward propulsion from that of the vertical hopping. The hopping height was maintained and adjusted by the pneumatic piston that serves as the leg, while the horizontal speed was adjusted using two pneumatic actuators that pivot the leg about the hip. By simply varying the touchdown position of the toe with respect to the center of mass of the robot, the speed and trajectory of the robot were adjusted.

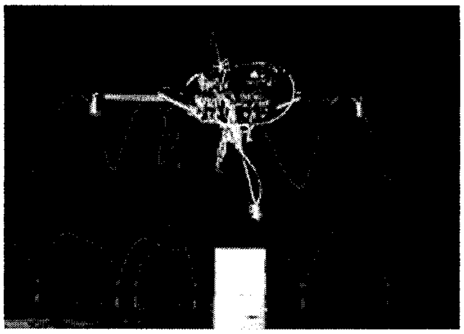

Fig. 1.13. Raibert's biped robot (1982).

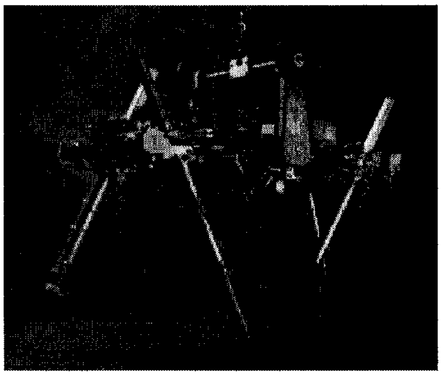

Fig. 1.14. Raibert's quadruped robot (1985).

Raibert applied the same control laws to implement a 3-D hopper in 1983 and subsequently developed multiple legged robots using the same principles. He developed bipeds by treating each of the legs as a single hopping leg, cyclically designating an *active* leg and an *idle* leg. Then, by pairing the legs of a quadruped, Raibert managed to reduce its control to an equivalent *virtual* biped – thereby controlling a four legged platform with the same approach as the one legged hoppers [17]. Pictured in Fig 1.14 is the Leg Lab's dynamic quadruped that was developed between 1984 and 1987 [18]. The platform is hydraulically actuated with three DOF legs: one at the hip in the pitching plane; a second at the hip in the yaw plane; and the third in the prismatic leg, which is actuated by a hydraulic cylinder in series with a passive pneumatic spring. By coupling the legs, the quadruped successfully executed trotting (diagonally paired legs), pacing (lateral pairs), bounding (front pair and rear pair) and several transitions between gaits.

In 1994, Kimura et al. introduced a planar quadruped called Patrush that used a biologically inspired approach for its control [19][20]. Shown in Fig. 1.15, each leg of Patrush I had three joints about the pitch axis; the two upper joints were actuated with DC motors and the lower joint was passively compliant. The 4.6 Kg robot had a body length of 360 mm, a height of 330 mm and a width of 240 mm. It successfully executed trot and pace gaits, and by 1996, the platform was able to negotiate irregular terrain consisting of slopes (up to 12°) and small steps (up to 30 mm). Patrush I was fitted with special running legs in 1997, see Fig. 1.16, that enabled the robot to hop and bound along a flat surface. These legs had the same basic configuration as the original legs, but had a much larger ankle. Presently, a second variation of the platform, Patrush II (Fig. 1.17), is being used by Kimura's lab as a means to compare and study the differences between simulation and experiment.

To test the biological control approach in three dimensions, Kimura's laboratory built a new quadruped, Tekken, in 2000 [19]. Pictured in Fig. 1.18, the platform has four DOF legs: two DOF at the hip (pitch and yaw), one DOF at the knee (pitch) and a passively compliant ankle (pitch). The 3.1 Kg robot had a body length of 400 mm, a height of 210 mm and a width of 120 mm. Tekken has performed dynamic walking gaits over flat surfaces (up to 1m/s) and over irregular terrain that consisted of slopes (up to 10°) and small steps (up to 40 mm). It has also executed running or bounding gaits over flat terrain, but the majority of the current research on this platform is directed towards improving Tekken's mobility on irregular surfaces.

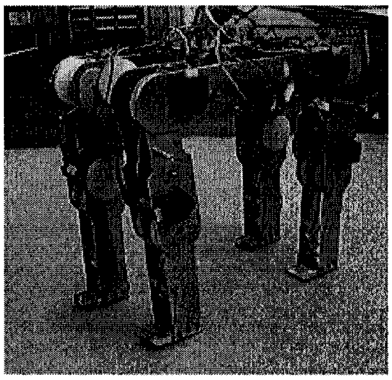

Fig. 1.15. Patrush I (1994).

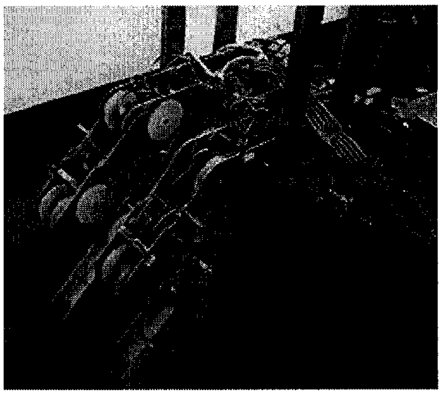

Fig. 1.16. Patrush I with running legs (1997).

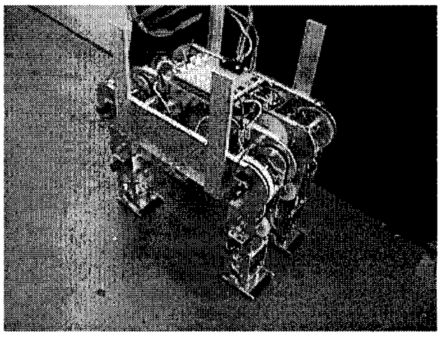

Fig. 1.17. Patrush II (2000).

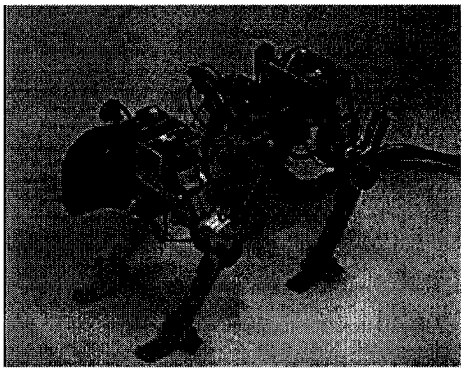

Fig. 1.18. Tekken (2000).

All of the aforementioned quadrupeds were powered via a tethered cable, and in the case of Kimura's platforms, the computation was also done *off-board.* To date, the only dynamic quadrupeds that are fully power autonomous and have *on-board* computation are the Scout robots developed at the Ambulatory Robotics Lab at McGill University. These robots are discussed in the next section.

1.2.3. Previous Robots in the ARL

The Ambulatory Robotics Lab (ARL) was founded by Professor Martin Buehler in 1991 with the directive to create dynamically stable robots in the tradition of Raibert [21]. His main objective was to exploit the passive dynamics of robots and use elastic mechanical devices to reduce the number of DOF and the power consumption. The first such robot was a planar monopod that had only two DOF: an electrically actuated hip and radially compliant leg [22][23]. The passive compliance in the leg enabled the platform to recover the majority of the energy lost at touchdown, thereby decoupling a great deal of the required actuator energy from the gravitational loads. Using control algorithms based on Raibert's approaches, the Monopod was able to run at a speed of 1.2 m/s with an average power consumption of 150 W. To realize lower power consumption, the Monopod II platform was built in 1996 and is shown in Fig. 1.18. It inherited most of the features of Monopod I with an additional compliant mechanism at the hip. This passive mechanism was responsible for sweeping the leg forward during flight and resulted in reducing the power consumption by a factor of two; achieving stable dynamic running at a speed of 1.2 m/s with an average mechanical power consumption of 68W – a world record for power autonomous legged locomotion.

To further demonstrate the ability to implement dynamic behaviour on mechanically simple platforms, the Scout I robot was designed and built in 1997 [24][25]. Shown in Fig. 1.19, this small quadruped had stiff legs with only one DOF at the hip joints (pitch axis). As in the monopods, the natural or passive dynamics of the robot were exploited to achieve stable motion. The platform walked by rocking back and forth, alternating the *lift-off* phases of the front and rear pairs of legs. The front legs were kept at a constant position, while the rear legs swept backwards at touchdown to move the robot forward. This gait was realized by sensing only joint positions and touchdown. The robot also achieved a variety of other behaviours, including sidestepping, turning and climbing steps up to 45% of its leg length.

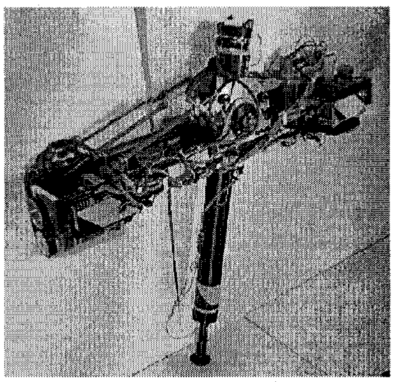

Fig. 1.18. ARL's Monopod II (1996).

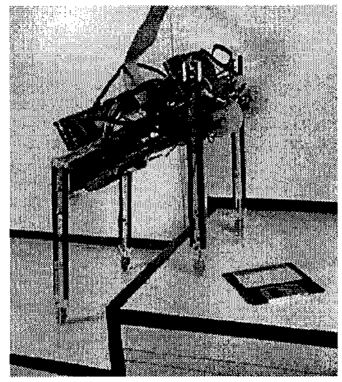

Fig. 1.19. ARL's Scout I (1997).

Fig. 1.20. ARL's Scout II (1998).

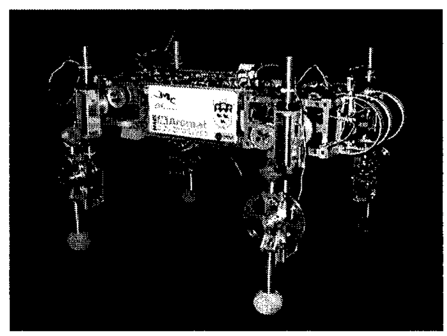

Fig. 1.21. ARL's Scout II with passive knees (1999).

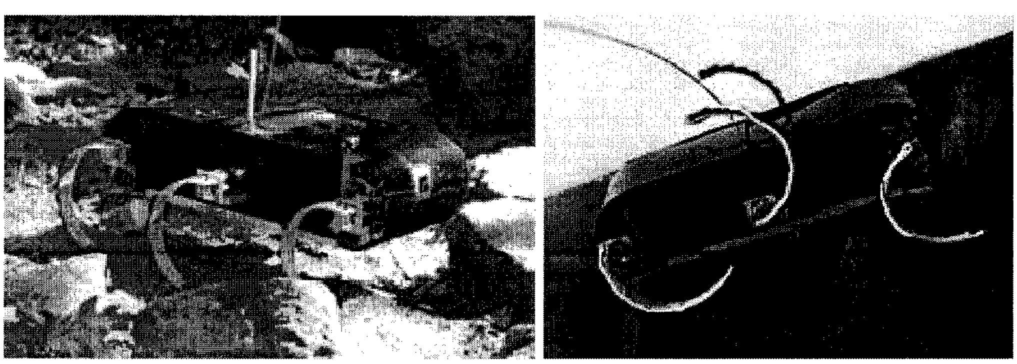

Fig. 1.22. ARL's RHex platform standing (left) and stair climbing (right).

In 1998, a larger quadruped, Scout II, was designed and built to realize dynamic running [26][27]. Shown in Fig. 1.20, the robot built upon Scout I's simplicity using the same basic configuration with the addition of compliant legs. In the same manner as the Monopods, the sprung prismatic legs enable the robot to recover the majority of the vertical energy lost during touchdown. This allowed for the actuators, power supply and computing equipment all to be mounted onboard the platform. Scout II achieved dynamic walking, bounding (1.3 m/s) and pronking gaits, as well as turning and step climbing [27][28][29]. In 1999, the Scout II platform executed planar trotting with modified legs that incorporated passive knees (see Fig. 1.21) [30].

By introducing compliant legs and exercising simplicity in both the mechanics and the control, Buehler et al. had developed the first power autonomous quadruped that performed stable dynamic motion. The Scout series set new standards for dynamic machines by reducing required complexity and cost, as well as increasing their reliability. It was a fundamental step towards the target of realizing dynamic behaviour on legged platforms in *real world* operation.

Inspired by the biomechanics of cockroaches, a Robotic Hexapod (RHex) platform was designed and constructed in 1999 [31][32]. Each of the six legs only has one actuated DOF at the hips and is radially compliant. The platform's primary means of locomotion is the tripod gait. This gait relies on the inherent stability of a tripod stance; front and rear leg touchdown on one side with middle leg touchdown on the other side. All three legs in each tripod set are synchronized and 180 degrees out of phase with the opposite set. Using this gait, the RHex platform is able to transverse rugged and highly fractured outdoor terrain with a performance level unmatched by any other legged platform to date. Again, the simplicity of its mechanics and control facilitate a highly robust and reliable platform that can be used in *real world* operation. The robot also has two dynamic gaits; the pronk and a dynamic tripod gait with aerial phases between the alternating tripod stances. In 2002, a simple stair climbing algorithm was implemented with such success that it made RHex the most reliable legged stair climber to date [34]. Owing to its superior terrain negotiating capabilities, the RHex platform exemplifies the mobility advantages of legs over traditional wheels or tracks.

Chapter 2

Dynamic Behaviours

2.1. Modeling

A simulation environment was used to explore the feasibility of a variety of dynamic behaviours. It was used to deduce an optimal mechanical configuration, to converge upon design parameters and to develop controllers. The first step was to create an accurate model whose parameters could be changed easily to allow for the assessment of a wide range of possibilities. *Working Model* software packages were used with their Script Editors to develop parametric models with variables that could be changed at runtime [35][36]. Without the use of the scripts, only the initial conditions could have been changed and *real-time* controllers could not have been developed.

The basic configuration of the platform was adopted from the Scout II robot at the ARL, with the addition of an active wheel placed at the foot of each leg. Thus, each leg had three degrees of freedom: an actuated joint at the hip (pitch axis), a passively compliant telescoping leg and an actuated wheel joint (pitch axis). Values for the robot's geometry, mass and actuation parameters were estimated initially by scaling between two existing platforms, as outlined in the section below.

2.1.1. Scaling Methodology

A simple scaling methodology was employed to obtain realistic estimates of design parameters and to allow for performance assessment of a wide range of platform sizes. Two existing platforms were used as baselines from which the simulated sizes were interpolated. The two platforms used were the DRES ANT (Fig. 1.8) and the ARL RHex (Fig. 1.22), both discussed in Chapter 1. The reasoning behind using these 6 legged machines, versus two 4 legged machines, lies in the fact that the work presented in this thesis was done in partial fulfillment of a contract with DRES, which was targeted to extend the mobility of the ANT platform [37][42]. (This is also why the platform developed here is called ANT.) One of the main ideals behind this family of platforms is a modular design that permits a flexible operation architecture. Each module has one pair of legs, with a minimal configuration of 2 modules (2x2, 4 legs) and can be increased to 3x2, 4x2, etc. to meet the requirements of different operating tasks and/or payloads. As such, when the simulation model was initially developed, 6 legged (3x2) models were being used to investigate statically stable behaviour. When the dynamic behaviour of the 4 legged (2x2) configuration was investigated, the middle module was simply removed from the platform, as shown in Fig. 2.1.

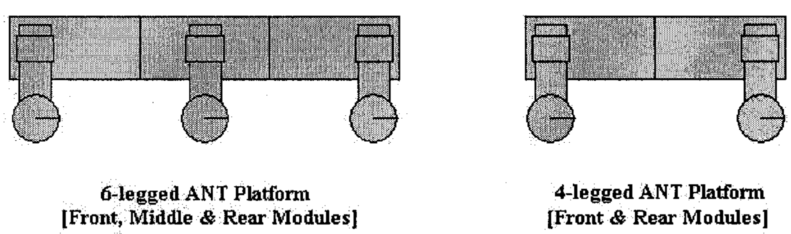

Fig. 2.1. Examples of 6 and 4 legged ANT models.

The purpose of the scaling procedure is to obtain realistic parameters as functions of the body length. That is, given only the body length as input, the scaling technique yields all the estimated design parameters. This allowed for a rapid, practical estimation of design variables and was especially useful in estimating the actuation parameters, which are normally very intricate functions of many interdependent variables. Table 2.1 outlines the methods chosen to scale each parameter. The order in the table reflects the computational order of the parameters (i.e. volume appears before mass because the calculation of mass requires the body volume). Table 2.2 contains the values used for interpolation.

Table 2.1. Scaling methodology.

Parameter	**Method of Computation**
Body length	INPUT: 0.4 to 3.38 m (RHex to ANT)
Body thickness	Linearly interpolated as a function of body length
Body width	Linearly interpolated as a function of body length
Body volume	Body length x body thickness x body width
Body mass density	Linearly interpolated as a function of body length
Body mass	Body volume × body mass density
Power density (Hip torque/body mass)	Linearly interpolated as a function of body length
Hip torque	Body mass × power density
Hip no load speed	Linearly interpolated as a function of hip torque
Wheel torque	Linearly interpolated as a function of hip torque
Wheel no load speed	Linearly interpolated as a function of hip torque

Table 2.2. Scaling methodology.

Parameter (units)	**RHEX**	**ANT**
Body length (m)	0.40	3.38
Body thickness (m)	0.12	0.5
Body width (m)	0.09	1.25
Body volume (m^3)	0.004	2.113
Body mass density (Kg/m^3)	1736	645
Body mass (Kg)	7.5	1363
Power density (Nm/Kg) (hip torque/body mass)	0.73	1.37
Hip torque (Nm)	5.5	1865
Hip no load speed (rpm)	303	58
Wheel torque (Nm)	5.5	280
Wheel no load speed (rpm)	303	260

The RHex platform was enhanced with active wheels by assuming the wheel actuation to be roughly equal to the hip actuation. This served only as a starting point, as the selection of the wheel actuation was later based upon behavioural studies of the platform in simulation and is discussed in *Chapter 3*.

The effectiveness of this scaling methodology lies in the exploitation of the power density. The complex relationships between the geometry, mass and actuation have already been successfully established on the two existing platforms and are embodied by their power densities. Once the relationship between body length and mass is established, the power density is a simple means to accurately relate the mass to the hip torque. The other actuation parameters were then linearly interpolated from the existing platform values as functions of the hip torque.

2.1.2. Model Parameters

The platform was designed to be as symmetrical as possible, so as to simplify the control and ensure identical behaviour in the event that the robot was flipped over. Symmetry proved to be especially important for dynamic behaviour, as many of these maneuvers purposely flip the robot and often rely on symmetrical mass distribution. Thus, the body mass was evenly distributed and the hip joints were placed symmetrically on the body. The body was left unarticulated, as the actuation of a body joint capable of providing dynamic motion would be quite massive; any foreseeable gains from this articulation would be outweighed by the mass increase and result in a decrease in the dynamic performance. The addition of body articulation was also avoided so as to maintain the platform's concept of simplicity.

The leg length was dictated by the necessity of the platform to easily pitch itself upwards. Looking at Fig. 2.2, it can be seen that using a leg length that extends the wheel beyond the robot's center of mass enables such pitching, even when the robot's torso is horizontal. The ability to control the body pitch with such ease proved to be crucial for performing many dynamic maneuvers. Increasing the leg length beyond this increases the moment arm of the leg, which decreases the effectiveness of the leg torque and yields observable decreases in performance. Therefore, the ideal leg length was taken to be the length required to just reach the body's center of mass. Given this criteria for leg length, it can be seen how hip separation plays a role in the leg length. Looking at Fig. 2.3, larger hip separation requires longer legs to reach the center of mass, which again decreases the effectiveness of the leg torque. Thus, the hip separation was made as small as possible without hindering the feasibility of any behaviour. The actual hip separation was converged upon through trials in simulation.

The wheels' diameter was made relatively small in comparison to existing hybrid platforms. This was to allow for precise foot placement and to lighten the legs, both of which are necessary for dynamic behaviour. Reducing the size of the wheels decreases the mobility of the platform in *wheel-only* mode, but the need for larger wheels is negated substantially by the mobility arsenals gained with dynamic behaviour.

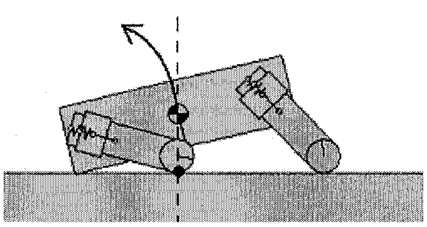

Fig. 2.2. Legs induce flipping moment.

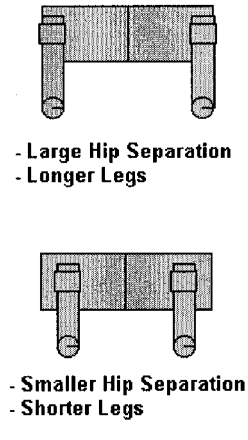

Fig. 2.3. Hip separation effects leg length.

The first requirement for developing controllers on a robotics platform is the ability to properly pass position and speed commands to the joints. The simple and effective way this was accomplished was through the use of PD joint control, which regulates the torque applied to the actuators:

$$\tau_{Motor} = K_D(\theta_{Desired} - \theta_{Actual}) + K_V(\dot{\theta}_{Desired} - \dot{\theta}_{Actual}) \tag{2.1}$$

K_D and K_V are constants or gains *tuned* for the particular joint to obtain desired tracking characteristics. The actuation of the platform must be properly modelled so that the simulations are accurate enough to use in assessment and design. In this case, a generalized torque-speed curve was used to yield the operating characteristics of DC motors. This curve is plotted in Fig. 2.4, where the shaded region is the permissible operating range. This standard actuation model requires only two parameters of a DC motor: stall torque and no load speed. These parameters of the torque-speed curve were initially set to those obtained through the scaling procedure, however, these values were adjusted slightly in simulation to optimize performance.

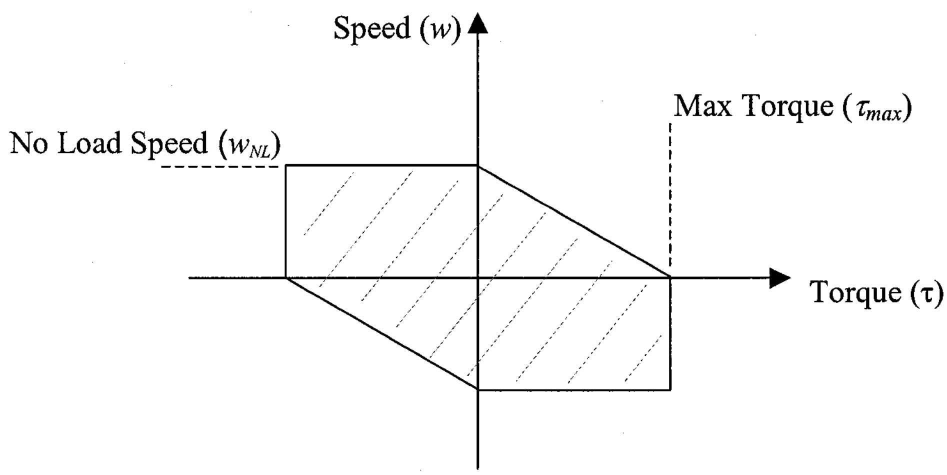

Fig. 2.4. Generalized Torque-Speed Curve.

2.1.3. Leg Compliance

The leg compliance is the only modelling parameter that has not been discussed thus far. It is an important aspect of the model as it is responsible for enabling the majority of the dynamic behaviour. This is because dynamic behaviour is characterized by *quick* motion and often contains flight phases, usually requiring the expenditure of large amounts of energy. As the maneuver becomes more dynamic, the energy losses at touchdown increase significantly, making it increasingly more difficult to implement such behaviour on an autonomously powered platform. The ability to recover some of these energy losses is crucial to the implementation of a dynamic platform [21].

To expand on how leg compliance was used on the platform, the bounding gait in Fig. 2.5 is presented. It can be seen that during the front leg's stance phase (B to E), the leg's compliance first stores the energy (B, C) and then returns it to the body (D, E). In this fashion, the majority of the vertical energy, as well as a portion of the forward momentum lost during touchdown, is recovered over the duration of the stance phase. With the majority of the vertical energy restored by the sprung legs, most of the actuators energy can be used to propel the robot forward. This yields higher feasible speeds and more efficiency with this otherwise impossible gait.

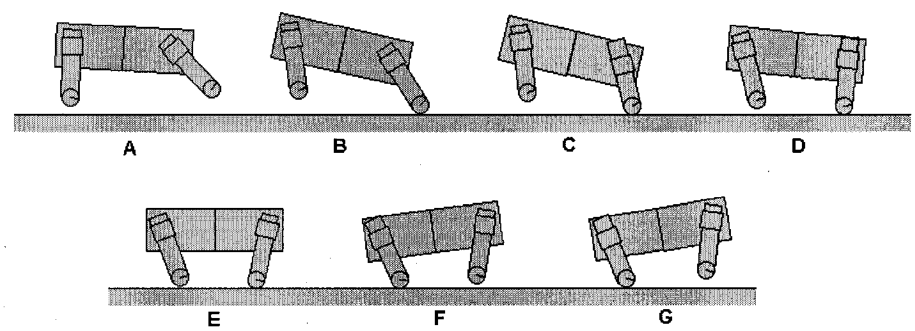

Fig. 2.5. Storing and releasing energy with leg compliance in a bounding gait.

The forward momentum stored in the compliance during touchdown can be used either to increase the vertical energy or to restore the forward momentum. The latter is accomplished by directing the spring return slightly forward during takeoff, in the same manner as the front leg in Fig.2.5. D and E.

The compliance cannot return all of the energy lost at touchdown owing to two main factors. The first is the frictional losses in the leg compliance; made up of standard Coulomb forces, viscous damping or any other source of frictional loss. It was assumed that including viscous damping in the model was sufficient to account for these losses and is standard practice in the ARL. Thus, the frictional resistance in the leg compliance was modelled as,

$$F_{friction} = c\dot{l} \tag{2.2}$$

where c (Ns/m) is the damping coefficient and $\dot{l}$ (m/s) is the radial velocity of the prismatic leg. The value c was taken to be 25 Ns/m, which was the experimentally measured value of the Scout II prismatic leg. The second source of energy loss is the unsprung mass on the robot. This is the mass of the robot that does not transfer its momentum to the spring in the compliance, which in this case is the mass of the legs and wheels. When the robot touches down, the momentum of the legs and wheels is dissipated to the ground, not to the spring (Fig.2.5. B,C). Since the momentum of the unsprung mass is irretrievable, it is important that the unsprung mass be kept as low as possible on a dynamic platform.

A good starting point for choosing a spring constant for a small to mid-sized robotic platform is the following general guideline pertaining to the natural frequency (f_n) of the platform.

$$f_n = \frac{\sqrt{k/m}}{2\pi} \approx 2\,\text{Hz} \tag{2.3}$$

Where k (Nm) is the spring constant and m (Kg) is the mass of the platform. This rule of thumb used in the ARL stems from many years of experience working with compliant legs, but correlates quite well with Farley's et al. findings on animal legs [38]. Farley measured the ground reaction forces of trotting quadrupeds and hopping bipeds while filming their motion. Each leg-pair was then modeled as a single linear spring directly connecting a point mass at the mass center to the midpoint between the feet. Schmiedeler and Waldron built upon Farley's findings to develop the following expression that approximates the effective individual leg stiffness for quadruped animals [39].

$$k = 500m^{0.67} \tag{2.4}$$

This expression for animal legs correlates very well with the 2 Hz rule of thumb adopted by the ARL. This is most likely owing to the fact that dynamic robots are designed to mimic animals and their behaviour. Thus, it makes sense to use models for animals to gain intelligent estimates of the required leg stiffness. As these expressions are solely functions of body mass, they were easily integrated into the scaling method to produce initial estimates for the spring stiffness. As with most of the other parameters, the spring constant was then adjusted in simulation to optimize performance.

There are a number of issues that were taken into consideration when adjusting and selecting the spring constant. For example, the spring's stiffness directly effects the obtainable speeds, proving that a softer leg compliance lends itself to slower maneuvers. This is because the duration of the stance phase is a function of the spring's stiffness (i.e. the softer the spring, the longer the stance phase and visa versa). A platform with stiffer springs has a shorter stance time, allowing for a faster sweep rate through the same sweep angle, which in turn yields quicker behaviour. This imposes an upper limit on spring stiffness, as the no load speed of the motor dictates the maximum sweep rate and therefore the spring's stiffness. One must also consider that occasionally the actuators drive energy into the spring by forcing the shortening of the leg during the stance phase. If a stiffer spring is used, the stance time and the opportunity to drive energy into the spring is reduced, again imposing an upper limitation on spring stiffness.

Leg travel also plays a significant role in the selection of a spring constant. Softer springs require more travel, forcing limitations such as ground clearance to dictate a lower boundary of stiffness. Preload can be used to reduce both the leg travel and the stance time, as increasing the preload acts in the same manner as increasing the spring stiffness. Interestingly, increasing either the spring's stiffness or the preload both result in greater lift-off velocities with higher return heights. This phenomenon can be understood by looking at the definition of the differential work done by the viscous friction.

$$\partial W_{friction} = \sum_i F_{f_i} dl = \sum_i (c\dot{l}_i) dl = \sum_i (c\dot{l}_i^2) dt. \tag{2.5}$$

It can be seen that integrating over less time (i.e. shorter stance phase) yields less losses in friction. With less loss of energy, a stiffer spring with larger preload yields greater return heights with less travel.

Thus, raising the spring stiffness as high as the actuation permits is a good design practice, as travel and friction are reduced while speed of movement is increased. However, this ceiling is hard to quantify as the required sweep angles and corresponding speeds are functions of the properties and behaviours specific to the platform. Thus, as mentioned, equations (2.3) or (2.4) were used as an initial guidelines for leg stiffness, but the leg stiffness was increased to the highest feasible value through observation and trials in simulation.

2.1.4. Equations of Motion

With the development of any new platform, it is good practice to develop and study its equations of motion. The development of such a model leads to better understanding of the platform and can be utilized to implement various controllers. To this end, the dynamic model presented in Appendix A was developed using the Lagrangian Methodology and the Software package *Mathematica* [41]. These equations better acquainted the author with the platform and are included in the appendices for reference. They will also assist future projects undertaking the platform's advancement.

2.2. Benefits of a Wheel at the Foot of the Leg

There are obvious efficiency gains associated with employing wheeled locomotion over flat terrain. However, placing a wheel at the foot of the leg, rather than say on the body, enables many behavioural advantages other than simply rolling or ground following. An active wheel enables many additional behaviours through wheel resistance (braking) or the ability to hold/change leg angles while driving the *foot* along the ground. In many instances, the latter produces otherwise impossible accelerations that spin the body around generating high energy maneuvers. The behavioural gains that this additional degree of freedom yields are described in the next section, *Simulation of Dynamic Behaviour*. This section addresses the more straightforward, quantifiable type of advantages associated with the placement of a wheel at the foot of the leg; advantages that enable higher dynamic performance than previous power autonomous platforms.

The first can be demonstrated exemplifying the behaviour depicted in Fig. 2.6. Throughout steps A to E, the platform is applying the maximum power to its hip actuators in an attempt to stand up as quickly as possible. Consider the following three possibilities for the wheel actuation: locked or braked (i.e. no wheels), passive (no actuation) and active (with actuation). In Fig. 2.7, the platform with the wheels locked does not gain flight from this maneuver owing to the friction losses between the locked wheels and the ground. However, the one with passive wheels does gain flight, while the platform with active wheels gains even more flight. Thus, the wheels, even if passive, increase the effectiveness of the hip torque.

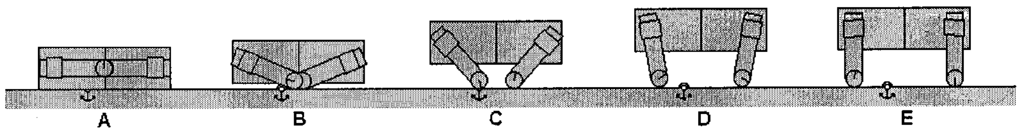

Fig. 2.6. ANT Standing up using all legs.

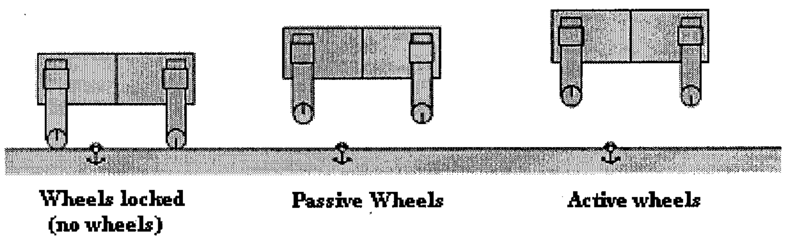

Fig. 2.7. Flight gained from standing up with different wheel actuation.

It is obvious that a platform with the active wheels would gain more flight than one with passive wheels. However, one may pose that instead of adding power to actuate the wheel, why not simply increase the power of the hip actuators while using passive wheels with brakes? The reasoning is that the placement of an active wheel at the foot of the leg significantly increases the efficiency of the *effective power* applied to the hips. To qualify this principle, imagine the situation depicted in Fig.2.8. With passive wheels, as shown in case A, the hips have *just* enough power to hold the body in the position shown. In order to raise the body upwards, the hips would have to exert additional power. In case B, the active wheels provide the extra power required to move the body upwards. Thus, the wheel power can be considered to translate to an *effective power* increase at the hips, or to generate an *effective hip torque*. It will be shown that adding power to the platform through the active wheels is much more efficient than allocating additional power to the hips.

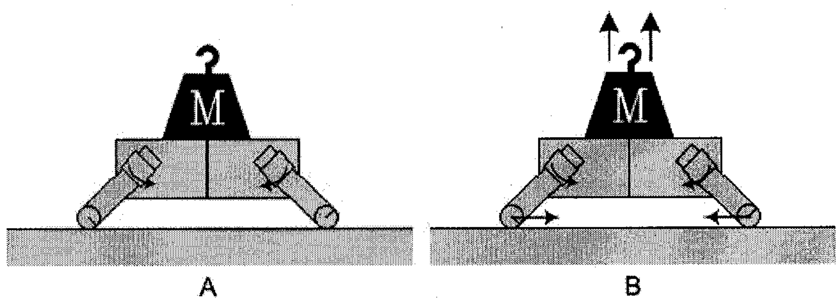

Fig. 2.8. A - Lift at equilibrium with passive wheels, B – Lifting with active wheels.

To quantify the wheel's effective hip power, the wheel's effective hip torque is needed. The geometry and nomenclature used are contained below in Fig. 2.9.

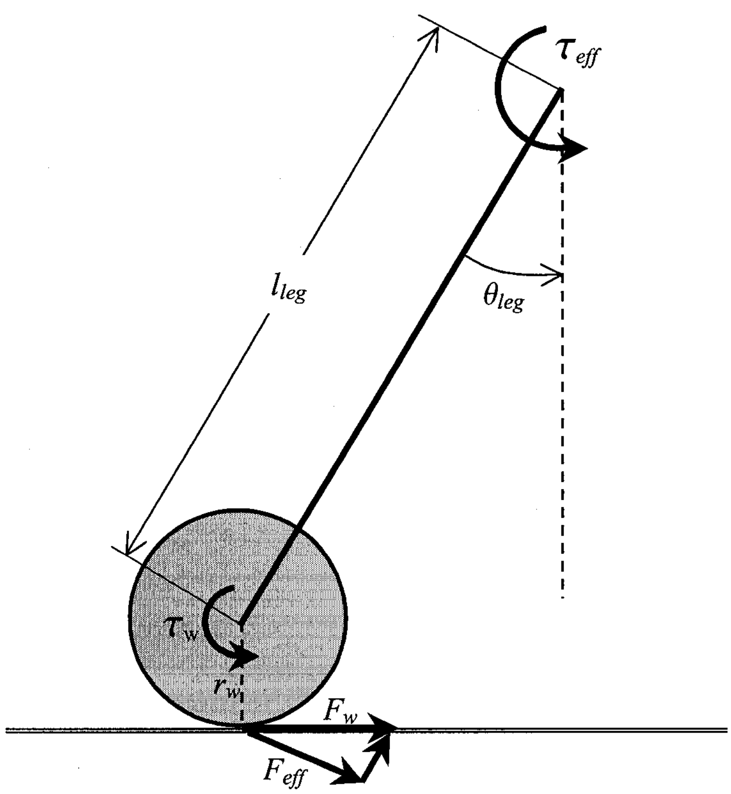

Fig. 2.9. Nomenclature used for effective torque calculations.

where,

τ_{eff} = effective hip torque from wheel

τ_w = wheel torque

l_{leg} = length of leg

θ_{leg} = leg angle

F_w = tangential wheel force

F_{eff} = effective hip tangential force

r_w = wheel radius

The following equations outline the calculations used to deduce the effective hip torque (τ_{eff})generated by the wheel. Assuming no slipping occurs,

$$F_w = \frac{\tau_w}{r_w} \tag{2.6}$$

$$F_{eff} = F_w Cos\theta_{leg} = \frac{\tau_w}{r_w} Cos\theta_{leg} \tag{2.7}$$

$$\tau_{eff} = F_{eff} l_{leg} = \left(\frac{l_{leg}}{r_w} Cos\theta_{leg} \right) \tau_w = C_\tau \tau_w \tag{2.8}$$

Thus, the wheel's effective hip torque is dependent upon the leg angle and length. Owing to the compliance in ANT's legs, both variables must be considered. The factor C_τ is the ratio of the effective hip torque generated by the wheel to the torque applied at the wheel. Fig. 2.10 is a plot of the change in the factor C_τ through a 0 to 60 degree sweep, with an 80 mm change on a 200 mm leg and a 60 mm wheel. These values are the actual functional range of the ANT testbed, presented in *Chapter 3*. From Fig. 2.10, it can be seen that for regular dynamic maneuvers the torque factor C_τ lies roughly between 2 and 6.5. This means that, for 1 Nm of torque applied at the wheel, that between 2 and 6.5 Nm of torque would have to be generated by the hips to yield the same body accelerations.

This mechanical advantage of the wheel leads to tremendous gains in electrical power. To quantify this, the relationship between the output torque and the input power of the electrical motors is required. Since the motors on the ANT testbed are connected to gearheads, the torque generated by the motor is,

$$\tau_m = \frac{\tau_{output}}{N_m \varepsilon_m}, \tag{2.9}$$

which can be used with the current drawn by the motor,

$$i_m = \frac{\tau_m}{k_\tau}, \tag{2.10}$$

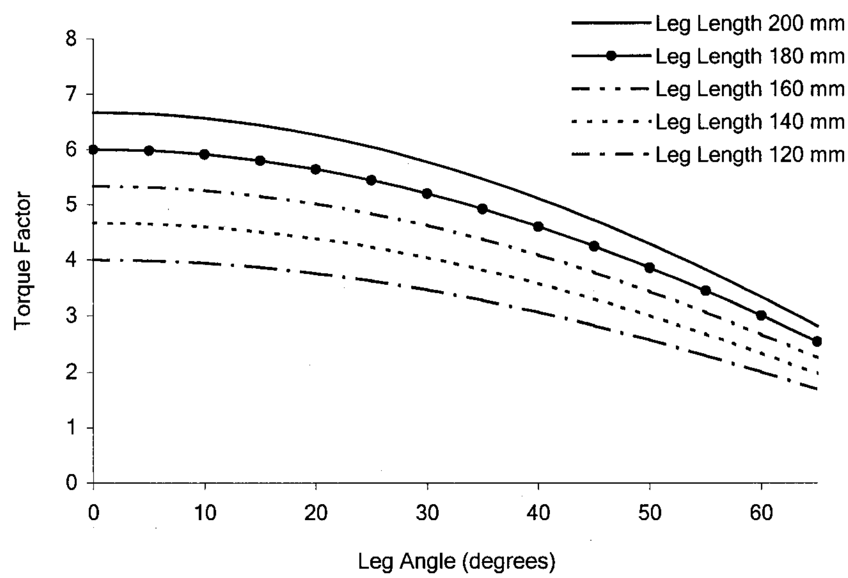

Fig. 2.10. Torque factor for ANT's range of operation.

to compute the electrical power used by the motor,

$$P_m = r_a i_m^{\ 2} = r_a \left(\frac{\tau_{output}}{N_m \varepsilon_m k_\tau} \right)^2, \tag{2.11}$$

where

P_m = power used by the motor

τ_m = torque generated by the motor

τ_{output} = torque after gearhead

N_m = gear reduction

ε_m = gearhead efficiency

i_m = motor current

k_τ = torque constant (Nm/A)

r_a = armature or terminal resistance.

The electrical power used by the testbed's hip and wheel motors was plotted as a function of the torque applied to the joints in Fig. 2.11. For the situation depicted in Fig. 2.8, the power required by the hip motor to generate the same accelerations as those generated with the use of the wheel would be

$$P_{hip} = r_{a_{hip}} \left(\frac{\tau_{hip_i} + \tau_{eff}}{N_{hip}\varepsilon_{hip}k_{\tau\, hip}} \right)^2 \tag{2.12}$$

where, τ_{hip_i} is the initial torque applied to the hips without the wheels (see Fig. 2.8.A). This power can then be compared to the power used by the wheel,

$$P_{wheel} = r_{a_{wheel}} \left(\frac{\tau_{wheel}}{N_{wheel}\varepsilon_{wheel}k_{\tau\, wheel}} \right)^2 \tag{2.13}$$

using the power factor,

$$C_P = \frac{P_{hip} - P_i}{P_{wheel}}. \tag{2.14}$$

where, P_i is the initial power used by the hip actuators to apply the initial hip torque τ_{hip_i}. This initial torque τ_{hip_i} must be considered because the hip must exert a minimum torque, which is required to position the legs and to hold up the body.

Consider the case where the hip actuation is outputting 90% of its maximum torque (stall) and it is desired to raise this to 100% of the stall torque. It turns out that the power required by the hip actuation is much more than power required by the wheel actuation to accomplish the same effective gain in hip torque. The power factor C_p for this case is plotted over the ANT testbed's range of operation in Fig. 2.12. It can be seen from the plot that the wheel actuation is up to 55 times more efficient than the hip actuation to perform this task. This is owing to the fact that for this case, the hip's motor is near stall or the high power dissipation range of the motor (see Fig. 2.11). Due to the mechanical advantage of the wheel placement, the wheel only needs to operate in the lower torque, or lower power dissipation range, to makeup the additional torque.

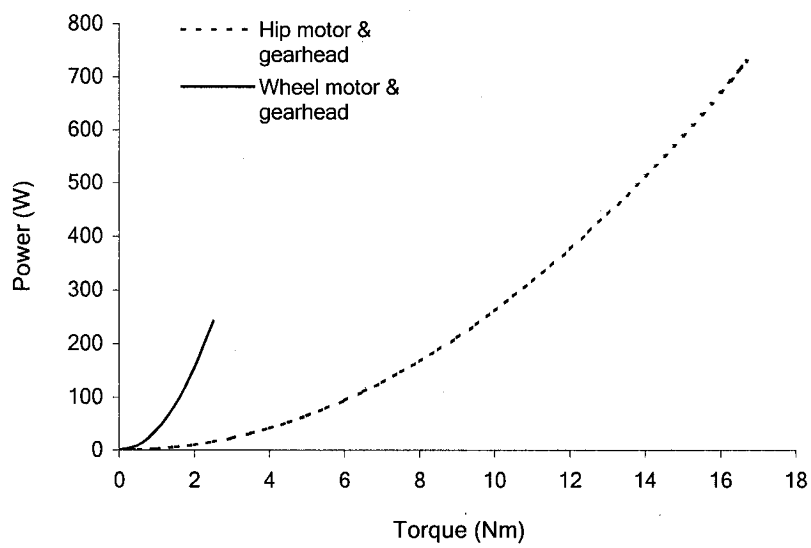

Fig. 2.11. Electrical power of ANT's motors as a function of the torque applied to the joints.

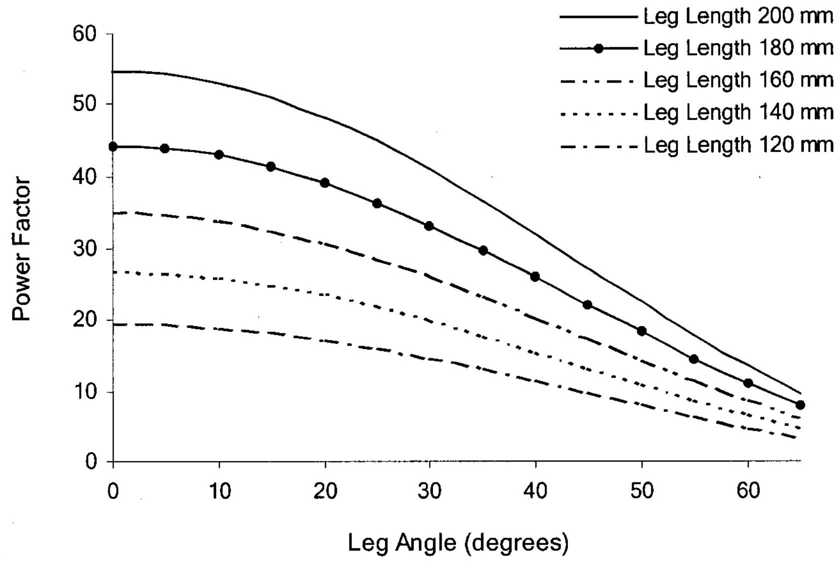

Fig. 2.12. Power factor for raising the hip torque from 90% stall to 100% stall.

To properly assess the efficiency of the wheel actuation, consider the case where the hip actuators are operating in the low power range (10% of stall), while the wheels are operating in their high power region (100% of stall). Here, the wheel actuators are using their maximum power, while the hip power is calculated using Eq. 2.12. The power factor C_p is plotted for this case in Fig. 2.13, where it can be seen that the wheel actuation is still up to 3.75 times more efficient than the hip actuation. However, this case is not likely as there is a minimum power required by the hips to hold the body in place, which far exceeds the 10% of stall used in this example. It should be noted for this case that at the larger angles and shorter leg lengths, the hip actuation is actually slightly more efficient.

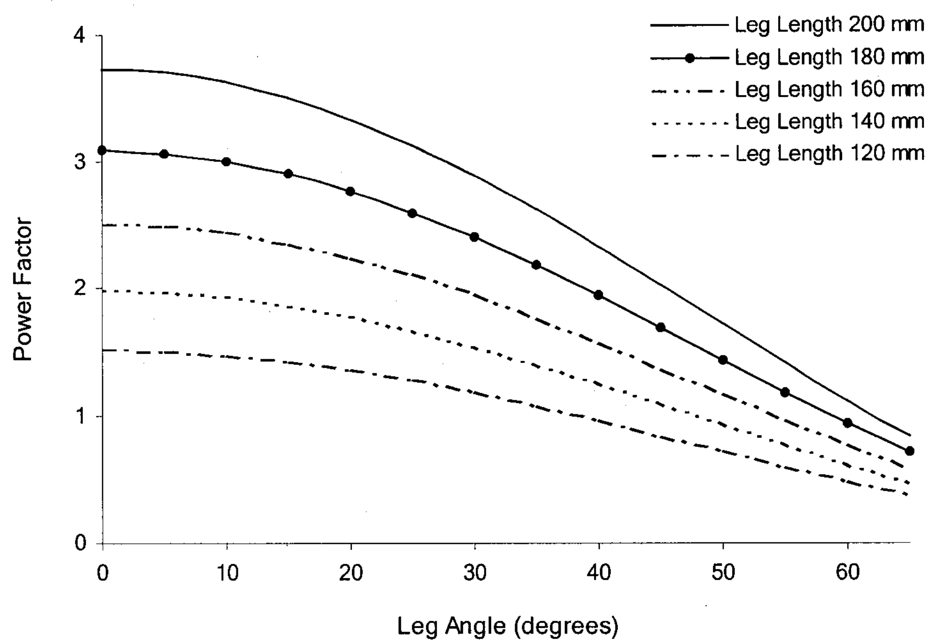

Fig. 2.13. Power factor when hip is operating at 10% stall and wheel is operating at 100% stall.

As a final example, consider the more plausible case where the hip actuators are operating in the mid-torque range (60% of stall), while the wheels are operating in their high power region (100% of stall). Here, the power of the hip actuation needed to match the accelerations gained with the wheel power, far exceed the hip's maximum deliverable power in most instances. The hip actuators, of course, can only deliver up to 100% of their stall torque. In this case, the wheel actuation raised the effective hip torque from 60% to 100% of the feasible stall torque with 1/3 the energy requirements. In other words, it would have taken the hips 3 times the power used by the wheels to bring themselves to maximum torque. The remaining 2/3 of the wheel power produces an effective hip torque exceeding that of the hip actuation's stall torque. This effective increase in the hip's stall torque is plotted as percentages of the hip's true stall torque in Fig. 2.14.

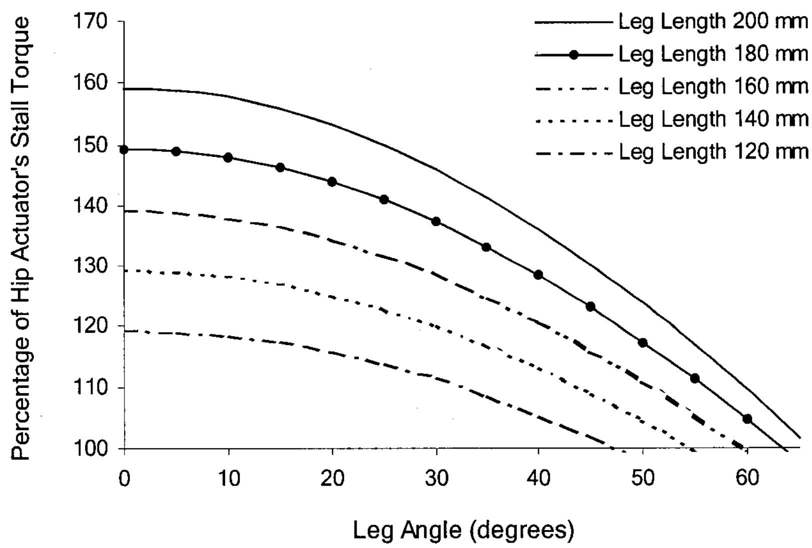

Fig. 2.14. Percentage of effective increase in stall torque.

The underlying result is that power can be more efficiently applied to the hips by indirectly applying it to wheels placed at the foot of the leg. This efficiency gain is one of the key factors that enabled the quadruped introduced here to realize many dynamic feats that were previously unobtainable. Moreover, the reduction in required hip torque allowed for smaller gear ratios at the hip, yielding higher no load speeds that allow the legs to sweep faster. This in turn increases the feasible speeds and the dynamic capability of the platform.

Another benefit of placing a wheel at the foot of the leg is the ability to adjust the toe position during stance phase so as not to hinder the compliance. Looking at Fig. 2.15, it can be seen that during a stance phase with all 4 legs on the ground that the toe separation increases as the leg length (compliance) shortens. This is caused by the fact that the hip separation remains constant while the leg length changes. Without the wheels, the toe would scrape along the ground hindering the storage of energy in the compliance. The energy to scrape the toe along the ground would come from part of the body's momentum, thereby decreasing the momentum available to be stored in the compliance. As well, the forces from the body trying to push the toe cause an increase in frictional forces on the slider, decreasing the effectiveness of the compliance.

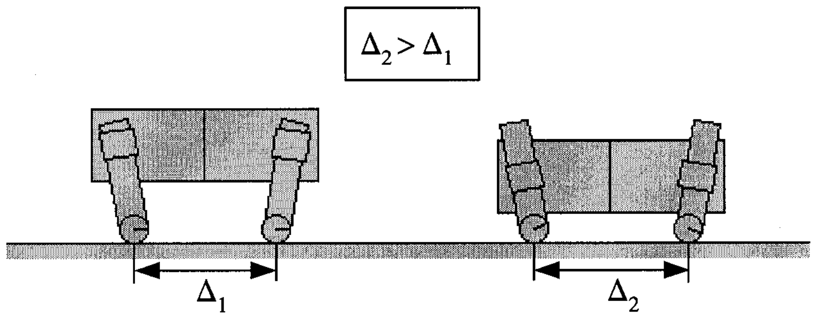

Fig. 2.15. Toe separation increase during stance phase with passive wheels.

2.3. Simulation of Dynamic Behaviour

Dynamic behaviours widen the scope of negotiable obstacles, increase efficiency and generally increase the mobility realm. As such, a smaller robot with dynamic capabilities will outperform a larger robot without these arsenals. This is the main motivation behind developing a dynamic platform, however, the high energetics involved with these behaviours makes them difficult to realize on a power autonomous platform. The placement of wheels at the foot of the legs, introduced here, widens the scope of dynamic maneuvers for a power autonomous platform. This section presents these maneuvers, with possible utilities, and discusses how this extra degree of freedom was exploited to realize them.

The scaling techniques were used to get initial values for the platform's parameters and were then adjusted in simulation to optimize performance. All of the behaviours presented here were simulated with models having a body length of either 0.50 m or 0.67 m. The values of those parameters critical to performing the maneuvers are contained in Table 2.3 for these two models. In the captions of the figures presenting these behaviours below, the body length (l_{body}) is given so that Table 2.3 may be referenced. Note that the actuation parameters were checked with manufacture's catalogues to ensure realistic results and to validate the scaling techniques.

Table 2.3. Simulation parameters for two models.

Body Length (m)	0.5	0.67
Mass (Kg)	19	64
Spring Constant (N/m)	5000	10000
Max Hip Torque (Nm)	16	83
Max Hip Speed (rpm)	330	290
Max Wheel Torque (Nm)	3.5	17
Max Wheel Speed (rpm)	500	300

2.3.1. Maneuvers with Locked Wheels

The first couple of behaviours presented are gaits that are accomplished without the use of wheels and have been successfully implemented on previous platforms. Shown in Fig. 2.16 and Fig. 2.17, a high speed bounding gait and a pronking gait were simulated with the wheels locked-out or braked.

The high speed bound embodies a tremendous amount of energy that can be redirected and used to clear a variety of obstacles. The sequence in Fig. 2.18 is an example of such use of the energy. Here, the robot positions the legs so as to direct all the momentum into one large *leap* with enormous ground clearance. The figure depicts a large ledge, but it could be used for any number of obstacles such as ditches or muddy swamps.

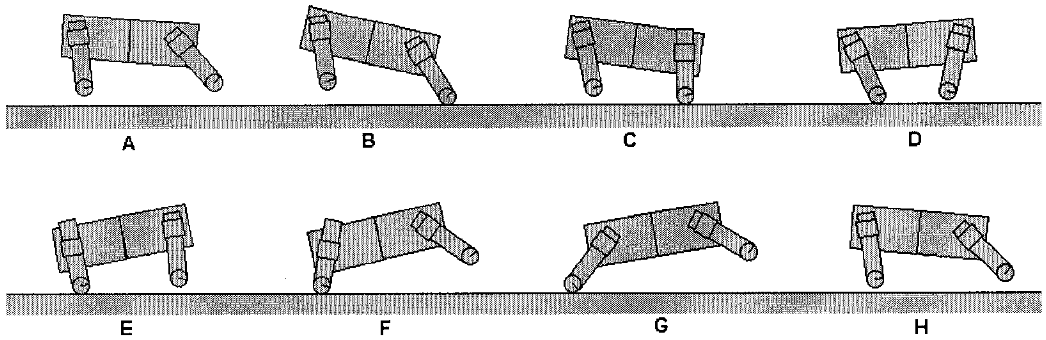

Fig.2.16. High speed bounding gait, approx. 3 m/s (l_{body} = 0.5 m).

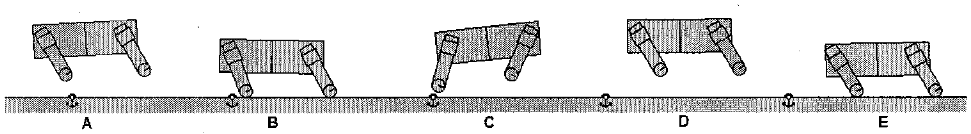

Fig. 2.17. Pronking gait (l_{body} = 0.5 m).

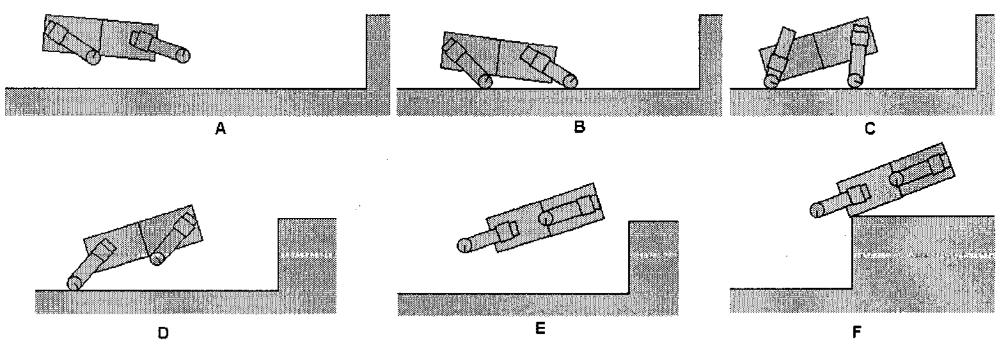

Fig. 2.18. High speed bound used to negotiate large ridge (l_{body} = 0.5 m).

2.3.2. One Leg Bounce

This behaviour is a basic dynamic movement that exploits the hybrid wheel-leg design and a first step to many other behaviours. The basic sequence of maneuvers is depicted in Fig. 2.19. The robot begins sweeping its left legs when touchdown is detected (Fig. 2.19.B), which is sensed the moment the leg spring begins to compress. The body then pitches downwards as the leg spring compresses (Fig. 2.19.B), while both the hip and the wheel actuation sweep the leg outwards. This acts to pitch the body upwards while it is still pitching downwards, further compressing the spring. When the body begins to pitch upwards (Fig. 2.19.C), the leg continues to sweep outwards, pushing the body upwards with the compliance. Throughout the entire sequence the right leg is kept vertical with respect to the ground.

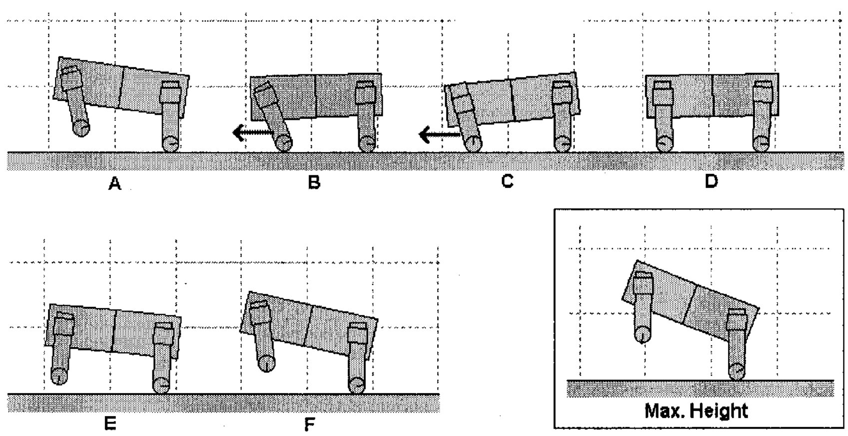

Fig. 2.19. One leg bounce sequence (l_{body} = 0.5 m).

This sequence is repeatedly performed, each time gaining height in roughly the same spot. However, actuation limitations restrict the maximum obtainable height as illustrated in the figure. The higher the robot bounces, the more the spring compresses and therefore the more acceleration the robot experiences. After a critical point, the motor's no-load speed restricts the robot from adding any more energy into the bounce. That is, if the leg cannot swing fast enough to cause a vertical displacement greater than that delivered by the compliance, then the leg will not add energy to the robot. A utility for this maneuver could be to drive the right wheel along the ground, once it has reached a desired pitching height, to drive the robot's body over an obstacle. This utility is illustrated in Fig. 2.20.

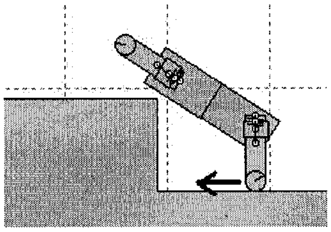

Fig. 2.20. Obstacle clearance following one leg bounce ($l_{body} = 0.67$ m).

2.3.3. Two Leg Bounce

This behavior is identical to the one leg bounce except that both legs are used to supply the robot with vertical energy. The basic sequence of maneuvers in Fig. 2.21 is repeatedly performed, each time gaining height in roughly the same spot. Just as in the one leg bounce, actuation limitations restrict the maximum obtainable height. This maneuver is a good first step for any maneuver that would require a large initial ground clearance or a large amount of energy stored in the compliance (i.e. pronking).

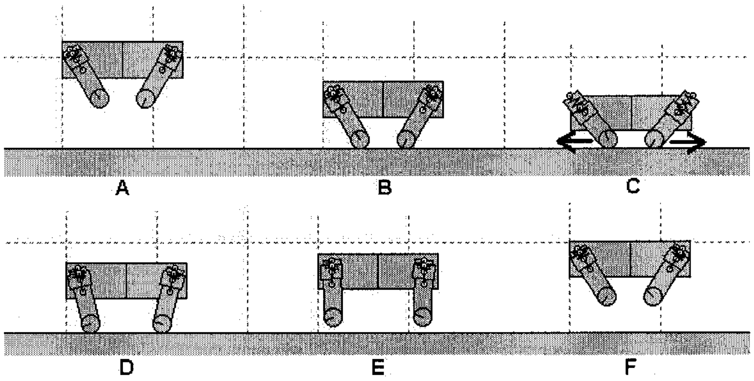

Fig. 2.21. Two leg bounce sequence ($l_{body} = 0.67$ m).

2.3.4. Inverted Pendulum Control

This behaviour allows the robot to suspend its body in the air in a controlled manner. It begins with the one leg bounce and as soon as it has reached the maximum height, it performs the start-up sequence of maneuvers depicted in Fig. 2.22. The moment the left leg lifts off, the right wheel drives towards the left, which pitches the torso much higher than the one leg bounce. The right wheel continues to drive leftward until the robot is vertical. As soon as the torso is perpendicular to the ground, the bottom (right) hip is locked and an inverted pendulum controller maintains the torso suspended vertically.

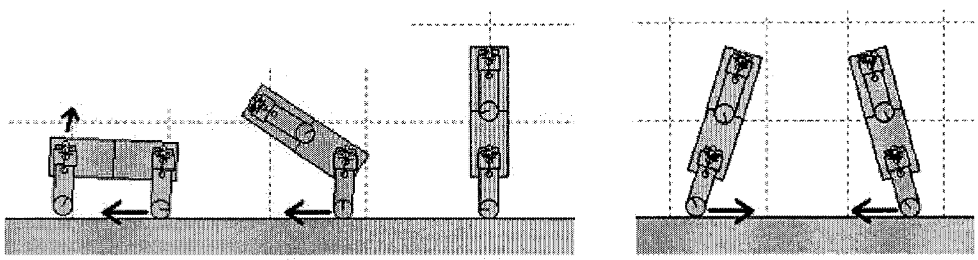

Fig. 2.22. Inverted pendulum controller ($l_{body} = 0.67$ m).

The inverted pendulum controller maintains the torso's orientation by commanding wheel angles that drive the robot in the corrective direction (Fig. 2.22, right). It simply adds/subtracts an angle proportional to the amount of correction required to the current wheel angle. This proportional angle is related to the torso angle through a PD controller,

$$\theta_{desired} = \theta_{current} + K_D(90° + \theta_{torso}) + K_V\dot{\theta}_{torso} \quad (2.15)$$

If the desired torso angle is set to one offset from the 90 degrees depicted in Fig. 2.22.C, the platform maintains this desired body pitch by driving in the direction it is leaning towards. This could enable the robot to overcome obstacles in the same fashion as illustrated in Fig. 2.20, but with more precision and larger clearance than the one leg bounce technique.

2.3.5. One Leg Flip

This maneuver is depicted sequentially in Fig. 2.23, which is executed in the same fashion as the start-up maneuver for the inverted pendulum controller. Except in this behaviour the wheel continues driving leftward after the torso is vertical, causing the torso to flip about the right leg (Fig. 2.23.B to D). Again the right leg is always positioned vertically with respect to the ground, maintaining a pivot about which the torso swings. When the robot reaches position D in the figure, the wheel brakes and the torso swings downward on the other side of the robot. At the same time, the left leg (in flight) swings around 180 degrees to absorb the impact with the compliance. The compliance then returns the torso's momentum, which pitches the body upwards again (Fig. 2.23.G). The platform then drives rightward and repeats the maneuvers to flip the robot in the other direction. Thus, positions A and K in the figure are more or less the same position.

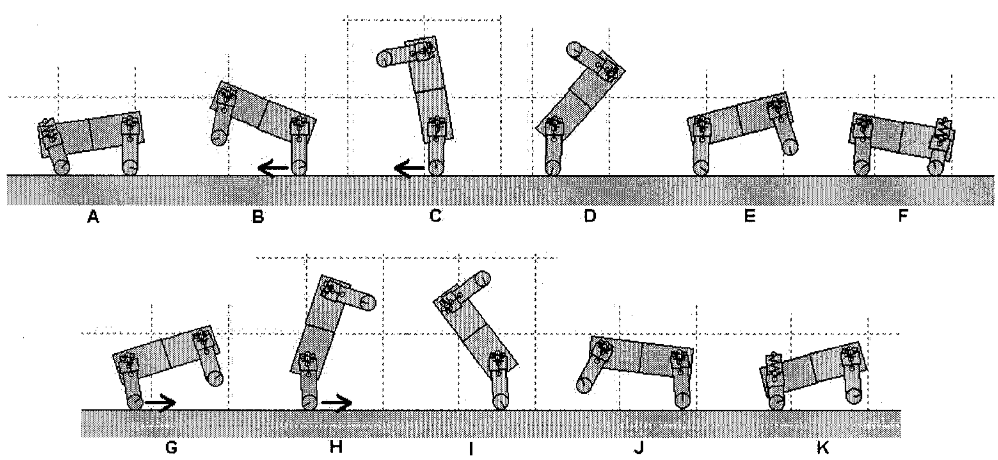

Fig. 2.23. One leg flip sequence ($l_{body} = 0.67$ m).

These principles can be used to shorten the time required by the one leg bounce to reach its maximum height. If the maneuver performed in Fig 2.23.B is executed during positions D or E in Fig. 2.19, it results in more height gained for that cycle of the one leg bounce. The wheel direction can then be reversed when the body is falling (Fig. 2.19.F) to pitch the torso downward more quickly.

It is possible to capitalize on the high energetics of the one leg bounce by performing another maneuver immediately afterwards, providing there is a proper transition. An example of such behaviour is the forward flip depicted in Fig. 2.24. Notice that Fig. 2.23.K. and Fig. 2.24.A. are captured at the same moment in time, making Fig. 2.24 a continuation of the events in Fig. 2.23. This forward flip executed in the figure is made possible through the exploitation of the energy stored in the compliance from the one leg bounce. After the forward flip is executed (Fig. 2.24.J), the robot has a very large amount of ground clearance that could be redirected to generate a large leap or any number of other behaviours.

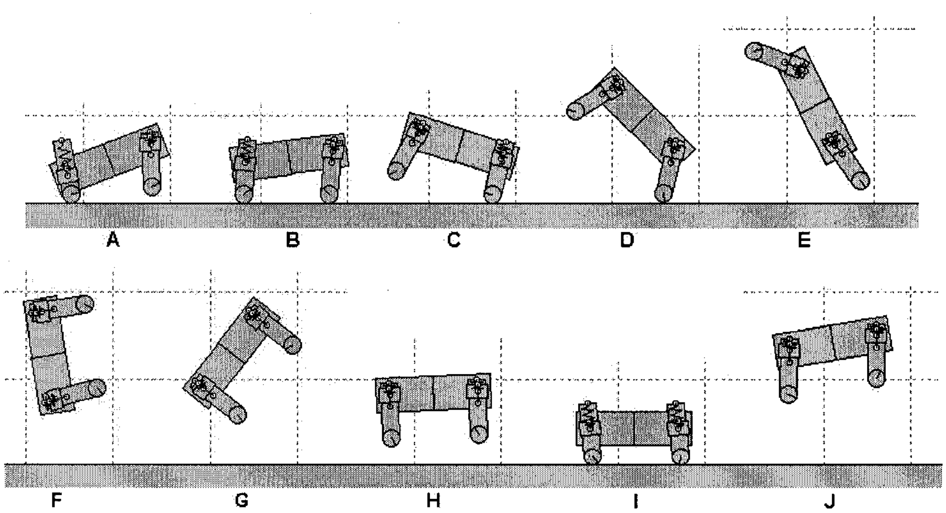

Fig. 2.24. Forward flip after one leg bounce (l_{body} = 0.67 m).

2.3.6. Back Flip

The basic back flip maneuver is depicted sequentially in Fig 2.25. The robot begins lying on the ground with both of its legs directed forward and commands both legs to rotate 270 degrees rearward. The sweeping of the front leg quickly lifts the front end in the air and gives the torso an initial rotational velocity about the rear hip. The rear leg then continues to torque the torso about its hip, while lifting the torso in the air. The wheel on the front leg is left free to roll, while the wheel on the rear leg is actively driven. The wheel on the rear leg controls the amount of body rotation at lift-off in the manner depicted in Fig. 2.25.D. In the sequence portrayed in Fig. 2.25, both legs land on the ground roughly at the same time following the back flip (see positions H and I). However, if more or less rear wheel rotation occurs around position D, the front or rear legs land at different moments in time.

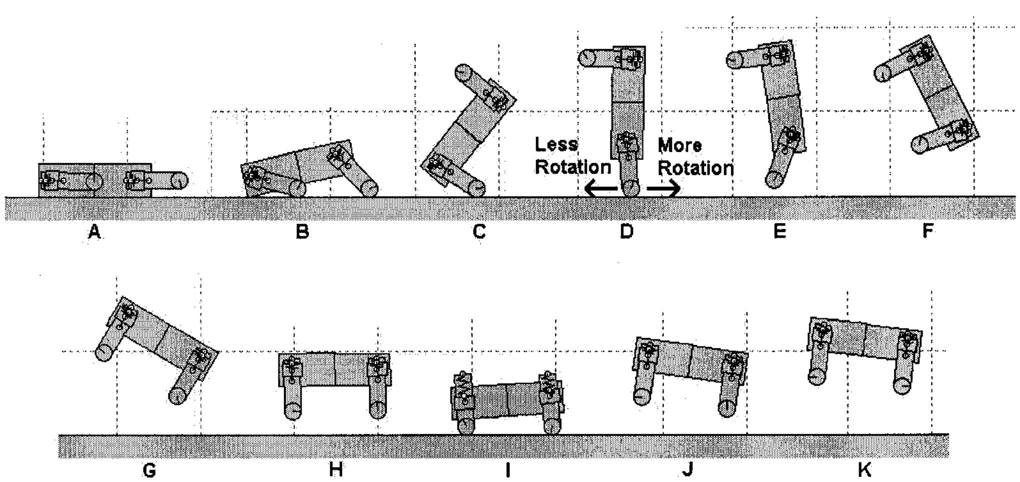

Fig. 2.25. Back flip sequence ($l_{body} = 0.67$ m).

This maneuver only causes a small horizontal displacement rearwards, as the motion is mainly a vertical leap with rotation. In other words, it is more like a back flip and not a back handspring. As can be seen in Fig. 2.25.K., the robot obtains a large amount of ground clearance after performing this maneuver. Again, the energetics of this large ground clearance can be exploited to perform various other dynamic behaviours following the back flip. Since it obtains this large height much more quickly than other maneuvers, it is a preferable behaviour for gaining such height.

Fig. 2.26 illustrates using the back flip to get over a high step. It performs the same sequence of maneuvers as the regular back flip except that the robot initially drives towards the obstacle. As the step simulated in Fig. 2.26 is significantly higher than the platform, the maneuver gives the platform tremendous obstacle negotiating capabilities. The same behaviour could be implemented to clear ditches or any number of obstacles. The high utility of the back flip exemplifies the advantages of exploiting the dynamic capabilities of a robot.

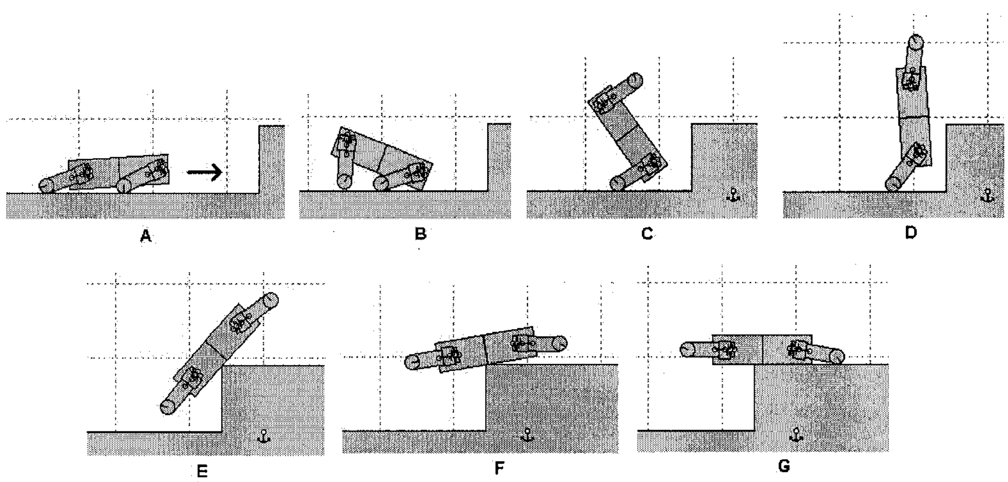

Fig. 2.26. Driving towards and back flipping onto a ledge (l_{body} = 0.67 m).

A less energetic maneuver that combines the back flip and the inverted pendulum controller is illustrated in Fig. 2.27. It begins with a *slower* back flip and merges into the inverted pendulum controller. Again, the back flip is preferred over the one leg bounce as it can obtain the final behaviour, the inverted pendulum controller, with a much quicker start-up time.

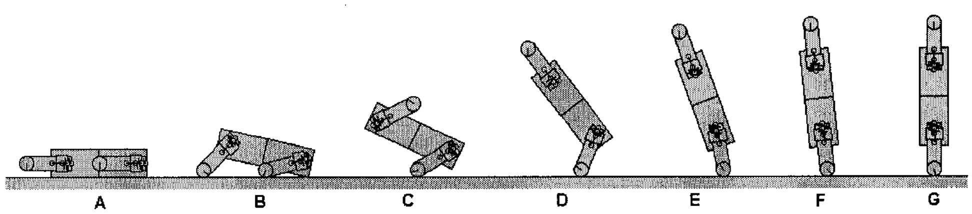

Fig. 2.27. Back flip to inverted pendulum controller (l_{body} = 0.67 m).

2.3.7. Pronking with Wheels

This gait starts-up with the back flip or the two leg bounce to obtain a large initial ground clearance. After it has obtained the maximum possible height, the sequence of maneuvers depicted in Fig. 2.28 enables the robot to pronk using its wheels. After only rough tuning, speeds over 1 m/s have been obtained in simulation. Upon touchdown, the rear leg hits first because the rear legs are set to smaller angles than the front legs. Immediately, the rear wheel drives the robot in the direction shown by the arrow in Fig. 2.28.B., while the front wheel is set to remain passive. This not only gives the robot a forward velocity, but also aids to pitch the front end upwards. When the front leg's compliance reaches the bottom of its stroke (Fig. 2.28.C), the front legs swing towards the body with the assistance of the front wheels (Fig. 2.28.D). This adds vertical energy to the robot and pitches the front end of the robot upwards. This front leg swing is the main mechanism of body pitch control for this mode of pronking. Note that the rear leg does not swing during stance, but only adjusts its touchdown angle during flight to accommodate speed changes.

The ground clearance is maintained owing to a couple of factors. Firstly, the wheels input most of the energy used to increase or maintain the forward velocity.

Thus, the legs are not used to input forward acceleration and are used solely to maintain the ground clearance. Secondly, in a pronk the rear compliance always receives more than the required energy to return the robot to the same height. This is a byproduct of adding forward momentum to a platform, as it is displaced partially to the rear of the robot. Thus, any vertical energy lost at touchdown is more than adequately compensated for in the rear legs. With no need to use the rear legs to gain any height in the rear end of the robot, it can be set to a constant angle. The front legs are then used solely to compensate for the lost energy in the front; sweeping more to pitch the front upwards and less to pitch it downwards. As the robot's forward velocity increases, the set point angles of the legs are adjusted slightly to maintain the gait.

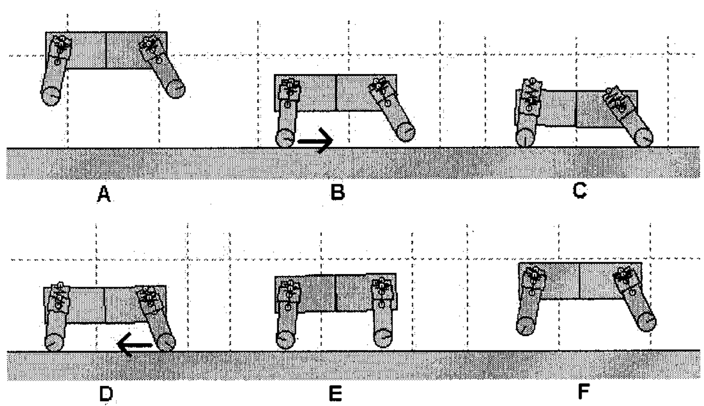

Fig. 2.28. Pronking sequence reaching speeds over 1 m/s (l_{body} = 0.67 m).

Chapter 3

Design of Testbed

A full systems design of a testbed capable of executing the dynamic behaviours presented in *Chapter 2* was completed. This prototype will prove the feasibility of such behavioural feats for autonomously powered platforms, demonstrate their wide utility and pave the way for their realization on ruggedized outdoor platforms. A complete set of assembly drawings for the prototype are in Appendix B and should be referred to for any necessary clarification.

3.1. Design Specifications

A prototype sized large enough to negotiate reasonably sized obstacles and to carry a useable payload was desired. However, it was also desirable to have a smaller sized platform on which it was relatively easy to perform experiments in the laboratory environment. Due to the size of a few mandatory components (i.e. PC104 stack), the platform can only be made so small. A prototype with body length of approximately 0.5 m was selected as a good compromise of these issues. The design specifications for the 0.5 m ANT prototype, which were deduced using the methods outlined in *Chapter 2*, are contained in Table 3.1. The wheel actuation specifications are not included in this table as they were deduced using alternative methods that are discussed in the *Section 3.22. Actuation Design* below.

Table 3.1. Design specifications.

Description (units)	Value
Body Length (m)	0.5
Body thickness (m)	0.16
Body width (m)	0.4
Leg length (m)	0.18
Ground Clearance (m)	0.13
Body mass (Kg)	16.3
Leg & wheel mass (Kg)	2.68
Total mass (Kg)	19
Hip Torque (Nm)	16.5
Hip No Load Speed (rpm)	330
Hip separation (m)	0.35
Wheel Diameter (m)	0.06
Spring Constant (N/m)	5000

3.2. Actuation Design

3.2.1. Hip Actuation

In Fig. 3.1 below, regions critical to performing various behaviours are labelled on the torque-speed curve for the hip actuation. This figure shows the dynamic compromises associated with using alternative gear ratios and emphasizes that the ANT platform exploits the entire range of the hip actuation to achieve the dynamic maneuvers.

The motor, gearhead and transmission components selected to achieve the hip actuation requirements are contained in Table 3.2. A Maxon 90 W brushed DC motor, a 2 stage planetary gearhead (15:1 reduction) and a set of timing belt pulleys were chosen. These components yield an output of 16.7 Nm of stall torque with a no load speed of 332 rpm, meeting the design targets. The reason the entire reduction is not done with the motor's gearhead, but rather in conjunction with a pulley reduction, is due mainly to space constraints in the robot. Looking at the top view of the robot in Fig. 3.2., it can be seen that placing two motor/gearhead/encoder packages along the leg axis would result in a very wide robot. The belt pulleys allow the motors to be staggered, offsetting them from the leg axis, enabling a smaller body. This also allows for wiring to run from the leg into the body freely, via a hole through the hip shaft, to connect electronic hardware. Using external pulleys also enables post-construction versatility, as alternate pulleys can be employed to change the reduction.

An *HTD* timing belt system was used so that there would be no slipping, ensuring for precise rotation of the hips. Pictured in Fig. 3.3 is a hip motor/gearhead combination packaged with a digital encoder. In Fig. 3.4, both the 22 and 32 tooth *HTD* (5mm pitch) pulleys, as well as the 9mm wide timing belt, are shown. For more information please refer to the bill of materials and manufacture's sheets included in the appendices.

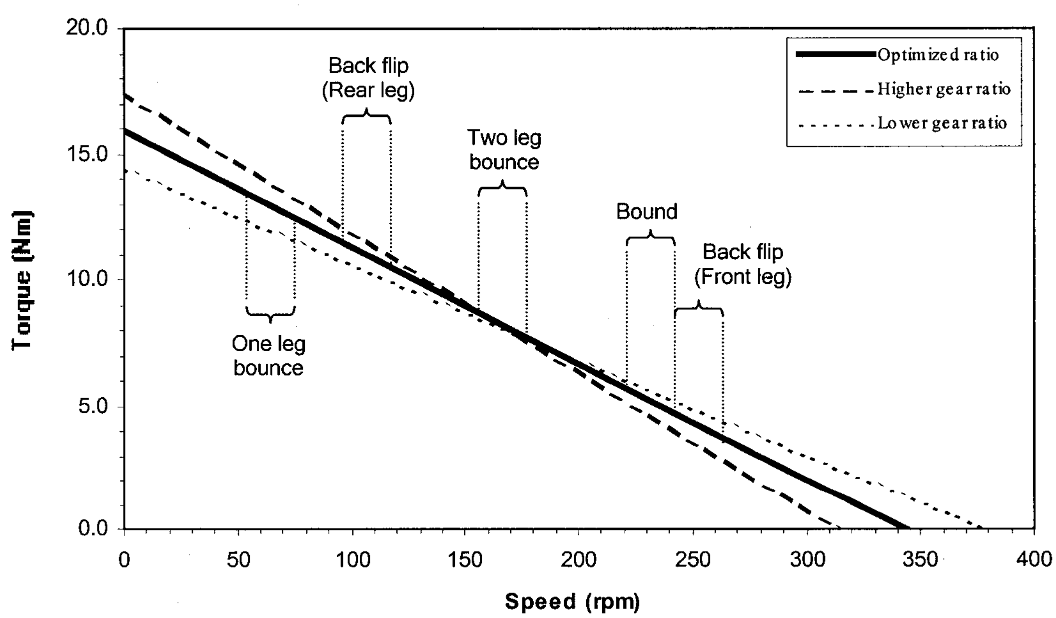

Fig. 3.1. Critical regions of performance for various behaviours on the hip's torque-speed curve.

Table 3.2. Hip actuator components [44][60].

Hip Motor Maxon RE 35 (118777)	
Power (W)	90
Stall torque (Nm)	0.949
No load speed (rpm)	7220
Voltage (V)	30
Starting current (A)	24.4
Torque constant (Nm/A)	0.039
Mass (Kg)	0.34

Hip Gearhead Maxon GP 42C (203116)	
Reduction	15
Max. efficiency (%)	81
Max. cont. torque (Nm)	7.5
Max. discont. torque (Nm)	11.3
Mass (Kg)	0.36

Hip Output with Timing Pulleys HTD Timing Belt Pulleys (32/22)	
Pulley reduction (32/22)	1.45
Stall torque (Nm)	16.7
No load speed (rpm)	332
Mass (Kg)	0.1

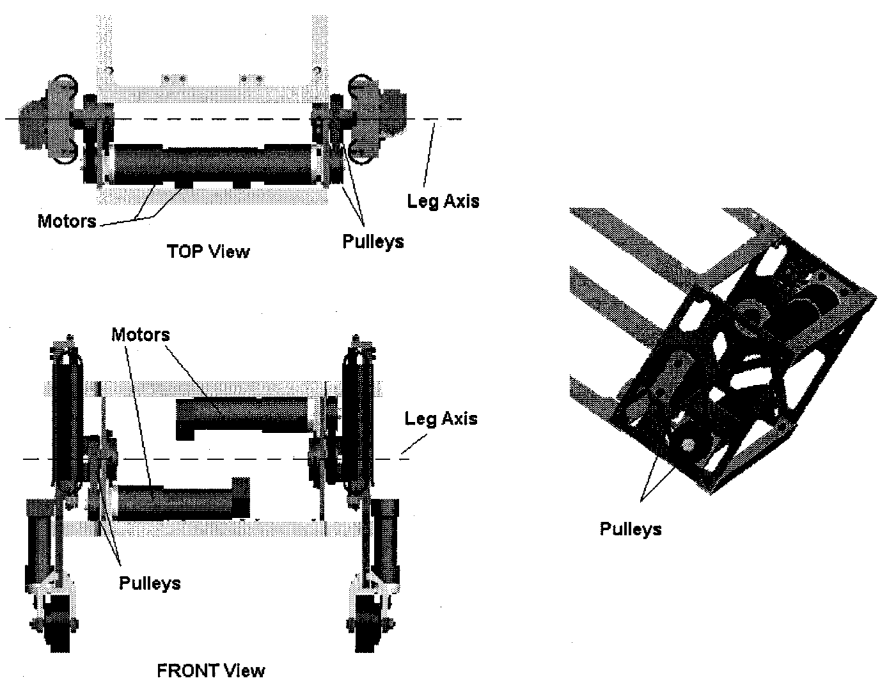

Fig. 3.2. Hip motor offset using belt pulleys.

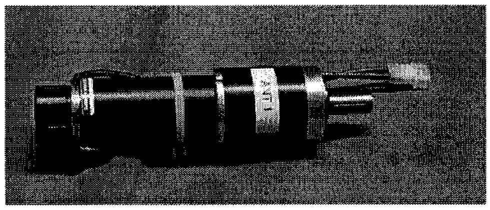

Fig. 3.3. Hip motor/gearhead with encoder.

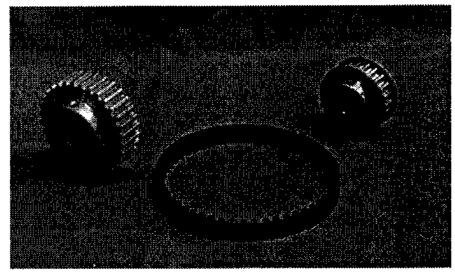

Fig. 3.4. Timing belt pulleys and belt.

3.2.2. Wheel Actuation

The design of the wheel actuation was undertaken much differently than the hip actuation. The behaviours demanding the highest speeds from the wheels, the one and two leg bouncing, established a minimum for the no load speed. In Fig. 3.5, the wheel speed during the simulation of these maneuvers is plotted over time periods when the platform is maintaining the maximum height. From the plots it can be seen that a no load speed of 500 rpm would be sufficient for the successful execution of these maneuvers.

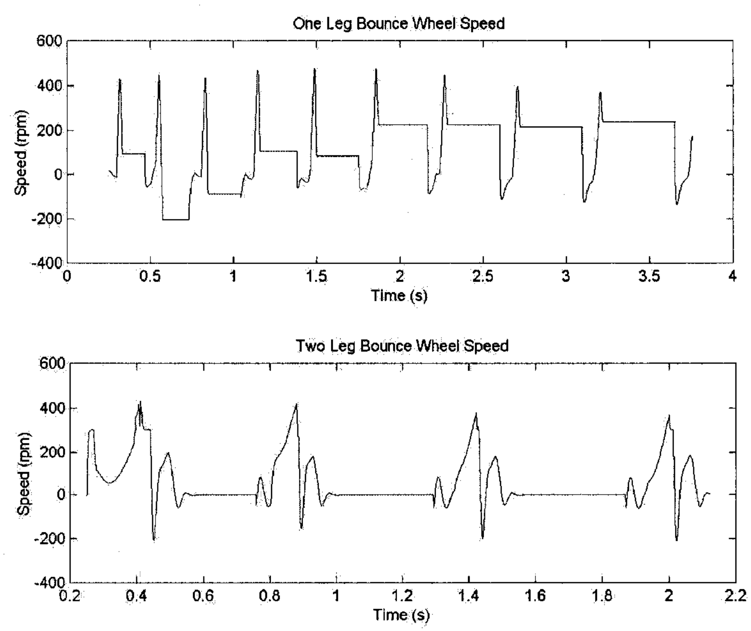

Fig. 3.5. Wheel speeds for one and two leg bouncing.

The torque requirement at the wheels is based on the more static mode of locomotion - incline climbing. The objective was to have enough wheel power so that the platform could climb a slope of at least a 45 degrees at 20% of the no load speed, using only two wheels. If the power was sufficient to do so, the wheels would also have enough power to climb a 45 degree slope using 4 wheels at over half the no load speed. Using two wheels, each wheel would require 2.0 Nm of torque to climb a 45 degree slope. Therefore, 2.5 Nm of torque is the required stall value of the motor to ensure a climbing speed of 20% no load. With 2.5 Nm of stall, the platform will be able to climb a 45 degree slope using all four wheels at 60% of the no load speed.

The wheel actuation was therefore required to have a stall torque of 2.5 Nm and a no load speed of 500 rpm. The motor, gearhead and transmission components selected to satisfy these requirements are in Table 3.3. A Maxon 20 W brushed DC motor, a Maxon 1 stage planetary gearhead (4.8:1 reduction) and a set of bevel gears (3:1 reduction) were chosen. These components yield an output of 2.5 Nm of stall torque with a no load speed of 715 rpm, which more than satisfied the requirements. The reason the entire reduction was not done with the motor's gearhead, but rather in conjunction with a set of bevel gears, was due to the 90 degree angle between the wheel axis and motor axis. Since a bevel gear, or another right angle transmission, would have to be employed, using a ratio other than 1:1 to reduce the requirements of the gearhead was sensible. Using a larger ratio than 1:1 also increases the distance between the wheel axis and the motor (see Fig. 3.6, variable *d*), which reduces the mass centered at the wheel and therefore the rotational inertia of the leg.

The selected wheel actuation will enable the platform to climb a 45 degree incline, assuming no slipping, using two wheels at a speed of 0.45 m/s, or at a speed of 1.35 m/s using four wheels. Assuming on flat ground that the motors could reach at least 80% of their no load speed, the cruising speed of the platform will be at least 1.8 m/s. Pictured in Fig. 3.7 is a wheel motor/gearhead combination packaged with a digital encoder. In Fig. 3.8, both the 15 and 45 tooth (mod. 1) bevel gears are shown. For more information on these items, please refer to the bill of materials in Appendix C and the manufacture's data sheets in Appendix D.

Table 3.3. Wheel actuator components.

Wheel Motor Maxon RE 25 (118751)	
Power (W)	20
Stall torque (Nm)	0.218
No load speed (rpm)	10300
Voltage (V)	18
Starting current (A)	13.5
Torque constant (Nm/A)	16.1
Mass (Kg)	0.13

Wheel Gearhead Maxon GP 32C (233147)	
Reduction	4.8
Max. efficiency (%)	80
Max. cont. torque (Nm)	1.0
Max. discont. torque (Nm)	1.25
Mass (Kg)	0.118

Wheel Output with Bevel Gears SDP Straight Bevel Gear (Mod. 1)	
Reduction (45/15)	3
Stall torque (Nm)	2.51
No load speed (rpm)	715
Mass (Kg)	0.08

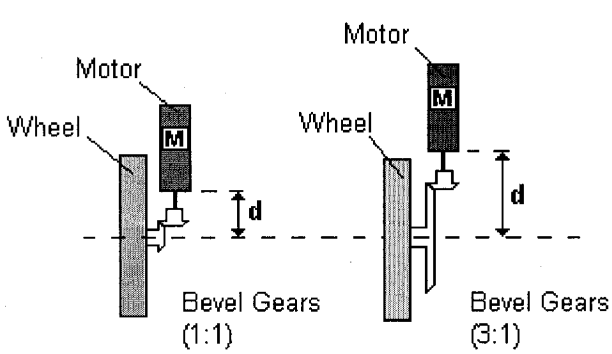

Fig. 3.6. Larger bevel gear moves the motor up the leg

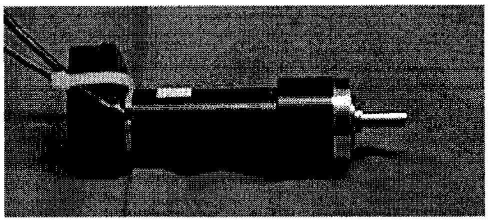

Fig. 3.7. Wheel motor/gearhead with encoder.

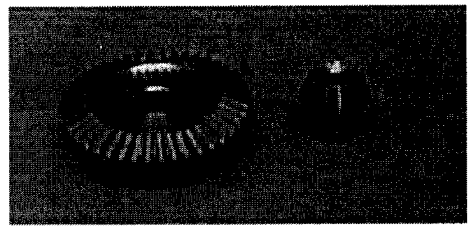

Fig. 3.8. Bevel gears for wheels.

The nominal voltage of the wheel motors is 18 V, while the hip motor's nominal voltage is much higher at 30 V. Thus, the power supply will be rated for at least 30V creating an opportunity to increase the performance of the wheel motors. Recall the relationship between the back EMF and the rotor speed of a DC motor,

$$EMF = K_w w, \tag{3.1}$$

where Kw is the speed constant and w is the angular speed; the back EMF increases as the speed of the rotor increases. Using the model of a DC motor in Fig. 3.9, the back EMF applies a voltage to the armature resistance (R_a) opposing the voltage applied by the supply at the motor terminals. So as the speed increases, the current through the windings decreases. Therefore, at higher speeds the terminal voltage may be raised beyond that of the nominal voltage without drawing large currents that could cause the motor to exceed its permissible thermal limitations. This can be safely accomplished so long as the speed is kept below the maximum permissible speed to avoid commutation problems that could lead to premature motor failure. Abiding by this, the torque speed curve of the motor can be enhanced to that depicted in Fig. 3.10, safely achieving higher performance from the motor. Using this technique to enhance the operating traits of the wheel motors, the cruising speed will be increased to approximately 2 m/s and the general performance of the motors will be higher than that observed in simulation.

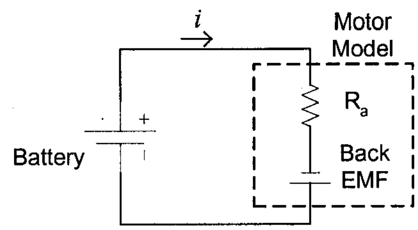

Fig. 3.9. Motor and battery schematic

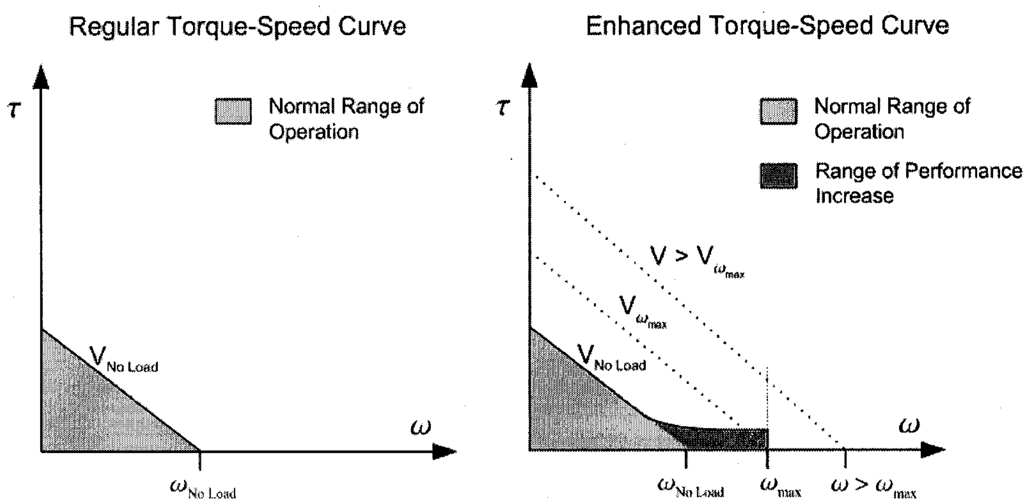

Fig. 3.10. Torque-speed curve with voltage increase at high speeds

3.2.3. Actuator Performance

Two key behaviours were simulated with the final geometry and the selected actuation parameters to obtain projected performance data for the testbed's actuation. The two dynamic behaviours used were the back flip and standing up, as their actuation demands are the highest of all the behaviours. The back flip maneuver exemplifies the performance requirements of the hip actuation, while standing up exemplifies the limits associated with wheel actuation. In order to confine the study of the back flip maneuver to that of solely hip actuation, the back flip performed for these tests was executed using unactuated wheels. In the figures below, the torque, speed and power consumption of the actuators are plotted over the time indicated sequentially in the appropriate diagram of the maneuver. A torque-speed plot is also given for each of the two maneuvers to highlight that the platform is operating at the limits of the torque-speed curve the majority of the time.

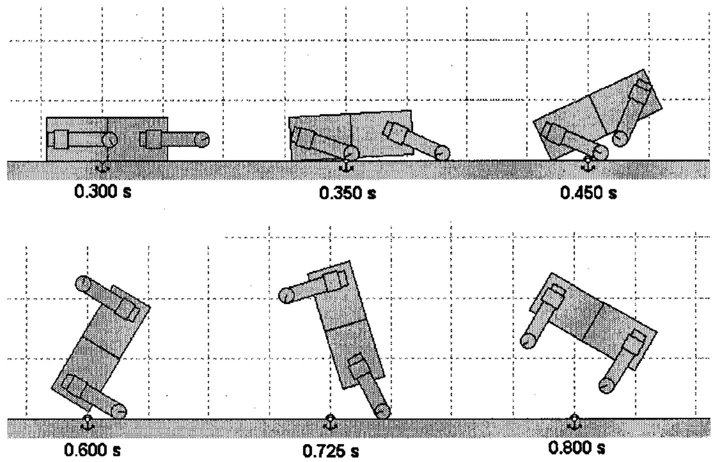

Fig. 3.11. Back flip with sequential time labels

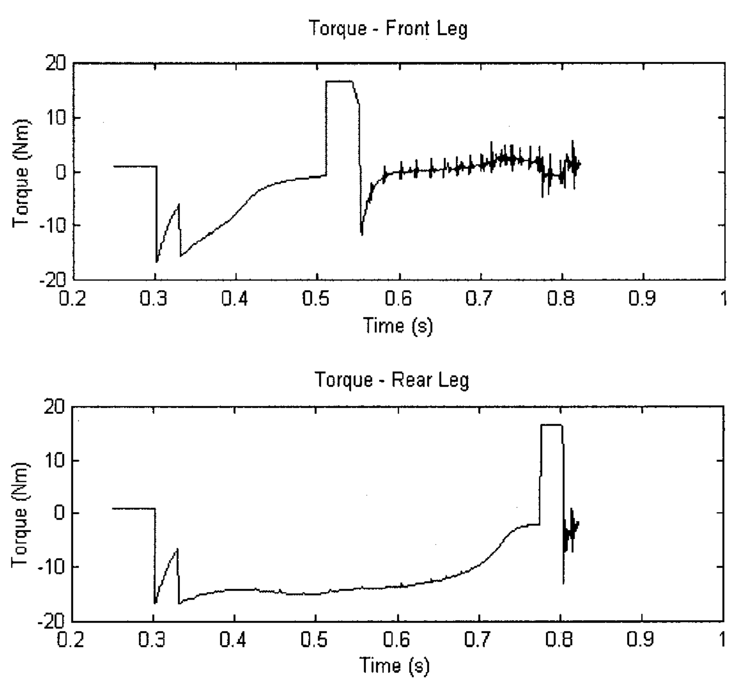

Fig. 3.12. Leg torque during back flip

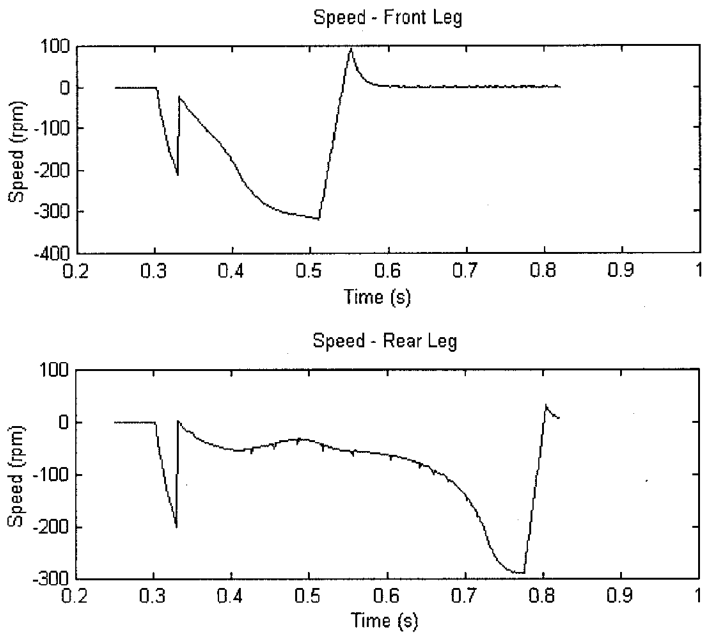

Fig. 3.13. Leg speed during back flip

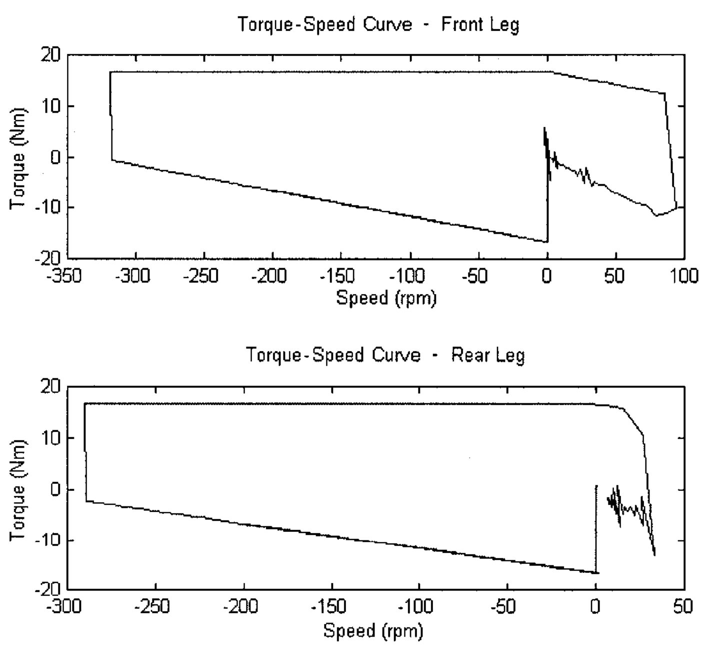

Fig. 3.14. Torque-speed plot for legs during back flip

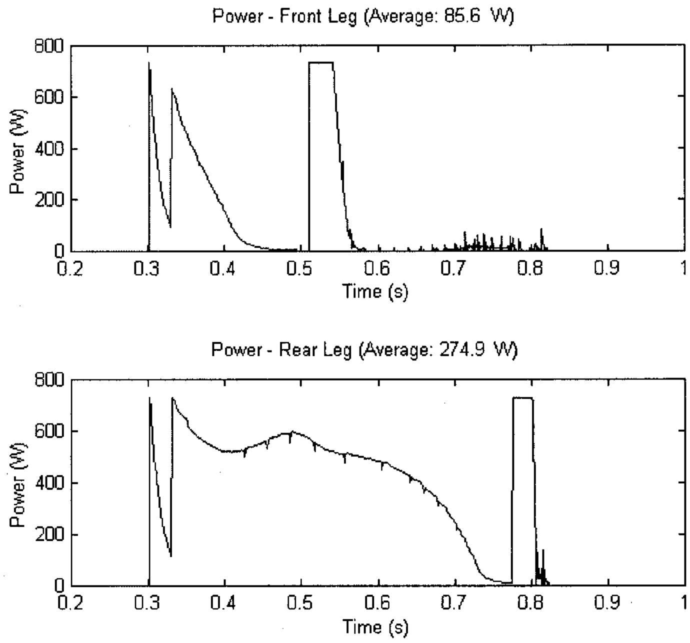

Fig. 3.15. Leg power consumption during back flip

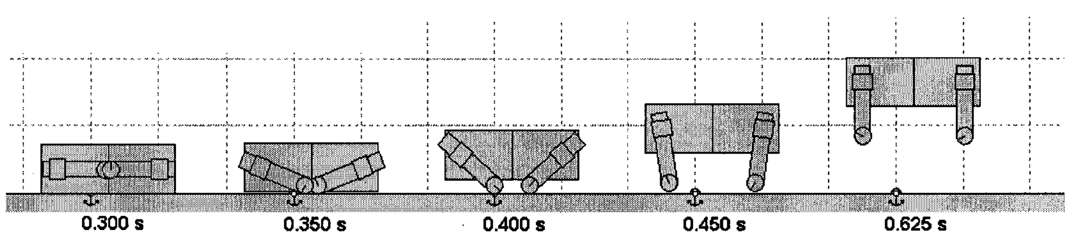

Fig. 3.16. Standing up with sequential time labels

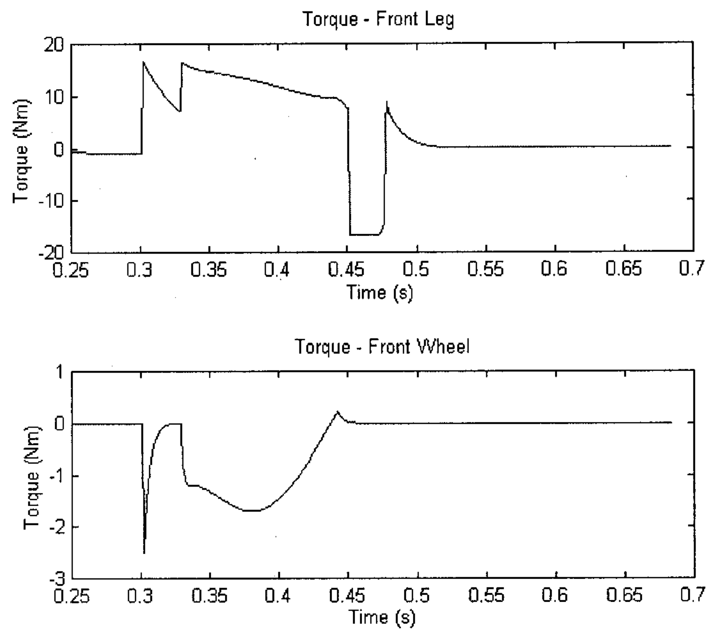

Fig. 3.17. Leg and wheel torques while standing up

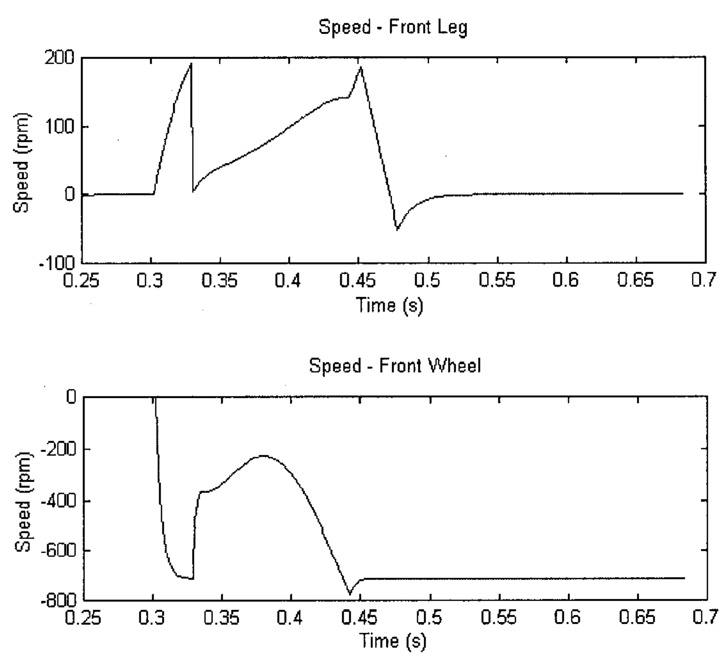

Fig. 3.18. Leg and wheel speeds while standing up

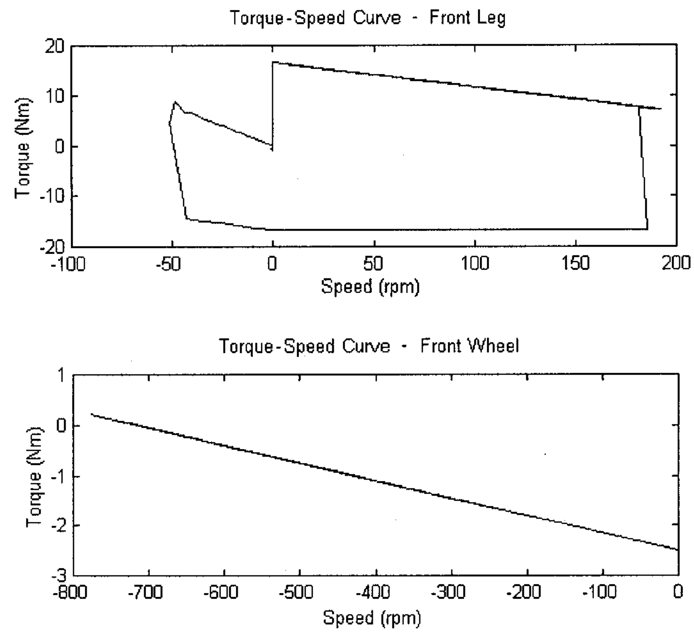

Fig. 3.19. Torque-speed plot for legs and wheels while standing up

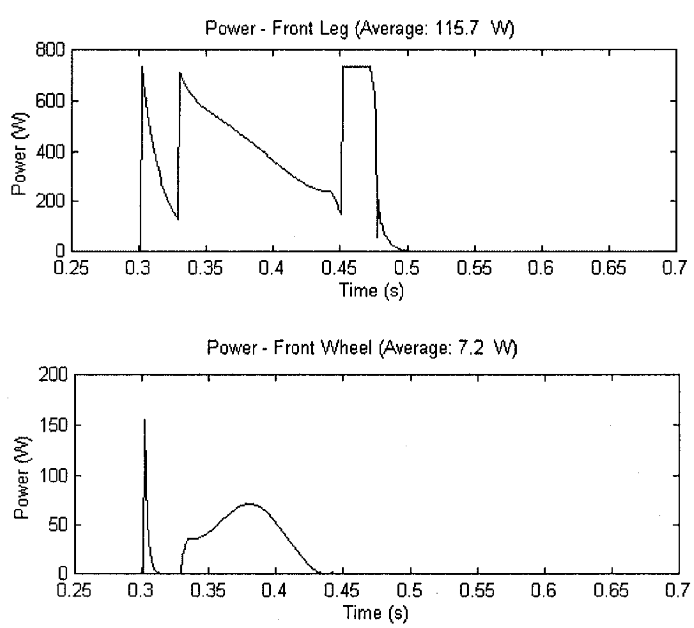

Fig. 3.20. Leg and wheel power consumption while standing up

The above plots of the actuators performance indicate that the behaviours could be executed with a slightly higher power efficiency. Between the 0.50 s and the 0.55 s marks during the back flip (see Fig. 3.11), as well as between the 0.45 s and the 0.50 s marks while standing up (Fig. 3.16), the hips abruptly stop the swinging of the legs in flight and hold their positions. The legs are forced from their maximum rotational speed down to a zero rotational speed in roughly 0.05 s, generating the large spikes in hip torque shown in Fig. 3.12. and Fig. 3.17. On the testbed, the leg speeds will be gradually decreased, or *ramped* down, to decrease the power consumption without altering the behavioural performance.

3.3. Electronics and Sensors

3.3.1. Sensors

To determine angular joint positions, encoders on the motor shafts are packaged with the *Maxon* motors (see Fig. 3.3 and 3.7). Specifically, the motors are assembled with *Hewlett Packard HEDS 5540*A incremental digital encoders (see Fig. 3.21) which have 500 counts per revolution [43]. However, quadrature decoding will be employed to obtain 2000 counts per revolution, or better than 0.2 degree resolution. The angular velocity of the joints will be obtained by differentiating the joint position data over time. As these encoders have no means to detect an absolute position, only incremental steps relative to their starting position, the hips will be calibrated with the use of Hall Effect sensors to *zero* the joint positions.

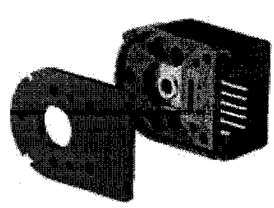

Fig. 3.21. *Hewlett Packard HEDS 5540*A digital encoder.

The digital hall effect sensor used for this purpose is the *Micronas HAL506UA-E* [45][52] and is pictured in Fig. 3.22 with its complementary *Hamlin H-33* permanent magnet [45]. The sensor will be mounted on the body at the hip, while the magnet will be attached to a pulley mounted on the leg. The trigger point, or the *zeroed* leg angle, will be determined experimentally and used by the controllers at run-time to calibrate the leg angle. Upon start-up, the robot will swing its legs until they trigger their corresponding hall effect sensors, thereby setting the encoder signal in the controller to the experimentally determined angle. It should be mentioned that the wheels do not require *zeroing* as absolute positioning is not required, rather only the encoders relative positioning.

Fig. 3.22. *Micronas HAL506UA-E* hall Effect sensor and *Hamlin* magnet.

Most of the behaviours' controllers require knowledge of toe touchdown and the length of the leg compliance during stance phases. Both of these are acquired through a linear potentiometer mounted on the leg. This sensor allows for easy acquisition of the leg length. Touchdown is detected the moment the leg compliance shortens, while flight is deduced if the leg is at full extension. *Midori LP-100FP* 5kΩ potentiometers [46], pictured in Fig. 3.23, were chosen because of their precise ±1% linearity, small diameter and sufficient stroke length of 100 mm. Their 50G rating also means that they will most certainly withstand any accelerations the robot will undergo and they weigh only 35 g.

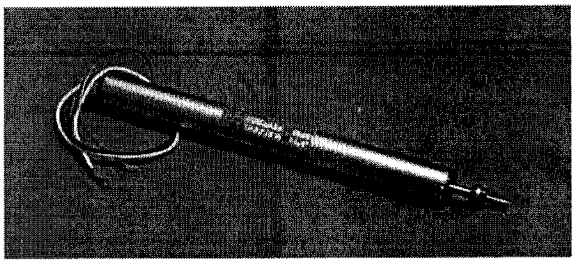

Fig. 3.23. *Midori LP-100FP* 5kΩ potentiometer.

Some the behaviours, such as the one leg bounce or inverted pendulum controller, require knowledge of the body pitch. This will be obtained with the use of angular velocity sensors, specifically piezoelectric vibrating gyroscopes. Only one single axis unit will be implemented at first, as that is all that should be required to measure body pitch. However, future behaviours may require three axis acquisition, in which case three units will be appropriately mounted. *MuRata's Gyrostar ENC-03JA* [55] was selected because of its low cost, small size and weight of only 1 g. The ENC 03JA can handle velocities up to ±300°/s at a 50 Hz. response with ±5% full scale linearity. The angular velocity obtained from the sensor will be integrated to yield the angular position used by the controllers. To reduce the effect of drift, the signal will be reset or zeroed at every touchdown, which is sensed using the potentiometers in the leg. Below is a picture of one single axis unit.

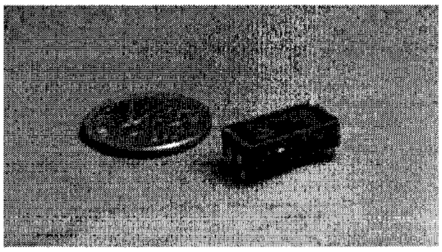

Fig. 3.24. *MuRata's Gyrostar ENC-03JA* single-axis gyroscope.

3.3.2. Amplifiers

In order to realize the performance observed in simulation, the selected motors must be able to draw the current they require at their nominal voltages. This was achieved by selecting amplifiers (motor drivers) that could deliver adequate current at the specified voltage. For the hip actuation, *Advanced Motion Control's 25A8* pulse width modulation (PWM) servo amplifier was chosen (see Fig. 3.25) [53]. They are designed to drive brushed DC motors at a high switching frequency and require only a single unregulated DC power supply. As well, they are fully protected against over-voltage, over-current, over-heating and short-circuits across motor, ground and power leads. They can operate in numerous modes including open loop, voltage, IR compensation, velocity, current (torque), analog position loop and digital loop.

Fig. 3.25. *AMC 25A8* Servo amplifier for hip's motor driver.

The 25A8 models have a peak current of 25 A and a maximum continuous current of 12.5 A. They operate between 20 and 80 V and weigh 270 g each. The ANT prototype will operate in current (torque) mode, which means that a reference input voltage commands a proportional torque output. They also have a current monitoring pin which will be used to log the torque of the motors. Other Advanced Motion Amplifiers have been successfully implemented on previous ARL robots, strengthening the decision to use this amplifier.

To drive the wheel motors, a custom designed motor driver board used by the Robotic Hexapod (RHex) project in the ARL will be employed [61]. It weighs less than commercial drivers at 440 grams and has had many successful years of implementation on the RHex platform. The board can drive up to 6 motors; each motor driven by single ended PWM motor control contained in an *Apex Microtechnology SA60* hybrid module [54]. The *SA60* contains a 100 kHz PWM generator, gate drive and 10 A continuous / 15 A peak H-bridge amplifier stage. It also has onboard voltage and current sensing with the MAX4172 current sense amplifier, an op-amp and a handful of support components. The board was modified for the ANT prototype to handle source voltages up to 40 V. The board to be used on the ANT prototype is shown in Fig. 3.26 (top and bottom view of the board).

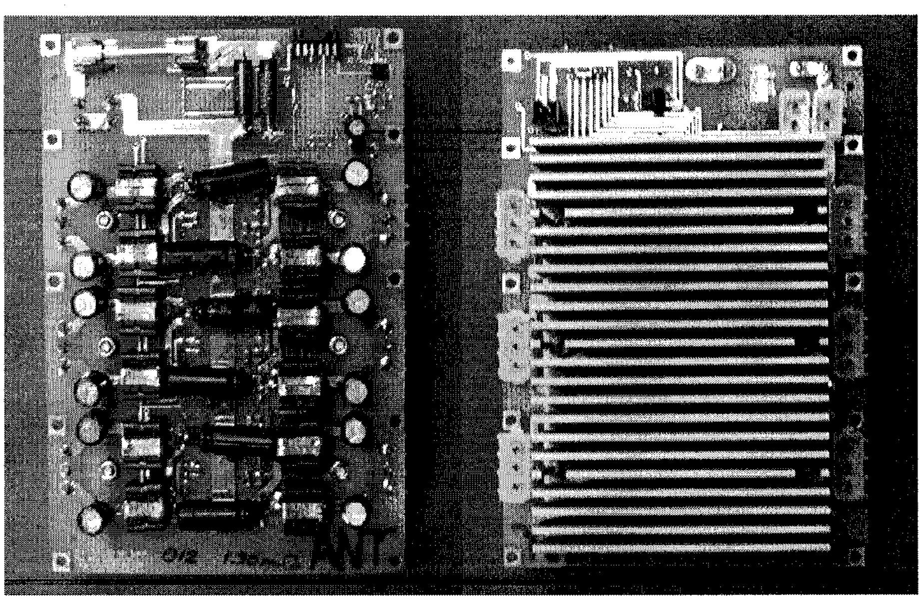

Fig. 3.26. Motor driver board for the wheel motors (top and bottom).

3.3.3. Power Supply

To power the ANT prototype, Nickel-Metal Hydride (NiMH) battery packs were selected. NiMH batteries offer high amperage output with proven reliability. Each pack is composed of 10 *Sanyo Twicell HR-D* cells [62]. These size D cells deliver 1.2 V each, summing to deliver 12 V from each pack with a 7.5 Ah rating. The are able to deliver 80 A continuous and up to 130 A peak. Each pack weighs 1.89 Kg and is protected top and bottom with heat resistant foam (Nomex), then wrapped in two layers of shrink wrap. One 10 cell pack with connector leads is pictured in Fig. 3.27. Three battery packs will be used to give the robot a 36 V supply and yield a total onboard battery mass of 5.67 Kg. For more information on the Sanyo HR-D cells, please refer to the Appendix D for the manufacture's data sheet.

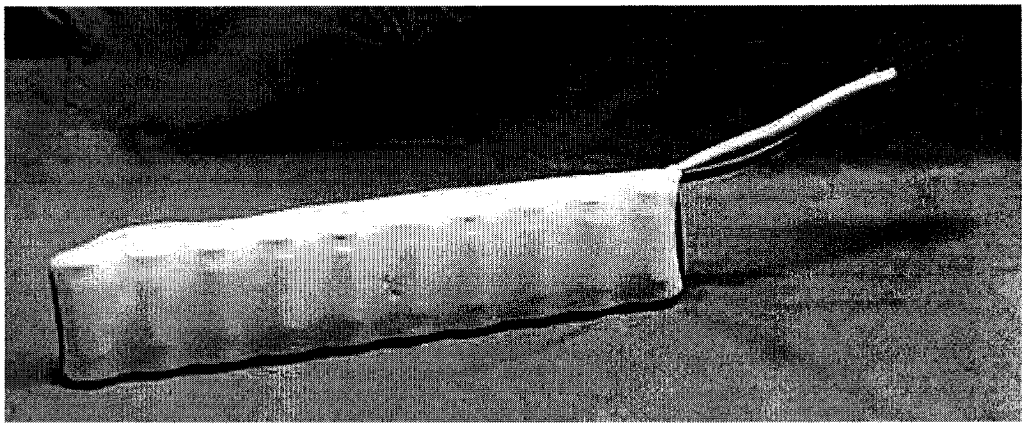

Fig. 3.27. NiMH battery pack for ANT prototype.

3.3.4. Control Electronics

The testbed's motors and sensors will be interfaced with a PC/104 form factor computer consisting of five boards. The *stack* of the five boards to be used on the prototype weighs 695 grams and is pictured in Fig. 3.28. A real-time operating system, *QNX 4.0*, will be used to run a C/C++ compiler, *Watcom*, to generate the controllers. The heart of the computer stack is the *Lippert CoolRoad Runner II* single board computer shown in Fig.

3.29 [47]. It is a PC/104-plus board with a *NSC Geode* Pentium-II-class 300 MHz. processor, fast IDE, 2 USB ports, 2 serial ports, parallel port, keyboard connector, PS/2 mouse port, sound, VGA/CRT and LCD support. It offers low power consumption and has been equipped with 256 MB of SDRAM and a 256 MB Flash disk.

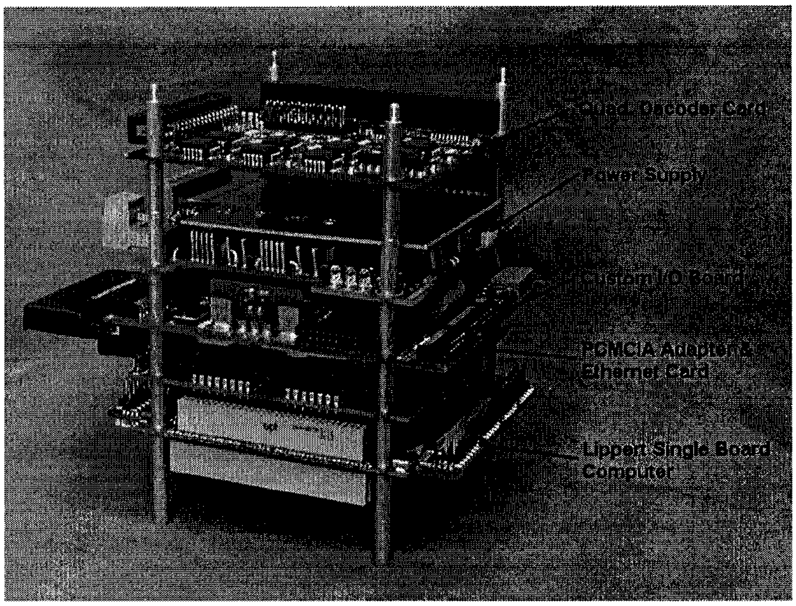

Fig. 3.28. PC/104 form factor computer.

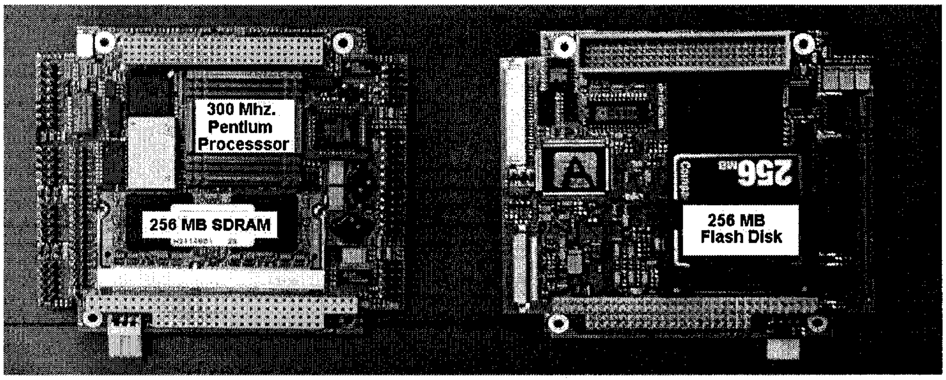

Fig. 3.29. *Lippert CoolRoad Runner II* single board computer (top and bottom).

Wireless Ethernet is provided using the *VersaLogic PCM-3115* PCMCIA adapter with a wireless Ethernet card capable of up to 11 Mbits per second (see Fig. 3.30) [48]. A desktop or laptop PC connected to a wireless access point will act as a user interface, eliminating the need for any cable connections to upload, change or edit controllers.

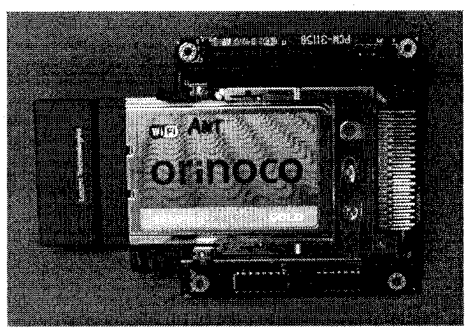

Fig. 3.30. *VersaLogic PCM-3115* PCMCIA adapter with Ethernet card.

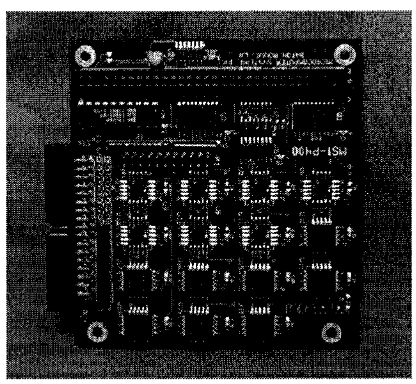

Fig. 3.31. *Microcomputer Systems MSI-P400* Quadrature decoder card (8-channel).

To monitor the position of the motor shaft with the encoders, a multi-channel quadrature decoder/counter card will be used. Each channel on the *Microcomputer Systems MSI-P400* card [50] has a 16-bit binary up/down counter with full 4X decoding and latched count outputs using a *Hewlett-Packard HTC-2016* decoder IC [43]. Thus, the motor's encoders, which have 500 counts per revolution, will be decoded to yield 2000 counts per revolution using the quadrature decoding. The particular card for the prototype, shown in Fig. 3.31, has 8 channels; 4 allocated to the hip motors and 4 to the wheel motors.

The robot's motor drivers and sensors will be interfaced to the computer stack using the custom interface card shown in Fig. 3.32. These particular cards have been used successfully by the Robotic Hexapod (RHex) project at the ARL for a couple of years. The card supports 12 analog outputs with 12 bit resolution; 8 outputs are allocated to the hip amps since they require differential input, and 4 outputs will be allocated to wheel motors since they only require single ended control. The board has 16 analog inputs (10-bit) that will be used for sensors. There are also 16 digital inputs, of which four will be used for Hall Effect sensors to zero the hip positions, while the remaining inputs will normally be connected to DIP switches for configuration settings. The card provides 8 digital outputs so that LEDs can be used for status feedback, as well as eight channels of radio-control servo inputs (PWM) to accept user commands. The A/D conversion performed by the PIC (*Microchip Technology PIC17C766/CL*) on the I/O card limits the iteration time for sensor feedback to a maximum of 1 KHz.

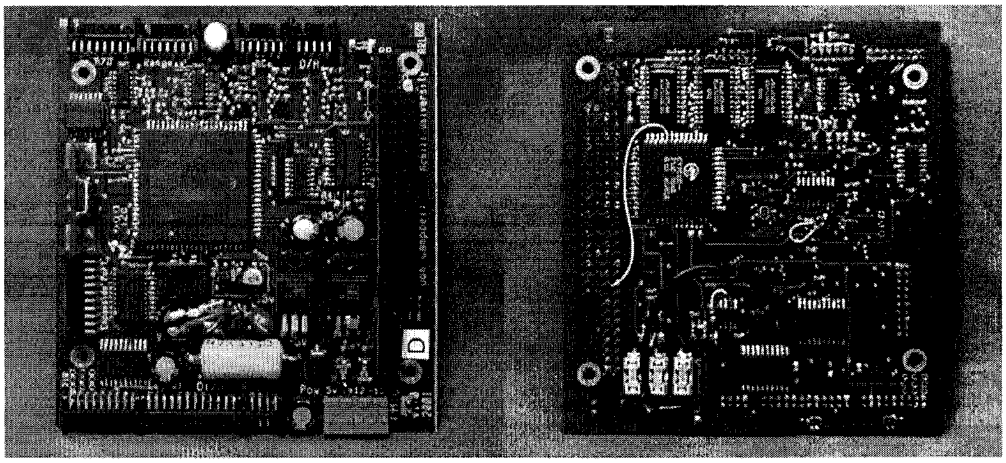

Fig. 3.32. Custom interface card for PC/104 computer.

The computer stack is powered by a *Real Time Devices* 50 W embedded power supply pictured in Fig. 3.33 [49]. The *EPWR104HR-25/25W* is protected against transient and reverse voltages, commonly encountered in vehicle operations, with continuous overload protection on all outputs. The board has two independent power supplies; a 25 W converter powers the +5V of the PC/104 bus and an additional 25 W converter supplies 5V and ±12V for the PC/104 bus and peripherals. The input voltage range is between 8 and 40 V, allowing the computer stack to be powered directly by batteries.

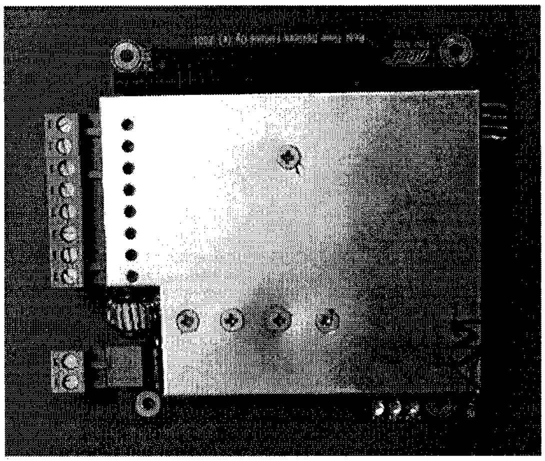

Fig. 3.33. *Real Time Devices* 50W embedded power supply for PC/104.

3.4. Mechanical Design

A full 3D model of the prototype was created in a *SolidWorks* software package [59]. The specifications in Table 3.1 were the general design targets for the prototype. The various actuation, power and control requirements of the platform embodied the majority of the platform's size and mass. Since a low mass is crucial to a dynamic platform, these components were chosen for their small size and mass, but they still allocate the majority of the targeted design mass. It was therefore important to design a very light structure so that the design objectives could be met and the dynamic performance realized. At the same time, the dynamic maneuvers will require the platform's structure to be quite strong since it will experience very high accelerations. For these reasons, the structure is composed mainly of high grade aluminium, owing to its renowned strength to weight ratio.

An important criteria for the design was that the robot's mass be symmetrically distributed about the pitch and roll axes. This was the mass distribution used in simulation and will help to keep the control of the robot as simple as possible. It is quite difficult to do this in practice, but it was decided to design for as much symmetry as possible and then compensate for any unbalance by shifting the batteries slightly.

3.4.1. Springs

Through simulation, it was determined that for the ANT prototype a spring constant around 5000 N/m would be ideal. The upper limit for the spring's stiffness was set to 5500 N/m owing to the speed limitations of the motor (no load speed). The lower limit was set at 4000 N/m to ensure a minimum speed in certain gaits and then raised to 5000 N/m to reduce travel and frictional losses. The mechanisms behind these design tradeoffs were discussed in *Section 2.1.3. Leg Compliance.*

Two sets of extension springs were chosen for the prototype. Extension springs were chosen as they are lighter than equivalently rated compression springs. Two springs operating in parallel were used over a single spring to eliminate any unbalanced spring forces. One set yields a spring constant of 4340 N/m per leg, while the other set yields a constant of 5220 N/m per leg. The reason for choosing 2 sets is that the first few behaviours to be implemented on ANT will not require the stiffer springs due to less stringent travel requirements. These behaviours will be easier to implement with the softer set and will help to familiarize the user more quickly with the inherent dynamics of the platform. When familiarity with the platform is gained and the work progresses, the stiffer set will be used to implement the higher energy maneuvers.

Both sets of springs will be pretensioned by 20 mm and can be extended the entire length of the prototype's 75 mm leg travel. The small table below summarizes the loading characteristics of both sets of springs and is adjacent to a picture containing a spring from both sets.

Table 3.4. Spring properties.

Parameter	Set #1	Set #2
Constant (k)	4340	5220
Preload (20 mm)	87 N	412 N
Max. Load	391 N	495 N
Mass	133 g	272 g

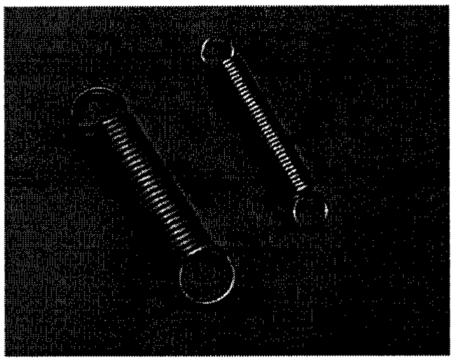

Fig. 3.34. Springs (Left k= 2610 N/m, Right k = 2170 N/m).

3.4.2. Leg Design

It is very important that the leg be as lightweight as possible to ensure low unsprung mass and low rotational inertia. The leg design was also critical to the platform's performance because it houses the compliance, which must be a reliable, low friction mechanism in order to keep the losses down and the return heights high. The leg also houses the wheel that is responsible for enabling the many of the dynamic behaviours. Consideration of all these factors went into the prototype's leg design presented in Fig. 3.35.

The leg is 180 mm in length from the hip axis to the wheel axis, meeting the targeted value given in Table 3.1. The unsprung mass of the leg is 822 g, which is 22% heavier than the targeted 670 g. However, this unanticipated mass increase will not significantly impede the platform's performance. This is because the prototype's body mass increased slightly from the targeted mass of 16.3 Kg to

16.7 Kg, a 2.5% increase. In simulation a body mass of 16.3 Kg was used with the leg mass of 670 g. This caused a 14% loss in the compliance efficiency. The body mass of the prototype is 16.7 Kg and it has a leg mass of 822 g. This will result in a 17% loss in the compliance efficiency. Thus, even with a 22% increase in leg mass, the legs are light enough that the small increase in body mass compensates for this increase, resulting in only a 3% increase in losses from unsprung mass.

Owing to the dynamic loading conditions, linear bearings were used to acquire a stiff, low friction prismatic leg joint. A commercial linear guide, *THK 2 RSR15 VM SS* [51], which has two *THK RSR 15*'s sliders mounted in series on one rail, was selected to carry the loads and maintain the required stiffness (see Fig. 3.36). The *THK LM* size 15 rails can be machined to customize the length, to accommodate mounting and reduce the rail's mass. They also have a low profile that helps keep the width of the platform down.

Fig. 3.35 and Fig. 3.38 show how the linear guide was integrated into the leg design. Because the slider rail is relatively heavy, it was attached to the hip shaft while the slider blocks were attached to the leg to keep the unsprung mass down. The wheel and springs were mounted along the slider's line of action so that the momentum transfer from the body to the springs would be as direct as possible. As mentioned, the two springs were mounted on either side of the slider to minimize any unbalanced forces on the sliders, thereby keeping the sliding resistance as low as possible. The slider blocks are bolted to the one piece leg struts on which the springs, wheel and motor are mounted. The springs are held in place using eye bolts to allow for adjustments in pretension or to accommodate different spring sets.

To minimize losses, the wheel's transmission was kept as direct as possible. One of the bevel gears is bolted directly onto the hub of the wheel and the other gear uses a set screw that sinks into a hole on the gearhead's shaft (see Fig. 3.39). These bevel gears must mate precisely for efficient power transmission, which requires both the wheel and the motor to be mounted rigidly so that there is next to no movement between them. For this reason, the brace that fixes the wheel to the leg also mounts the motor on the leg. Not only does the conglomeration of the separate fixtures result in higher rigidity, but both gears will move together in the event of any deflection reducing the opportunity for misalignment. This mount braces the wheel from both sides to minimize the stresses developed in the wheel shaft, the bearings and the mount itself.

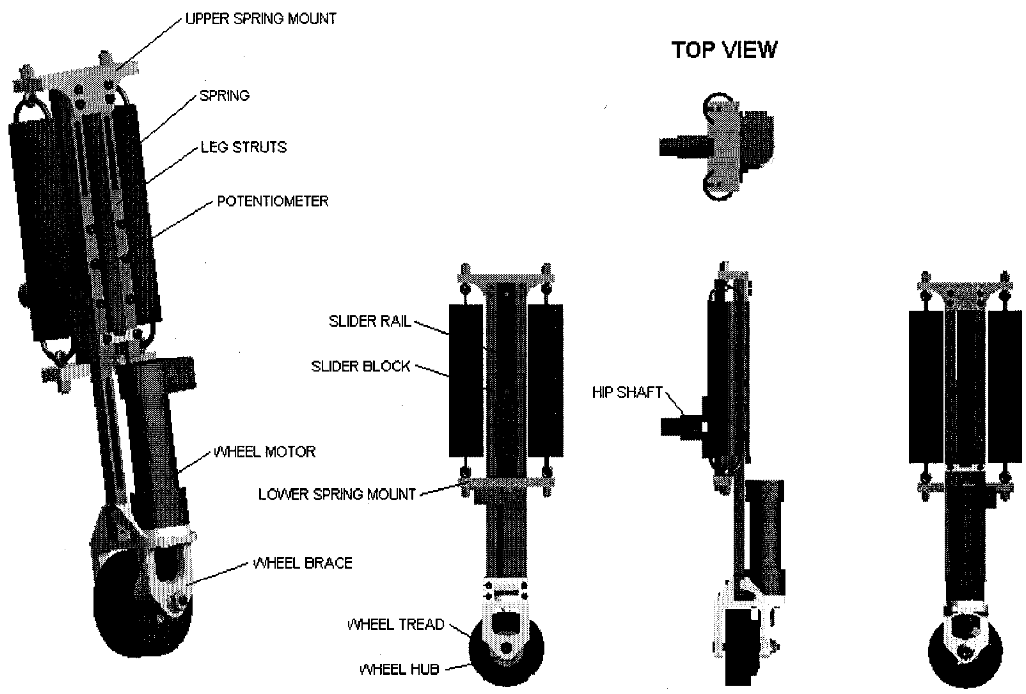

Fig. 3.35. Leg design for prototype.

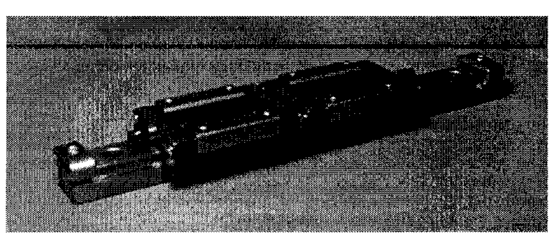

Fig. 3.36. *THK 2 RSR15 VM SS* slider blocks on sample *THK 150 LM* rail.

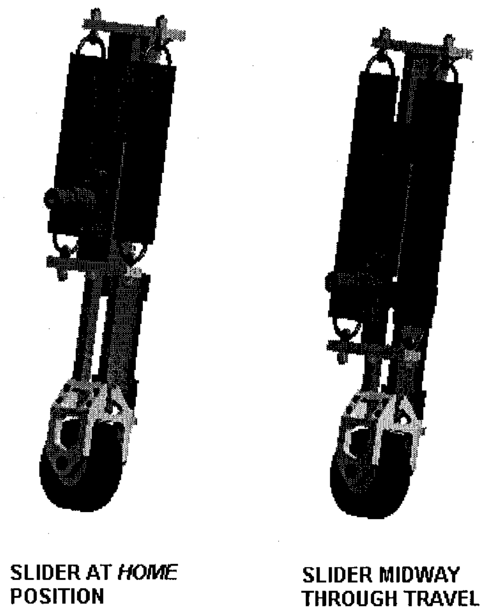

Fig. 3.37. View of leg design depicting leg travel.

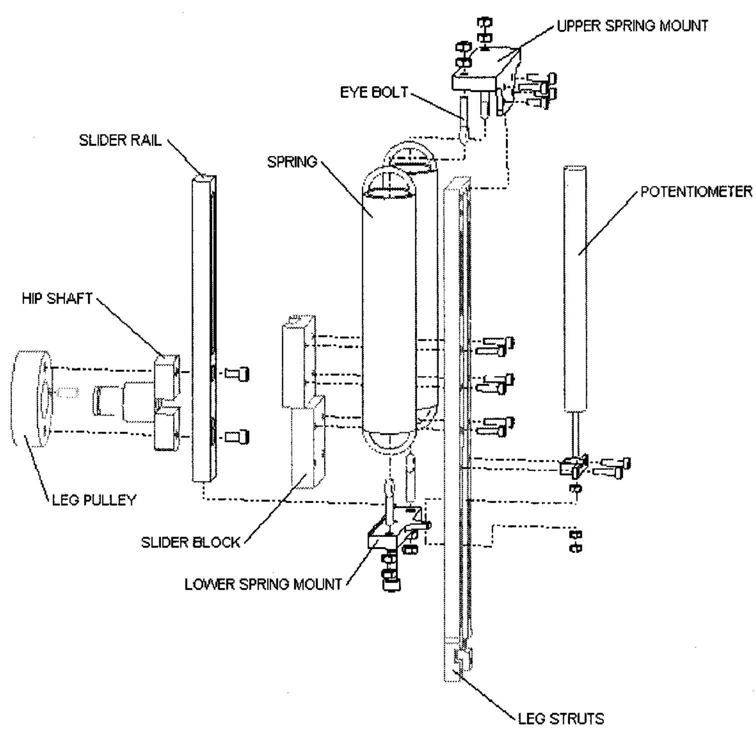

Fig. 3.38. Upper leg assembly.

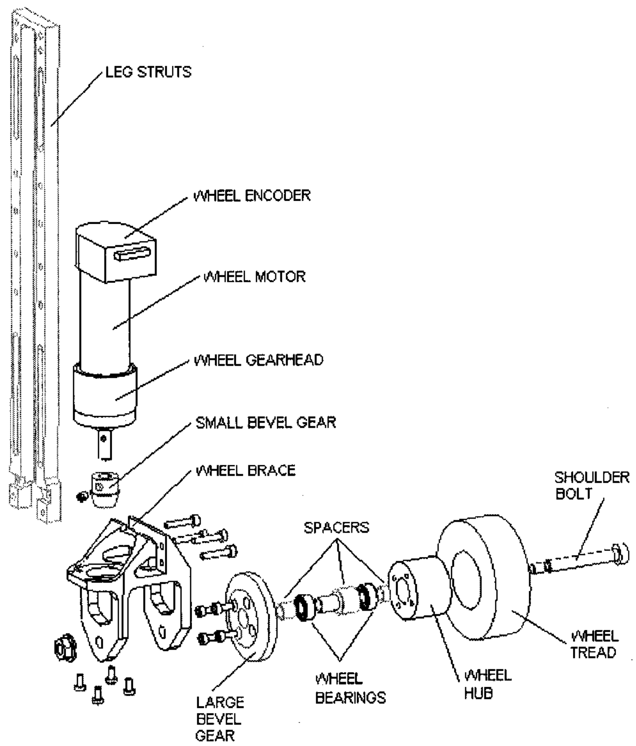

Fig. 3.39. Lower leg assembly.

The wheel hub's small diameter and large width necessitated the use of two bearings (*NSK 686DD*) [56] to properly handle the loads put on the wheel (see Fig. 3.39). The rubber wheel tread that is placed over the hub gives the wheel its traction and is crucial in dissipating the momentum of the lower leg during touchdown. The importance of the latter can be deduced from considering the case where the leg touches down and the momentum of the unsprung leg mass is not dissipated. Here the leg will bounce back and off the ground repeatedly producing what is known as *chatter* [40]. However, the controller commands the same leg torques/trajectories regardless if there is chatter present or not, which causes unpredictable behaviour to develop. This source of error is eliminated on the ANT prototype with the thick layer of rubber around the wheel hub that dissipates the leg's momentum and keeps the wheel in contact with the ground throughout stance. The exact type of rubber will be determined experimentally on the prototype to ensure proper performance.

In order to determine the position of the compliance with the potentiometer, its outside cylinder is attached to the leg and its sliding rod is bolted to the lower spring mount (see Fig. 3.38). The potentiometer was placed between the leg struts to protect it from damage as seen in the isometric view of Fig. 3.36.

3.4.3. Hip Design

A large part of the hip's layout was predetermined by the selection of transmission, as discussed in *Section 3.2.1. Hip Actuation*. Many of the remaining issues were brought to light by observing the frequent failures of similar components on other robotic platforms in the ARL. The hip design is pictured in Fig. 3.40 and Fig. 3.41. Similar to the directive for the wheel's bevel gears, it was important that the pulleys' fixture to their appropriate shafts be very robust. So the pulley on the leg is bolted directly to the hip shaft and the other pulley is fixed to the gearhead's shaft with a steel key and a set screw (see Fig. 3.41).

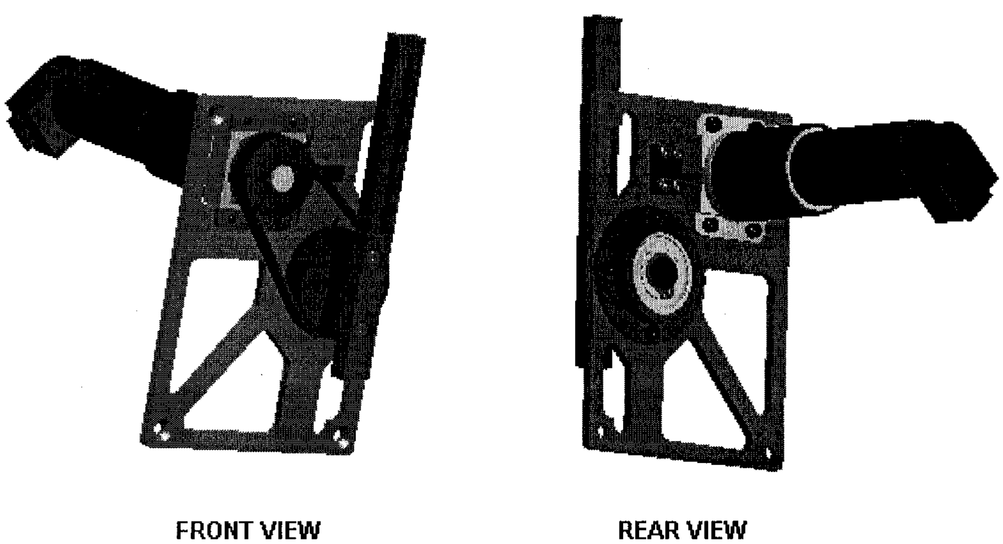

Fig. 3.40. Hip Design for ANT prototype.

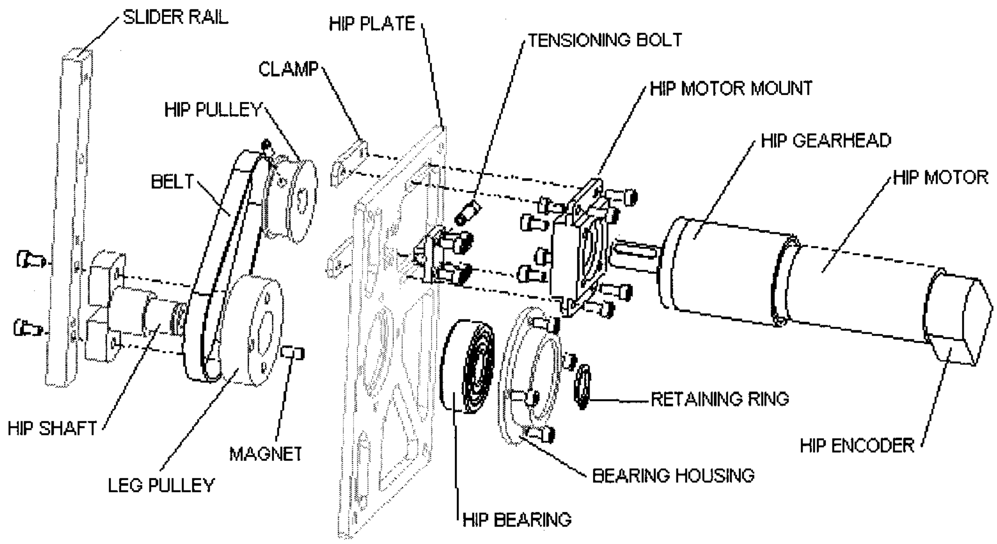

Fig. 3.41. Hip assembly.

To allow for quick assembly and to enable proper tensioning of the belt, the hip houses a tensioning system. The motor's gearhead is bolted to the hip's motor mount, which is in turn fixed to the hip plate by a clamping force - generated between the motor mount and the two clamping plates on the opposite side of the hip plate. When the clamps are loosened slightly, the motor mount can slide back and forth along a slot in the hip plate as shown in Fig. 3.42. A tensioning bolt aligned with this slot enables proper tensioning. To adjust the belt, the clamps are loosened, the tensioning bolt is used to adjust the position and then the clamps are retightened. It should be noted that the tensioning bolt is not meant to hold the motor mount in the desired position, but serves only to ease assembly and ensure sufficient belt tension. The clamping force is more than sufficient to hold the motor mount in place and is a well proven technique used on other platforms in the ARL.

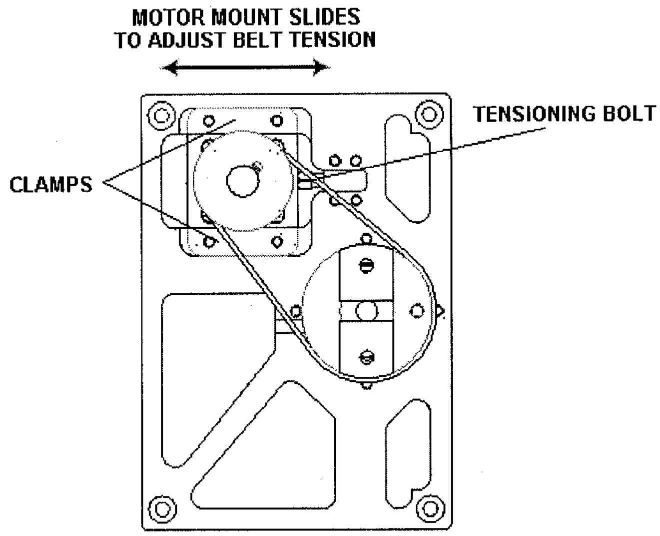

Fig. 3.42. Tensioning the hip belt

The hip shaft is mounted to the body through a bearing housed in the hip plate. The *SKF 6302-2RS1* [57] bearing may at first glance seem quite large for use on the ANT prototype, but it must handle the large moments generated by the distance that the linear slider is offset from the hip plate. This large bearing also accommodates a large hip shaft, which is bored out to permit cabling to pass through. Since the wheel motor, its encoder and the potentiometer require continuous connection to the electronics located inside the body, the hole through the hip shaft (labelled in Fig. 3.43) is used to feed wires from the leg into the body. Currently, this limits the rotation of the hip to only a few turns in either direction before it would damage the wires. This is sufficient to demonstrate the dynamic behaviours presented in this report, but it will be desirable in the near future to add slip rings inside the body to facilitate continuous rotation in either direction. It will be an easy upgrade to the testbed owing to the empty space along the entire axes of the hips and this cabling hole.

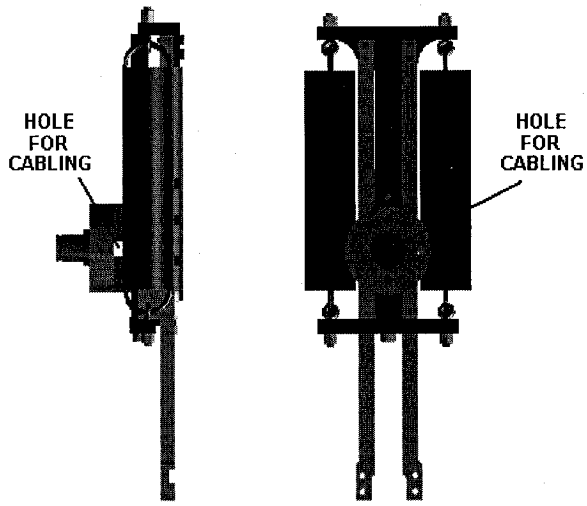

Fig. 3.43. Hole in hip shaft to allow wiring.

For ease of assembly and to reduce downtime caused by maintenance or inspection, the entire leg assembly is held in place by a retaining ring. All that is required to remove the leg from the hip is to loosen the hip belt and remove the retaining ring as shown in Fig. 3.44.

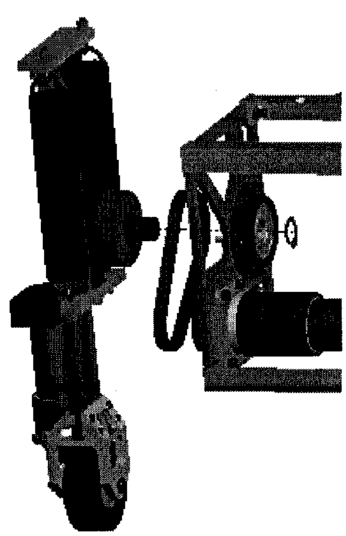

Fig. 3.44. Assembly of the leg to the hip.

3.4.3. Body Design

The four identical hips are structurally joined by six braces forming the frame assembly shown in the left side of Fig. 3.45. The hip plates and frame braces are composed of 7075-T6 aluminium owing to its high strength to weight ratio. On the right side of Fig. 3.45, the electric hardware is shown mounted to body. A detailed assembly of the electrical mounting is included in Appendix B. The batteries are held to rubber-surfaced braces (see Fig. 3.46) using Velcro straps to accommodate easy mounting/dismounting for recharging. Their fore-aft position can be adjusted to ensure an even distribution of mass about the pitch axis and will be determined experimentally on the assembled prototype. Note that the mass distribution about the roll axis is already symmetrical. Padding will be temporarily attached to the frame during the troubleshooting of the controllers to protect it from the abuse during this testing phase. A 1/32" Lexan skin, held on with Velcro, will also be used to help protect the electronics in the body from foreign objects (see Fig. 3.47).

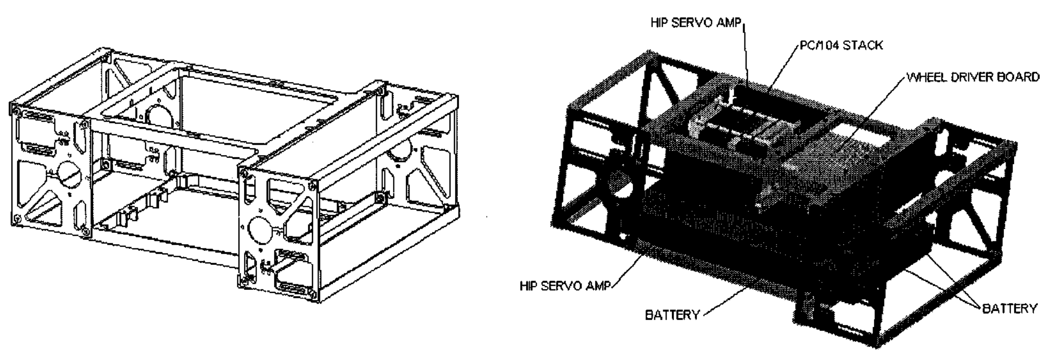

Fig. 3.45. Frame design for ANT prototype – structural (left) and stuffed (right).

The entire ANT prototype assembly is pictured in Fig. 3.46. The total mass of the prototype is 18.8 Kg without the inclusion of any wiring. It is estimated that the platform will be brought to a total mass of approximately 20 Kg with the cabling and their harnesses. This is an acceptable 1 Kg, or a mere 5%, over the targeted total mass. As mentioned earlier, the unsprung leg mass, which embodies the components considered to be the leg, is 822g. This is 152 g heavier than the targeted leg mass, but as previously discussed, the losses from unsprung mass only increased by 3% owing to the slight increase in body mass.

Generally speaking, the design targets outlined in Table 3.1 were amply met. The width of the body is a little larger than anticipated owing to the large leg width, but this has no effect on the platform's ability to achieve the dynamic behaviours discussed in this report. Notable differences in the design specifications are a 6 mm decrease in body length, an 8 mm increase in body thickness and a 4 mm decrease in ground clearance.

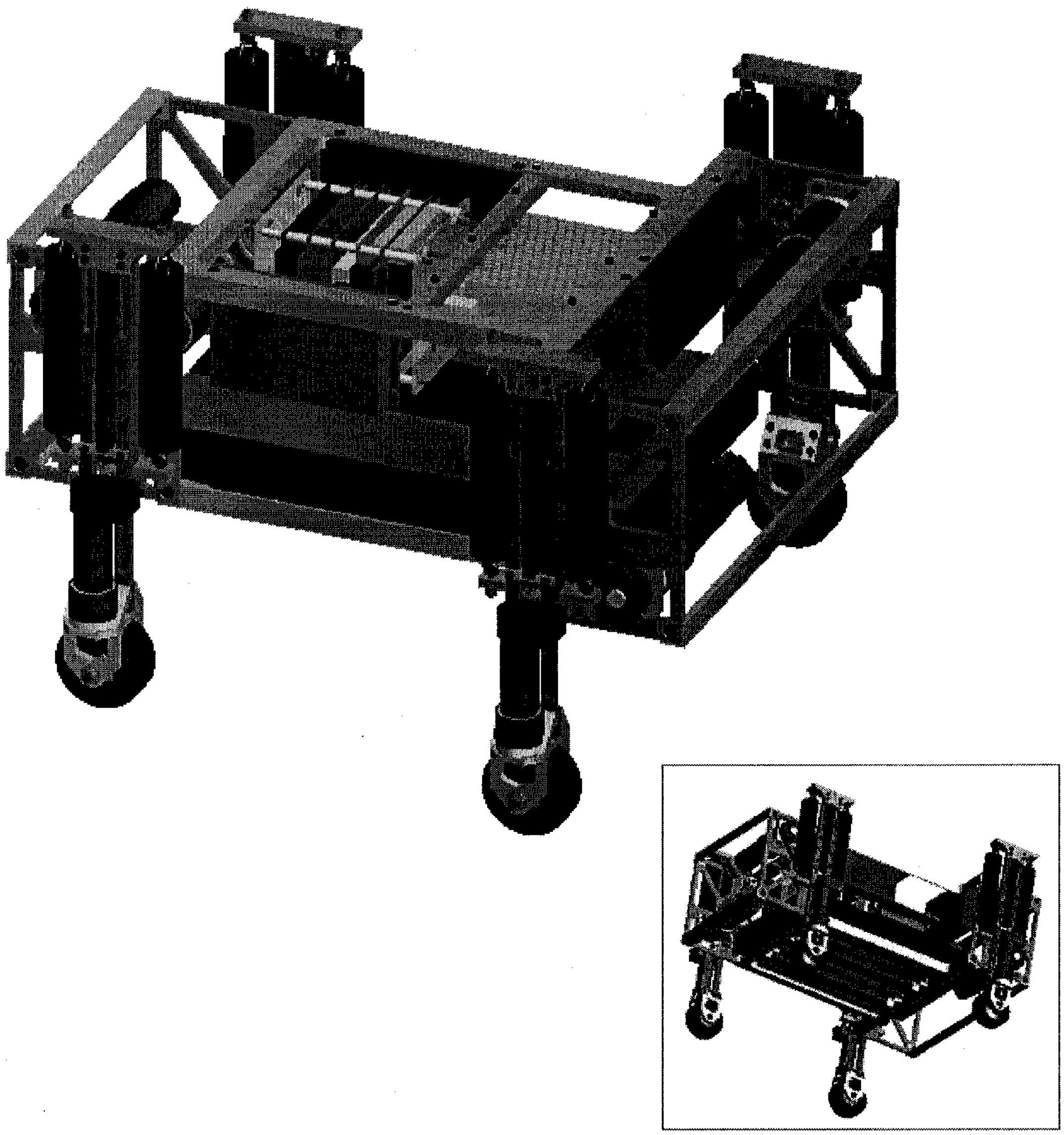

Fig. 3.46. Full Assembly of the ANT prototype.

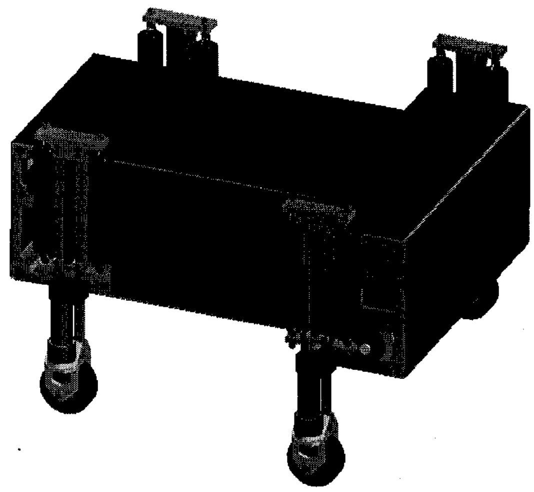

Fig. 3.47. ANT prototype with protective skin.

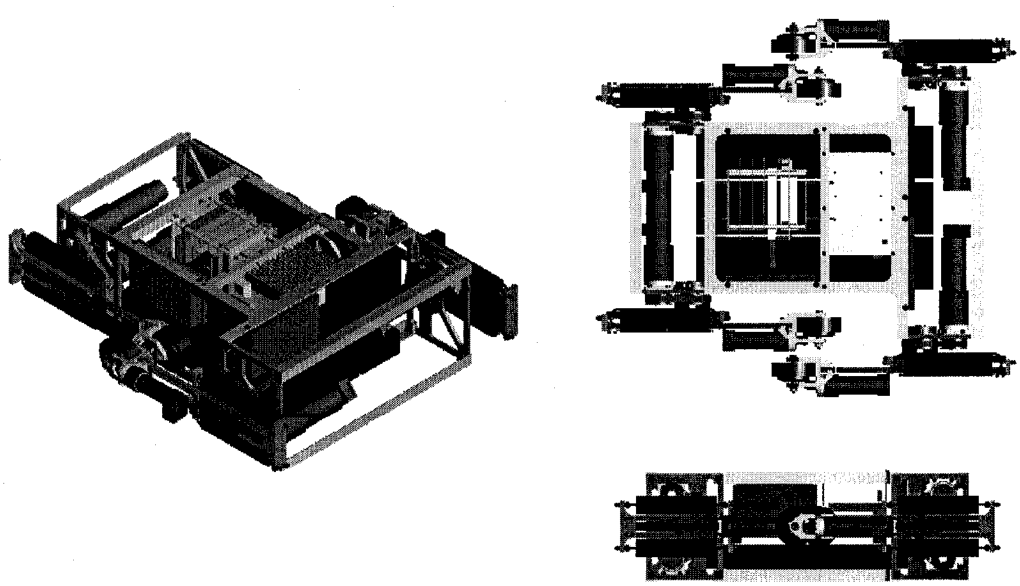

Fig. 3.48. ANT prototype with the legs folded.

3.5. Project Status

Machine drawings for the entire prototype were done using the *SolidWorks* software package [59], which included dimensions, tolerances and all machinist instructions. These drawings were sent to a few machine shops, whose quotes ranged from $5,000 to $8,000 (CAN, without taxes). All the of electrical and mechanical hardware has been purchased, as well as the raw material to be used for machining. The amplifiers have been calibrated and basic controller libraries from another ARL robot has been successfully uploaded to the PC/104 stack via the wireless ethernet. To date, the amount spent on the prototype's components, without the inclusion of duty, delivery or brokerage fees, is approximately $20,500 CAN. For a complete bill of materials and a full cost breakdown of the prototype, please refer to Appendix C.

Chapter 4

Conclusion

Using a detailed model, a variety of dynamic behaviours were successfully simulated for a hybrid leg-wheel platform. The realization of these behaviours is largely owed to the exploitation of the passive leg compliance. It efficiently recycles otherwise dissipated energy and enables these highly energetic maneuvers to be executed on this power autonomous platform. The placement of active wheels at the foot of the legs proved to significantly widen the scope of feasible dynamic behaviour for a quadruped platform. This degree of freedom, which was previously only exploited for rolling or ground following, reduces the torque requirements at the hips and facilitates a variety of otherwise impossible dynamic behaviour. A number of these maneuvers hold great utility for obstacle negotiation, enabling the platform to outperform larger robots without these arsenals. Most notable is the back flip that allows the robot to overcome obstacles greater in height than the platform itself.

These seemingly complex feats of mobility were accomplished with relatively simple controllers. The need for complicated control algorithms was primarily negated by maintaining a simple mechanical layout. From the standpoint of legged robots, this platform has a substantial reduction in both the number and the complexity of its degrees of freedom. A typical legged robot will have 3 or 4 active DOF per leg. The ANT platform on the other hand has only 2 active DOF and one passive DOF. This lends the ANT platform to simpler control methods and a much more robust leg design than other legged platforms. The simple layout of the leg lends itself to quicker movement than other more complex leg designs, which are weighed down by their actuators and are prone to frequent breakdowns. This reliability, coupled with its power autonomy, will allow the platform to be easily adopted for *real world* operation.

A full systems design of a testbed capable of executing the dynamic behvaiours presented in *Chapter 2* was completed. Owing to the use of a realistic model in simulation, the design specifications were able to be met. As targeted, the testbed is completely power and computationally autonomous. Many of the lessons learned from other robots in the ARL were considered in the testbed's design, which has undoubtedly produced a very robust and reliable machine. This prototype will prove the feasibility of the presented behaviours for autonomously powered platforms, demonstrate their wide utility and pave the way for their realization on ruggedized platforms.

Future Work

The focus of any work in the immediate future will undoubtedly be the construction of the prototype and the implementation of the developed controllers. This involves commissioning the machining, fully assembling the robot including all the wiring/cabling and troubleshooting the controllers. Once the behaviours from this study are successfully implemented, it seems to follow naturally that other behaviours and utilities will be investigated. Payload and endurance studies may be undertaken to access the performance of the platform for *real world* tasks. Behaviourally, there is a great deal of unexplored opportunity in manoeuvring about the roll and yaw axes. The development of a reliable stair climbing algorithm would obviously be beneficial as well. Another behavioural example is a bi-pedal gait, whereby the robot would hop along the ground on just two legs. To attain stability, it may require much more sophisticated control algorithms than the control presented in this work, but it is predicted that the active wheels will significantly aid in the control of such a gait.

A few statically stable behaviours have been developed for the platform, such as a traction controller, a body pitch controller and a number of open loop walking gaits. These will also be implemented on the testbed, with focus on implementing open loop gaits like the crawl to efficiently negotiate obstacles and rough terrain. Since this robot is under the umbrella of DRES's ANT project, it may be desired in the future to design and construct another module to investigate six-legged behaviour.

An easy and most useful upgrade to the prototype is the addition of slip rings to facilitate the continuous rotation of the hip. As discussed in *Chapter 3*, this upgrade was anticipated so the prototype was designed to accommodate this add-on. Upgrades could also be made to allow for outdoor testing, which would aid in the development of a ruggedized version of the platform. A much larger upgrade that could be considered further in the future is the possibility of converting the legs into *tracked paddles*, as depicted in Fig. 4.1. It would involve the attachment of an idler on the leg and a belt that would run around it and an upgraded wheel. If the design manages to be of light enough weight that the dynamic behaviour is not significantly inhibited, then it would tremendously expand the stair climbing and rough terrain negotiating capabilities of the platform.

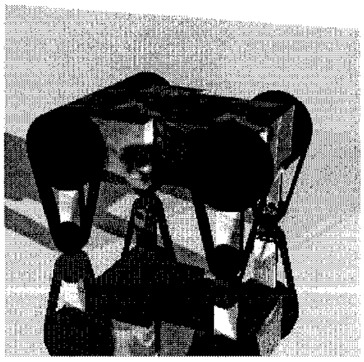

Fig. 4.1. ANT platform with *tracked paddles* as legs.

Bibliography

[1] A. Bogatchev, V. Gromov, V. Koutcherenko, S. Matrosso, V. Petriga., V. Solomnikov and S. Fedoseev, "Walking and wheel-walking robots", in Proc. 3rd Int. Conference on Climbing and Walking Robots, Madrid, Spain, 2000, pp. 813-823.

[2] "Preliminary concept of the autonomous chassis of the polar rover, Science report, S & T Rover Co. Ltd. (RCL), St. Petersburg, Russia, 1995.

[3] Web Ref. (Rovers): www.img.arc.nasa.gov/Marsokhod/missions.html

[4] Y. Ichikawa, N. Ozaki, Sadakane K., "A hybrid locomotion vehicle for nuclear power plants", IEEE Trans. On Systems, Man & Cybernetics SMC-13(6), pp. 1089-1093, 1983.

[5] T. Oomichi and T. Ibe, "Development of leg-wheel typed mobile", Robotics Society of Japan, vol. 2, no. 3, pp. 68-75, 1984.

[6] G. Belforte, N. D'Alfio, C. Ferraresi and M. Sorli, "Mobile robot with wheels and legs", in Proc. Int. Symposium and Exposition on Robots, 19th ISIR by the International Federation of Robotics, IFS Publications, 1988, pp.610-622.

[7] N. Kimura, "Disaster-preventing robot at petroleum production facilities", in Proc. 5th Int. Conf. on Advanced Robotics (ICAR), 1991, vol. 1, pp. 309-314.

[8] G. Endo and S. Hirose, "Study on roller-walker (system integration and basic experiments)", in Proc. IEEE Int. Conf. on Robotics and Automation, 1999, pp. 2032 -2037.

[9] H. Adachi, N. Koyachi, T. Arai, A. Shimiza and Y. Nogami, "Mechanism and control of a leg-wheel hybrid mobile robot", in Proc. IEEE/RSJ Int. Conf. on Intelligent Robots and Systems, 1999, pp. 1792 –1797.

[10] C. Brosinsky, D. Hanna, S. Penzes, "Articulated navigation testbed (ANT): an example of intrinsic mobility", in Proc. of the SPIE 14th Annual International symposium on Aerospace/Defence Sensing, Simulation and Controls, Orlando, Florida (2000).

[11] C. Brosinsky, S. Penzes, M. Buehler and C. Steeves, "Integrating intrinsic mobility into unmanned ground vehicle systems", in Proc. of the SPIE 14th Annual International symposium on Aerospace/Defence Sensing, Simulation and Controls, Orlando, Florida (2001).

[12] A. Halme, K. Koskinen, V-P Aarnio, I. Leppänen, S. Salmi and S. Ylönen, " WorkPartner – Future Interactive Service Robot", STeP2000 Millennium of Artificial Intelligence Conference, Helsinki, Finland, Aug 2000.

[13] F. Benamar, Ph. Bidaud, F. Plumet, G. Andrade and V. Budanov, "A high mobility redundantly actuated mini-rover for adaptation to terrain characteristics, in Proc. 3rd Int. Conf. on Climbing and Walking Robots, Madrid, Spain, 2000, pp. 105-112.

[14] Swiss Federal Institute of Technology Lausanne, Autonomous Systems Lab, dmtwww.epfl.ch/isr/asl/systems/shrimp.html

[15] O. Matsumoto, S. Kajita, K. Tani and M. Oooto, "A four-wheeled robot to pass over steps by changing running control modes", in Proc. 1995 IEEE International Conf. on Robotics and Automation, 1995, vol. 2, pp. 1700 – 1706.

[16] Raibert M. H., Brown Jr. H. B., Chepponis M., Hodgins J., Kroechling J., Miller J., Murphy K., N., Murthy S. S. and Stentz A., "Dynamically Stable Legged Locomotion", *Technical Report, CMU-LL-4-1985*, Carnegie Mellon University, The Robotics Institute, Pittsburgh, PA, USA, February 1985.

[17] Raibert M. H., Chepponis M., Brown H. B. Jr. "Running on four legs as though they were one". *IEEE J. Robotics and Automation*, 2:70-82, 1986.

[18] Massachusetts Institute of Technology, Leg Laboratory, www.ai.mit.edu/projects/leglab.

[19] University of Electro-Telecommunications, Dept. of Information Management Science, Kimura Lab, www.kimura.is.uec.ac.jp/kimlab-e.html.

[20] Pearson K., "The Control of Walking", *Scientific American*, Vol. 72, p. 86, 1976.

[21] Buehler M., "Dynamic Locomotion with One, Four and Six-Legged Robots", in *J. of the Robotics Society of Japan*, Vol. 20, No. 3, pp. 15-20, 2002.

[22] Ahmadi M., *Stable Control of a One-Legged Robot Exploiting Passive Dynamics*, Ph.D. Thesis, McGill University, Montreal, QC, Canada, May 1998.

[23] Ahmadi M. and Buehler M., "Stable Control of a Simulated One-Legged Running Robot with Hip and Leg Compliance", in *IEEE Tr. On Robotics and Automation*, Vol. 13, No. 1, pp. 96 – 104, 1997.

[24] Buehler M., Cocosco A., Yamazaki K. and Battaglia R., "Stable open Loop Walking in Quadruped Robots with Stick Legs", *Proc. of the IEEE Int. Conf on Robotics and Automation*, pp. 2348 – 2353, 1999.

[25] Buehler M., Battaglia R., Cocosco A., Hawker G., Sarkis J. and Yamazaki K., "Scout: A Simple Quadruped that Walks, Climbs and Runs", *Proc. of the IEEE Int. Conf on Robotics and Automation*, pp. 1707 – 1712, 1998.

[26] Battaglia R., *Design of the Scout II Quadruped with Preliminary Stair Climbing*, M. Eng. Thesis, McGill University, Montreal, QC, Canada, May 1999.

[27] Talebi S., Poulakakis I., Papadopoulos E. and Buehler M., "Quadruped Robot Running with a Bounding Gait", *Experimental Robotics VII*, in Lecture Notes in Control and Information Sciences 271, D. Rus and S. Singh (eds.), Springer-Verlag, pp. 281-289, 2001.

[28] De Lasa M., *Dynamic Compliant Walking of the Scout II Quadruped*, M. Eng. Thesis, McGill University, Montreal, QC, Canada, July 2000.

[29] De Lasa M. and Buehler M., "Dynamic Compliant Walking", *Proc of IEEE Int. Conf. on Robotics and Automation*, pp 3153-3158, 2001.

[30] Hawker G., *Quadruped Trotting with Passive Knees: Design, Control and Experiments*, M. Eng Thesis, McGill University, Montreal, QC, Canada, November 1999.

[31] Saranli U., Buehler M., and Koditschek D. E., "RHex: A Simple and Highly Mobile Hexapod Robot", in *The Int. J. Robotics Research*, Vol. 20, No. 7, pp. 616-631, 2001.

[32] Altendorfer R., Moore N., Komsuoglu H., Buehler M., Brown Jr. H. B., McMordie D, Saranli U., Full R., Koditschek D. E., "RHex: A Biologically Inspired Hexapod Runner," in *Autonomous Robots*, Vol. 11, pp. 207-213, 2001.

[33] McMordie D. and Buehler M., "Towards Pronking with a Hexapod Robot", *4th Int. Conf. on Climbing and Walking Robots*, pp. 659 - 666, 2001.

[34] E. Z. Moore, D. Campbell, F. Grimminger, and M. Buehler, " Reliable Stair Climbing in the Simple Hexapod 'RHex'," 2002 IEEE Int. Conf. on Robotics and Automation (ICRA), Vol. 3, pp 2222-2227, Washington, D.C., U.S.A., May 11-15, 2002

[35] MSC Visual Nastran Desktop 2001 (Visual Nastran 4D), 2 MacArthur Place, Santa Ana, CA, 92707, www.mscsoftware.com

[36] Working Model 2D 5.0.3.37 Professional, Knowledge Revolution, 66 Bovet Road, Suit 200, San Mateo, CA 94402, www.krev.com

[37] DRES Contract # W7702-0-R815, "Hybrid Locomotive Unmanned Mobile Platforms", Sept 2000 through Aug 2002.

[38] Farley, C.T., Glasheen, J., and McMahon, T.A., "Running Springs: Speed and Animal Size", Journal of Experimental Biology, 185, pp. 71-86, 1993.

[39] Schmiedeler J., Waldron K., "Leg Stiffness and articulated leg design for dynamic locomotion", *Proc. of ASME 2002 Design Engineering Technical Conferences and Computers and Information in Engineering Conference*, Montreal, Canada, 2002.

[40] Alexander R. McN., "Three uses for springs in legged locomotion", in *The Int. J. Robotics Research*, Vol. 9, No. 2, pp. 53-61, April 1990.

[41] Wolfram Research. *Mathematica*, Version 3.0, 1996, www.wolfram.com.

[42] C. Steeves, M. Buehler, S.G. Penzes, "Dynamic behaviours for a hybrid leg-wheel mobile platform", in Proc. of the SPIE 15th Annual International symposium on Aerospace/Defence Sensing, Simulation and Controls, Vol. 4715, pp. 75-86, 2002.

[43] Hewlett Packard, 2002, www.hp.com.

[44] Stock Drive Products, New Hyde Park, NY, Catalogue No. 780, 2002, www.sdp-si.com.

[45] Digi-key, Catalogue No. C023, 2002, www.digikey.com.

[46] Midori America Corporation, 2555 E. Chapman Ave. Ste. 400, Fullerton, CA 92831, 2002, www.midoriamerica.com.

[47] EMJ Embedded Systems, 220 Chatham Business Drive, Pittsboro, NC, 27312, 2002, www.emjembedded.com.

[48] VersaLogic Corp., 3888 Stewart Rd., Eugene, OR, 97402, 2002, www.versalogic.com.

[49] Real Time Devices USA, Inc., 103 Innovation Blvd., P.O. Box 906, State College, PA, 16804, 2002, www.rtdusa.com.

[50] Microcomputer Systems, Inc., 1814 Ryder Drive, Baton Rouge, LA, 70808, 2002, www.microcomputersystems.com.

[51] THK Canada, 130 Matheson East, Unit 1, Mississauga, ON., L4Z 1Y6, 2002, www.thk.com.

[52] Micronas, Sharad Rastogi Associates, 210 Granville Lane, North Andover, MA, 01845, 2002, www.micronas.com.

[53] Advanced Motion Controls, Camarillo Ca., 2002, www.a-m-c.com.

[54] Apex Mircotechnology, 5980 N. Shannon Road, Tucson, AZ, 85741-5230, 2002, www.apexmicrotech.com.

[55] Murata Electronics North America Inc., 2200 Lake Park Drive, Smyrna, GA, USA, 30080-7604, 2002, www.murata.com.

[56] NSK Canada Inc., 5585 McAdam Road, Mississauga, ON., L4Z 1N4, 2002, www.tec.nsk.com.

[57] SKF Canada Ltd., 40 Executive Court, Scarborough, ON., M1S 4N, 2002, www.skf.com.

[58] Ambulatory Robotics Lab, Center for Intelligent Machines, McGill University, 2002, www.cim.mmcgill.ca/~arlweb.

[59] SolidWorks 2001 Plus, 300 Baker Avenue, Concord, MA, 01742, 2002, www.solidworks.com.

[60] Maxon Motors Inc., 101 Waldron Rd., Fall River, MA., 02720, 2002, www.maxonmotor.com.

[61] McMordie, D., *Towards pronking with a robotic hexapod*, M.Eng. Thesis, McGill University, Montreal, QC, Canada, July 2002.

[62] Sanyo, 2002, www.sanyo.com.

Appendix A

Dynamic Model

The Lagrangian methodology was used, in conjunction with a mathematics software package (*Mathematica*), to develop the equations of motion. The overlying assumption made was that the masses of the legs and wheels were considered negligible. The preliminary step was to breakdown the behaviour of the robot into distinct phases. Phases of this type are selected based on their ability to define the largest set of dynamic behaviours and thus encompass all behaviours with the smallest conceivable set. For ANT, the minimal set is four (4) phases, defined as:

A. Flight phase

B. Rear leg stance phase

C. Front leg stance phase

D. Double leg stance phase.

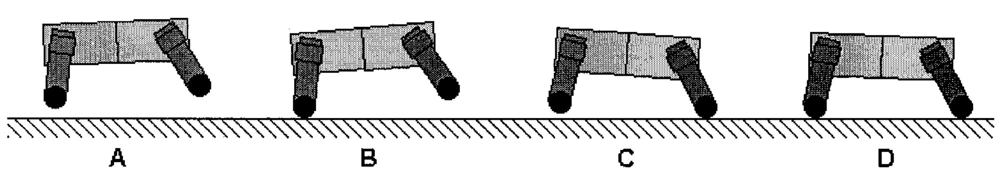

Fig. A.1. Four phases of ANT behaviour.

It is of course assumed that the wheels remain in rolling contact with the ground throughout the appropriate phase.

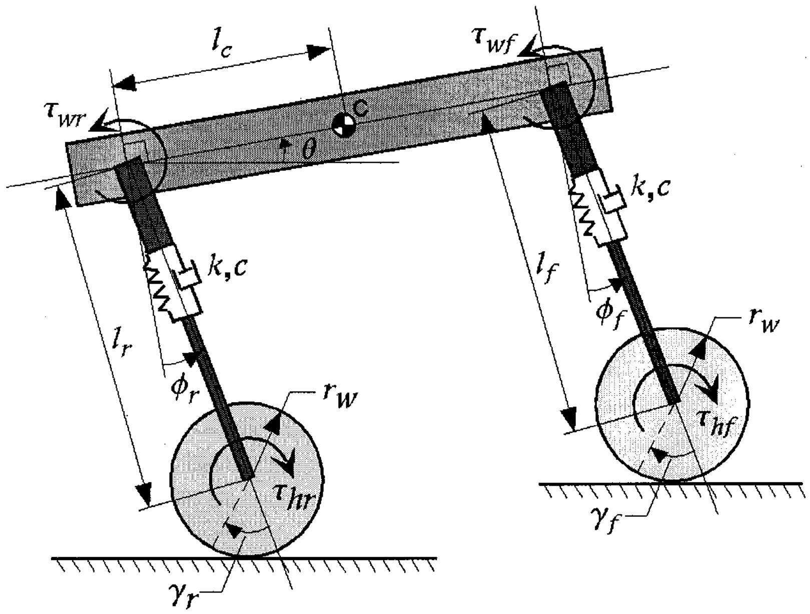

Fig. A.2. Symbolic reference and sign conventions.

A.1. Flight Phase

For the flight phase, the kinetic (T) and potential (V) energiesy are respectively defined as

$$
\begin{aligned}
T &= \tfrac{1}{2}m\dot{x}_c^2 + \tfrac{1}{2}m\dot{y}_c^2 + \tfrac{1}{2}I\dot{\theta}_c^2 \\
V &= mgy_c .
\end{aligned}
\tag{A.1}
$$

Note that the origin is with respect to an inertial frame of reference. Lagrange's equations for such a system are

$$
\begin{aligned}
&L = T - V \\
&\frac{d}{dt}\left(\frac{\partial L}{\partial \dot{q}_j}\right) - \frac{\partial L}{\partial q_j} = Q_j ,
\end{aligned}
\tag{A.2}
$$

where L contains the potential of the conservative forces and q_j contains the states of the system. Components of the *generalized force*, or the forces *not* arising from a potential (i.e. actuation and frictional forces), are represented by Q_j expressed as,

$$Q_j = \frac{\partial W}{\partial q_j}, \tag{A.3}$$

where ∂W is a differential of work. The means by which these generalized forces are incorporated into the Lagrangian methodology are through the following definitions of differential work:

$$\begin{aligned} \partial W_{force} &= \sum_i F_i dl_i \\ \partial W_{torque} &= \sum_i \tau_i d\theta_i \\ \partial W_{friction} &= \sum_i F_{f\,i} dl = \sum_i (c\dot{l}_i) dl = \sum_i (c\dot{l}_i^2) dt. \end{aligned} \tag{A.4}$$

The resulting equations of motion have the matrix form

$$\mathbf{M(x)\ddot{x}} + \mathbf{V(x,\dot{x})} = \boldsymbol{\tau}, \tag{A.5}$$

where **M** is the mass matrix, **V** is the velocity dependant vector, $\boldsymbol{\tau}$ is the input torque vector and **x** is the state vector. The flight phase is governed by the following system:

$$\mathbf{x}_{fl} = \begin{bmatrix} x \\ y \\ \theta \end{bmatrix}, \quad \mathbf{M(x)}_{fl} = \begin{bmatrix} m & 0 & 0 \\ 0 & m & 0 \\ 0 & 0 & I \end{bmatrix}, \quad \mathbf{V(x,\dot{x})}_{fl} = \begin{bmatrix} 0 \\ mg \\ 0 \end{bmatrix}, \quad \boldsymbol{\tau}_{fl} = \begin{bmatrix} 0 \\ 0 \\ 0 \end{bmatrix}.$$

A.2. Rear Leg Stance

For the rear leg stance phase, the kinetic (T) and potential (V) energies are respectively defined as

$$\begin{aligned} T &= \tfrac{1}{2} m \dot{x}_c^2 + \tfrac{1}{2} m \dot{y}_c^2 + \tfrac{1}{2} I \dot{\theta}_c^2 \\ V &= mgy_c + \tfrac{1}{2} k (l_r - l_{ro})^2. \end{aligned} \tag{A.6}$$

Note that the origin is with respect to an inertial frame of reference. The following kinematic constraints relate the body's center of mass to the platform's parameters:

$$\begin{aligned} x_c &= (\gamma_r - \theta - \phi_r)r_w - l_r \sin(\theta + \phi_r) + l_c \cos\theta \\ y_c &= l_r \cos(\theta + \phi_r) + l_c \sin\theta. \end{aligned} \tag{A.7}$$

Again, the resulting equations of motion have the matrix form

$$\mathbf{M(x)\ddot{x}} + \mathbf{V(x,\dot{x})} = \boldsymbol{\tau}\,. \tag{A.8}$$

The rear leg stance phase is governed by the following system:

$$\mathbf{x}_r = \begin{bmatrix} \theta \\ \phi_r \\ l_r \\ \gamma_r \end{bmatrix}, \quad \mathbf{M(x)}_r = \begin{bmatrix} m_{11} & m_{12} & m_{13} & m_{14} \\ m_{21} & m_{22} & m_{23} & m_{24} \\ m_{31} & m_{32} & m_{33} & m_{34} \\ m_{41} & m_{42} & m_{43} & m_{44} \end{bmatrix}, \quad \mathbf{V(x,\dot{x})}_r = \begin{bmatrix} v_1 \\ v_2 \\ v_3 \\ v_4 \end{bmatrix}, \quad \boldsymbol{\tau}_r = \begin{bmatrix} 0 \\ \tau_{hr} \\ 0 \\ \tau_{wr} \end{bmatrix},$$

where,

$$m_{11} = I + ml_c^2 + mr_w^2 + 2mr_w l_r \cos(\theta + \phi_r) + ml_r^2 + 2ml_c r_w \sin\theta - 2ml_c l_r \sin\phi_r$$
$$m_{12} = ml_c r_w \sin\theta + mr_w^2 - ml_c l_r \sin\phi_r + 2ml_r r_w \cos(\theta + \phi_r) + ml_r^2$$
$$m_{13} = ml_c \cos\phi_r + mr_w \sin(\theta + \phi_r)$$
$$m_{14} = -ml_c r_w \sin\theta - mr_w^2 - mr_w l_r \cos(\theta + \phi_r)$$

$$m_{21} = ml_c r_w \sin\theta + mr_w^2 - ml_c l_r \sin\phi_r + 2mr_w l_r \cos(\theta + \phi_r) + ml_r^2$$
$$m_{22} = mr_w^2 + 2mr_w l_r \cos(\theta + \phi_r) + ml_r^2$$
$$m_{23} = mr_w \sin(\theta + \phi_r)$$
$$m_{24} = -mr_w^2 - mr_w l_r \cos(\theta + \phi_r)$$

$$m_{31} = ml_c \cos\phi_r + mr_w \sin(\theta + \phi_r)$$
$$m_{32} = mr_w \sin(\theta + \phi_r)$$
$$m_{33} = m$$
$$m_{34} = -mr_w \sin(\theta + \phi_r)$$

$$
\begin{aligned}
m_{41} &= -ml_c r_w \sin\theta - mr_w^2 - mr_w l_r \cos(\theta+\phi_r) \\
m_{42} &= -mr_w^2 - mr_w l_r \cos(\theta+\phi_r) \\
m_{43} &- mr_w \sin(\theta+\phi_r) \\
m_{44} &= mr_w^2
\end{aligned}
$$

$$
\begin{aligned}
v_1 = {} & 2mr_w \dot{l}_r(\dot{\theta}+\dot{\phi}_r)\cos(\theta+\phi_r) - mgl_r\sin(\theta+\phi_r) + 2ml_r\dot{l}_r(\dot{\theta}+\dot{\phi}_r) \\
& - mr_w l_r(\dot{\theta}+\dot{\phi}_r)^2\sin(\theta+\phi_r) + ml_c(g+r_w\dot{\theta}^2)\cos\theta - 2ml_c\dot{l}_r(\dot{\theta}+\dot{\phi}_r)\sin\phi_r \\
& - ml_c l_r\dot{\phi}_r(2\dot{\theta}+\dot{\phi}_r)\cos\phi_r \\
v_2 = {} & ml_c r_w\dot{\theta}^2\cos\theta + 2mr_w\dot{l}_r(\dot{\theta}+\dot{\phi}_r)\cos(\theta+\phi_r) - mgl_r\sin(\theta+\phi_r) - ml_c l_r\dot{\theta}^2\cos\phi_r \\
& - 2ml_r\dot{l}_r(\dot{\theta}+\dot{\phi}_r) + mr_w l_r(\dot{\theta}+\dot{\phi}_r)^2\sin(\theta+\phi_r) \\
v_3 = {} & k(l_r - l_{ro}) + mg\cos(\theta+\phi_r) + ml_c\dot{\theta}^2\sin\phi_r - ml_r(\dot{\theta}+\dot{\phi}_r^2)^2 + c\dot{l}_r \\
v_4 = {} & -ml_c r_w\dot{\theta}^2\cos\theta + mr_w(\dot{\theta}+\dot{\phi}_r)(-2\dot{l}_r\cos(\theta+\phi_r) + l_r(\dot{\theta}+\dot{\phi}_r)\sin(\theta+\phi_r))
\end{aligned}
$$

A.3. Front Leg Stance

For the front leg stance phase, the kinetic (T) and potential (V) energies are respectively defined as

$$
\begin{aligned}
T &= \tfrac{1}{2}m\dot{x}_c^2 + \tfrac{1}{2}m\dot{y}_c^2 + \tfrac{1}{2}I\dot{\theta}_c^2 \\
V &= mgy_c + \tfrac{1}{2}k(l_f - l_{fo})^2.
\end{aligned} \tag{A.9}
$$

Note that the origin is with respect to an inertial frame of reference. The following kinematic constraints relate the body's center of mass to the platform's parameters:

$$
\begin{aligned}
x_c &= (\gamma_f - \theta - \phi_f)r_w - l_f\sin(\theta+\phi_f) - l_c\cos\theta \\
y_c &= l_f\cos(\theta+\phi_f) - l_c\sin\theta.
\end{aligned} \tag{A.10}
$$

Again, the resulting equations of motion have the matrix form

$$
\mathbf{M(x)\ddot{x}} + \mathbf{V(x,\dot{x})} = \boldsymbol{\tau}. \tag{A.11}
$$

The front leg stance phase is governed by the following system:

$$\mathbf{x}_f = \begin{bmatrix} \theta \\ \phi_f \\ l_f \\ \gamma_f \end{bmatrix}, \quad \mathbf{M}(\mathbf{x})_f = \begin{bmatrix} m_{11} & m_{12} & m_{13} & m_{14} \\ m_{21} & m_{22} & m_{23} & m_{24} \\ m_{31} & m_{32} & m_{33} & m_{34} \\ m_{41} & m_{42} & m_{43} & m_{44} \end{bmatrix}, \quad \mathbf{V}(\mathbf{x},\dot{\mathbf{x}})_f = \begin{bmatrix} v_1 \\ v_2 \\ v_3 \\ v_4 \end{bmatrix}, \quad \boldsymbol{\tau}_r = \begin{bmatrix} 0 \\ \tau_{hf} \\ 0 \\ \tau_{wf} \end{bmatrix},$$

where,

$$m_{11} = I + ml_c^2 + mr_w^2 + 2mr_w l_f \cos(\theta + \phi_f) + ml_f^2 - 2ml_c r_w \sin\theta + 2ml_c l_f \sin\phi_f$$
$$m_{12} = -ml_c r_w \sin\theta + mr_w^2 + ml_c l_f \sin\phi_f + 2ml_f r_w \cos(\theta + \phi_f) + ml_f^2$$
$$m_{13} = -ml_c \cos\phi_f + mr_w \sin(\theta + \phi_f)$$
$$m_{14} = ml_c r_w \sin\theta - mr_w^2 - mr_w l_f \cos(\theta + \phi_f)$$

$$m_{21} = -ml_c r_w \sin\theta + mr_w^2 + ml_c l_f \sin\phi_f + 2mr_w l_f \cos(\theta + \phi_f) + ml_f^2$$
$$m_{22} = mr_w^2 + 2mr_w l_f \cos(\theta + \phi_f) + ml_f^2$$
$$m_{23} = mr_w \sin(\theta + \phi_f)$$
$$m_{24} = -mr_w^2 - mr_w l_f \cos(\theta + \phi_f)$$

$$m_{31} = -ml_c \cos\phi_f + mr_w \sin(\theta + \phi_f)$$
$$m_{32} = mr_w \sin(\theta + \phi_f)$$
$$m_{33} = m$$
$$m_{34} = -mr_w \sin(\theta + \phi_f)$$

$$m_{41} = ml_c r_w \sin\theta - mr_w^2 - mr_w l_r \cos(\theta + \phi_r)$$
$$m_{42} = -mr_w^2 - mr_w l_r \cos(\theta + \phi_r)$$
$$m_{43} - mr_w \sin(\theta + \phi_r)$$
$$m_{44} = mr_w^2$$

$$\begin{aligned} v_1 = {} & 2mr_w \dot{l}_f (\dot{\theta} + \dot{\phi}_f)\cos(\theta + \phi_f) - mgl_f \sin(\theta + \phi_f) - 2ml_f \dot{l}_f (\dot{\theta} + \dot{\phi}_f) \\ & + mr_w l_f (\dot{\theta} + \dot{\phi}_f)^2 \sin(\theta + \phi_f) - ml_c (g + r_w \dot{\theta}^2)\cos\theta + 2ml_c \dot{l}_f (\dot{\theta} + \dot{\phi}_f)\sin\phi_f \\ & + ml_c l_f \dot{\phi}_f (2\dot{\theta} + \dot{\phi}_f)\cos\phi_f \end{aligned}$$
$$\begin{aligned} v_2 = {} & -ml_c r_w \dot{\theta}^2 \cos\theta + 2mr_w \dot{l}_f (\dot{\theta} + \dot{\phi}_f)\cos(\theta + \phi_f) - mgl_f \sin(\theta + \phi_f) - ml_c l_f \dot{\theta}^2 \cos\phi_f \\ & - 2ml_f \dot{l}_f (\dot{\theta} + \dot{\phi}_f) - mr_w l_f (\dot{\theta} + \dot{\phi}_f)^2 \sin(\theta + \phi_f) \end{aligned}$$
$$v_3 = k(l_f - l_{fo}) + mg\cos(\theta + \phi_f) - ml_c \dot{\theta}^2 \sin\phi_f - ml_f (\dot{\theta} + \dot{\phi}_f^2)^2 + c\dot{l}_f$$
$$v_4 = ml_c r_w \dot{\theta}^2 \cos\theta + mr_w (\dot{\theta} + \dot{\phi}_f)(-2\dot{l}_f \cos(\theta + \phi_f) + l_f (\dot{\theta} + \dot{\phi}_f)\sin(\theta + \phi_f))$$

A.4. Double Leg Stance

For the double leg stance phase, the kinetic (T) and potential (V) energies are respectively defined as

$$\begin{aligned} T &= \tfrac{1}{2} m \dot{x}_c^2 + \tfrac{1}{2} m \dot{y}_c^2 + \tfrac{1}{2} I \dot{\theta}_c^2 \\ V &= m g y_c + \tfrac{1}{2} k (l_r - l_{ro})^2 + \tfrac{1}{2} k (l_f - l_{fo})^2 . \end{aligned} \tag{A.12}$$

Note that the origin is with respect to an inertial frame of reference. The following kinematic relationships constrain the center of mass to positions dictated by the position of the rear wheel.

$$x_c = (\gamma_r - \theta - \phi_r) r_w - l_r \sin(\theta + \phi_r) + l_c \cos\theta \tag{A.13.a}$$

$$y_c = l_r \cos(\theta + \phi_r) + l_c \sin\theta \tag{A.13.b}$$

For a double stance, further kinematic constraints are required to properly model the phase. These of course are the relationships which describe how the front wheel's position constrains the center of mass in conjunction with the rear wheel's position:

$$\begin{aligned} x_f = {} & (\gamma_r - \theta - \phi_r) r_w - l_r \sin(\theta + \phi_r) + 2 l_c \cos\theta + \\ & l_f \sin(\theta + \phi_f) + (\gamma_f - \theta - \phi_f) r_w \end{aligned} \tag{A.14.a}$$

$$y_f = l_r \cos(\theta + \phi_r) + 2 l_c \sin\theta - l_f \cos(\theta + \phi_f) \tag{A.14.b}$$

The variables x_f and y_f represent the position of the front wheel's center at the start of the double stance phase. They are considered to be known inputs at the start of this phase. Solving eq. (A.14.a) and (A.14.b) for l_c yields,

$$\begin{aligned} (l_c)_x = \frac{1}{2\cos\theta} \Big(& x_f - (\gamma_r - \theta - \phi_r) r_w + l_r \sin(\theta + \phi_r) - l_f \sin(\theta + \phi_f) \\ & - (\gamma_f - \theta - \phi_f) r \Big) \end{aligned} \tag{A.15.a}$$

$$(l_c)_y = \frac{1}{2\cos\theta} \left(y_f - l_r \cos(\theta + \phi_r) + l_f \cos(\theta + \phi_f) \right) \tag{A.15.b}$$

The substitution of eq. (A.15.a) into eq. (A.13.a) and eq. (A.15.b) into eq. (A.13.b) results in properly constrained equations for the center of mass.

$$x_c = \tfrac{1}{2}\big(x_f + (\gamma_r - \theta - \phi_r)r_w - l_r \sin(\theta + \phi_r) - l_f \sin(\theta + \phi_f) \\ - (\gamma_f - \theta - \phi_f)r_w\big) \tag{A.16.a}$$

$$y_c = \tfrac{1}{2}\big(y_f + l_r \cos(\theta + \phi_r) + 2l_c \sin\theta + l_f \cos(\theta + \phi_f)\big) \tag{A.16.b}$$

Using the above expressions for the center of mass in eq. (A.12), the resulting equations of motion again have the matrix form

$$\mathbf{M(x)\ddot{x}} + \mathbf{V(x,\dot{x})} = \boldsymbol{\tau}\,. \tag{A.17}$$

This single expression is sufficient to fully model this phase without the need for a separate expression embodying the kinematic constraints. The double leg stance phase is governed by the following system:

$$\mathbf{x}_r = \begin{bmatrix} \theta \\ \phi_r \\ l_r \\ \gamma_r \\ \phi_f \\ l_f \\ \gamma_f \end{bmatrix}, \quad \mathbf{M(x)}_r = \begin{bmatrix} m_{11} & m_{12} & m_{13} & m_{14} & m_{15} & m_{16} & m_{17} \\ m_{21} & m_{22} & m_{23} & m_{24} & m_{25} & m_{26} & m_{27} \\ m_{31} & m_{32} & m_{33} & m_{34} & m_{35} & m_{36} & m_{37} \\ m_{41} & m_{42} & m_{43} & m_{44} & m_{45} & m_{46} & m_{47} \\ m_{51} & m_{52} & m_{53} & m_{54} & m_{55} & m_{56} & m_{57} \\ m_{61} & m_{62} & m_{63} & m_{64} & m_{65} & m_{66} & m_{67} \\ m_{71} & m_{72} & m_{73} & m_{74} & m_{75} & m_{76} & m_{77} \end{bmatrix}, \quad \mathbf{V(x,\dot{x})}_r = \begin{bmatrix} v_1 \\ v_2 \\ v_3 \\ v_4 \\ v_5 \\ v_6 \\ v_7 \end{bmatrix},$$

$$\boldsymbol{\tau}_r = \begin{bmatrix} 0 \\ \tau_{hr} \\ 0 \\ \tau_{wr} \\ \tau_{hf} \\ 0 \\ \tau_{wf} \end{bmatrix},$$

where

$$m_{11} = \tfrac{1}{4}\big(4I + ml_f^2 + ml_r^2 + 2ml_f l_r \cos(\phi_f - \phi_r)\big)$$
$$m_{12} = \tfrac{1}{4}m\big(l_f l_r \cos(\phi_f - \phi_r) + l_r^2 + r_w l_f \cos(\theta + \phi_f) + r_w l_r \cos(\theta + \phi_r)\big)$$
$$m_{13} = -\tfrac{1}{4}ml_f \sin(\phi_f - \phi_r)$$

$$m_{14} = -\tfrac{1}{4} m r_w \left(l_f \cos(\theta + \phi_f) + l_r \cos(\theta + \phi_r) \right)$$
$$m_{15} = \tfrac{1}{4} m \left(l_f^2 + l_f l_r \cos(\phi_f - \phi_r) - r_w l_f \cos(\theta + \phi_f) + r_w l_r \cos(\theta + \phi_r) \right)$$
$$m_{16} = \tfrac{1}{4} m l_r \sin(\phi_f - \phi_r)$$
$$m_{17} = \tfrac{1}{4} m r_w \left(l_f \cos(\theta + \phi_f) + l_r \cos(\theta + \phi_r) \right)$$

$$m_{21} = \tfrac{1}{4} m \left(l_f l_r \cos(\phi_f - \phi_r) + l_r^2 + r_w l_f \cos(\theta + \phi_f) + r_w l_r \cos(\theta + \phi_r) \right)$$
$$m_{22} = \tfrac{1}{4} m \left(r_w^2 + l_r^2 + 2 r_w l_r \cos(\theta + \phi_r) \right)$$
$$m_{23} = \tfrac{1}{4} m r_w \sin(\theta + \phi_r)$$
$$m_{24} = -\tfrac{1}{4} m r_w \left(l_r \cos(\theta + \phi_r) + r_w \right)$$
$$m_{25} = \tfrac{1}{4} m \left(-r_w l_r \cos(\theta + \phi_r) - r_w^2 + l_f l_r \cos(\phi_f - \phi_r) + r_w l_f \cos(\theta + \phi_f) \right)$$
$$m_{26} = \tfrac{1}{4} m \left(l_r \sin(\phi_f - \phi_r) + r_w \sin(\theta + \phi_f) \right)$$
$$m_{27} = \tfrac{1}{4} m r_w \left(l_r \cos(\theta + \phi_r) + r_w \right)$$

$$m_{31} = -\tfrac{1}{4} m l_f \sin(\phi_f - \phi_r)$$
$$m_{32} = \tfrac{1}{4} m r_w \sin(\theta + \phi_r)$$
$$m_{33} = \tfrac{1}{4} m$$
$$m_{34} = -\tfrac{1}{4} m r_w \sin(\theta + \phi_r)$$
$$m_{35} = -\tfrac{1}{4} m \left(l_f \sin(\phi_f - \phi_r) + r_w \sin(\theta + \phi_r) \right)$$
$$m_{36} = \tfrac{1}{4} m \cos(\phi_f - \phi_r)$$
$$m_{37} = \tfrac{1}{4} m r_w \sin(\theta + \phi_r)$$

$$m_{41} = -\tfrac{1}{4} m r_w \left(l_f \cos(\theta + \phi_f) + l_r \cos(\theta + \phi_r) \right)$$
$$m_{42} = -\tfrac{1}{4} m r_w \left(l_r \cos(\theta + \phi_r) + r_w \right)$$
$$m_{43} = -\tfrac{1}{4} m r_w \sin(\theta + \phi_r)$$
$$m_{44} = \tfrac{1}{4} m r_w^2$$
$$m_{45} = -\tfrac{1}{4} m r_w \left(l_f \cos(\theta + \phi_f) - r_w \right)$$
$$m_{46} = -\tfrac{1}{4} m r_w \sin(\theta + \phi_f)$$
$$m_{47} = -\tfrac{1}{4} m r_w^2$$

$$m_{51} = \tfrac{1}{4} m \left(l_f^2 + l_f l_r \cos(\phi_f - \phi_r) - r_w l_f \cos(\theta + \phi_f) - r_w l_r \cos(\theta + \phi_r) \right)$$
$$m_{52} = \tfrac{1}{4} m \left(-r_w^2 - r_w l_r \cos(\theta + \phi_r) + l_f l_r \cos(\phi_f - \phi_r) + r_w l_f \cos(\theta + \phi_f) \right)$$

$$m_{51} = \tfrac{1}{4}m\left(l_f^2 + l_f l_r \cos(\phi_f - \phi_r) - r_w l_f \cos(\theta + \phi_f) - r_w l_r \cos(\theta + \phi_r)\right)$$
$$m_{52} = \tfrac{1}{4}m\left(-r_w^2 - r_w l_r \cos(\theta + \phi_r) + l_f l_r \cos(\phi_f - \phi_r) + r_w l_f \cos(\theta + \phi_f)\right)$$
$$m_{53} = -\tfrac{1}{4}m\left(l_f \sin(\phi_f - \phi_r) + r_w \sin(\theta + \phi_r)\right)$$
$$m_{54} = -\tfrac{1}{4}mr_w\left(l_f \cos(\theta + \phi_f) - r_w\right)$$
$$m_{55} = \tfrac{1}{4}m\left(l_f^2 - 2r_w l_f \cos(\theta + \phi_f) + r_w^2\right)$$
$$m_{56} = -\tfrac{1}{4}mr_w \sin(\theta + \phi_f)$$
$$m_{57} = \tfrac{1}{4}mr_w\left(l_f \cos(\theta + \phi_f) - r_w\right)$$

$$m_{61} = \tfrac{1}{4}ml_r \sin(\phi_f - \phi_r)$$
$$m_{62} = \tfrac{1}{4}m\left(l_r \sin(\phi_f - \phi_r) + r_w \sin(\theta + \phi_f)\right)$$
$$m_{63} = \tfrac{1}{4}m \cos(\phi_f - \phi_r)$$
$$m_{64} = -\tfrac{1}{4}mr_w \sin(\theta + \phi_f)$$
$$m_{65} = -\tfrac{1}{4}mr_w \sin(\theta + \phi_f)$$
$$m_{66} = \tfrac{1}{4}m$$
$$m_{67} = \tfrac{1}{4}mr_w \sin(\theta + \phi_f)$$

$$m_{71} = \tfrac{1}{4}r_w\left(l_f \cos(\theta + \phi_f) + l_r \cos(\theta + \phi_r)\right)$$
$$m_{72} = \tfrac{1}{4}mr_w\left(l_r \cos(\theta + \phi_r) + r_w\right)$$
$$m_{73} = \tfrac{1}{4}mr_w \sin(\theta + \phi_r)$$
$$m_{74} = -\tfrac{1}{4}mr_w^2$$
$$m_{75} = \tfrac{1}{4}mr_w\left(l_f \cos(\theta + \phi_f) - r_w\right)$$
$$m_{76} = \tfrac{1}{4}mr_w \sin(\theta + \phi_f)$$
$$m_{77} = \tfrac{1}{4}mr_w^2$$

$$\begin{aligned}
v_1 = \tfrac{1}{4}m(&2l_f \dot{l}_r \dot{\theta} \cos(\phi_f - \phi_r) - 2l_f l_r \dot{\theta}\dot{\phi}_f \sin(\phi_f - \phi_r) - l_f l_r \dot{\phi}_f^2 \sin(\phi_f - \phi_r) + 2l_f \dot{l}_f (\dot{\theta} + \dot{\phi}_f) \\
&+ 2l_f \dot{l}_r \dot{\phi}_r \cos(\phi_f - \phi_r) + 2l_f l_r \dot{\theta}\dot{\phi}_r \sin(\phi_f - \phi_r) + l_f l_r \dot{\phi}_r^2 \sin(\phi_f - \phi_r) \\
&+ 2l_r \dot{l}_f (\dot{\theta} + \dot{\phi}_r) \cos(\phi_f - \phi_r) + 2l_r \dot{l}_r (\dot{\theta} + \dot{\phi}_r))
\end{aligned}$$

$$\begin{aligned}
v_2 = \tfrac{1}{4}m(&2l_r \dot{l}_r \dot{\theta} - l_f l_r \dot{\theta}^2 \sin(\phi_f - \phi_r) - r_w l_r \dot{\theta}^2 \sin(\theta + \phi_r) - 2l_f l_r \dot{\theta}\dot{\phi}_f \sin(\phi_f - \phi_r) \\
&- l_f l_r \dot{\phi}_f \sin(\phi_f - \phi_r) + 2l_r \dot{l}_f (\dot{\theta} + \dot{\phi}_f) \cos(\phi_f - \phi_r) + 2l_r \dot{l}_r \dot{\phi}_r - 2r_w l_r \dot{\theta}\dot{\phi}_r \sin(\theta + \phi_r) \\
&- r_w l_r \dot{\phi}_r^2 \sin(\theta + \phi_r) + 2r_w \dot{l}_f (\dot{\theta} + \dot{\phi}_f) \cos(\theta + \phi_f) - r_w l_f (\dot{\theta} + \dot{\phi}_f)^2 \sin(\theta + \phi_f) \\
&+ 2r_w \dot{l}_r (\dot{\theta} + \dot{\phi}_r) \cos\theta \cos\phi_r - 2r_w \dot{l}_r (\dot{\theta} + \dot{\phi}_r) \sin\theta \sin\phi_r)
\end{aligned}$$

$$v_3 = \tfrac{1}{4}(-4kl_{ro} - 2m\dot{l}_f(\dot{\theta}+\dot{\phi}_f)\sin(\phi_f-\phi_r) - ml_f(\dot{\theta}+\dot{\phi}_f)^2\cos(\phi_f-\phi_r) + 4kl_r - ml_r(\dot{\theta}+\dot{\phi}_r)^2$$
$$+ c\dot{l}_r$$
$$v_4 = \tfrac{1}{4}mr_w(-2\dot{l}_f(\dot{\theta}+\dot{\phi}_f)\cos(\theta+\phi_f) + l_f(\dot{\theta}+\dot{\phi}_f)^2\sin(\theta+\phi_f) + 2\dot{l}_r(\dot{\theta}+\dot{\phi}_r)\sin\theta\sin\phi_r$$
$$+ l_r(\dot{\theta}+\dot{\phi}_r)^2\cos\theta\sin\phi_r - 2\dot{l}_r(\dot{\theta}+\dot{\phi}_r)\cos\theta\cos\phi_r + l_r(\dot{\theta}+\dot{\phi}_r)^2\sin\theta\cos\phi_r)$$
$$v_5 = \tfrac{1}{4}m(-2r_w\dot{l}_f(\dot{\theta}+\dot{\phi}_f)\cos(\theta+\phi_f) + 2l_f\dot{l}_f(\dot{\theta}+\dot{\phi}_f) + r_wl_f(\dot{\theta}+\dot{\phi}_f)^2\sin(\theta+\phi_f)$$
$$+ 2r_w\dot{l}_r(\dot{\theta}+\dot{\phi}_r)\sin\theta\sin\phi_r + r_wl_r(\dot{\theta}+\dot{\phi}_r)^2\cos\theta\sin\phi_r + 2l_f\dot{l}_r(\dot{\theta}+\dot{\phi}_r)\sin\phi_f$$
$$- l_fl_r(\dot{\theta}+\dot{\phi}_r)^2\cos\phi_f\sin\phi_r - 2r_w\dot{l}_r(\dot{\theta}+\dot{\phi}_r)\cos\theta\cos\phi_r + r_wl_r(\dot{\theta}+\dot{\phi}_r)^2\sin\theta\cos\phi_r$$
$$+ 2l_f\dot{l}_r(\dot{\theta}+\dot{\phi}_r)\cos\phi_f\cos\phi_r + l_fl_r(\dot{\theta}+\dot{\phi}_r)^2\sin\phi_f\cos\phi_r)$$
$$v_6 = \tfrac{1}{4}(-4kl_{fo} + 4kl_f - ml_f(\dot{\theta}+\dot{\phi}_f)^2 + 2m\dot{l}_r(\dot{\theta}+\dot{\phi}_r)\sin(\phi_f-\phi_r) - ml_r(\dot{\theta}+\dot{\phi}_r)^2\cos(\phi_f-\phi_r))$$
$$+ c\dot{l}_f$$
$$v_7 = \tfrac{1}{4}mr_w(2\dot{l}_f(\dot{\theta}+\dot{\phi}_f)\cos(\theta+\phi_f) - l_f(\dot{\theta}+\dot{\phi}_f)^2\sin(\theta+\phi_f) + 2\dot{l}_r(\dot{\theta}+\dot{\phi}_r)\sin\theta\sin\phi_r$$
$$+ l_r(\dot{\theta}+\dot{\phi}_r)^2\cos\theta\sin\phi_r) + 2\dot{l}_r(\dot{\theta}+\dot{\phi}_r)\cos\theta\cos\phi_r + l_r(\dot{\theta}+\dot{\phi}_r)^2\sin\theta\cos\phi_r)$$

Appendix B

Assembly Drawings for Testbed

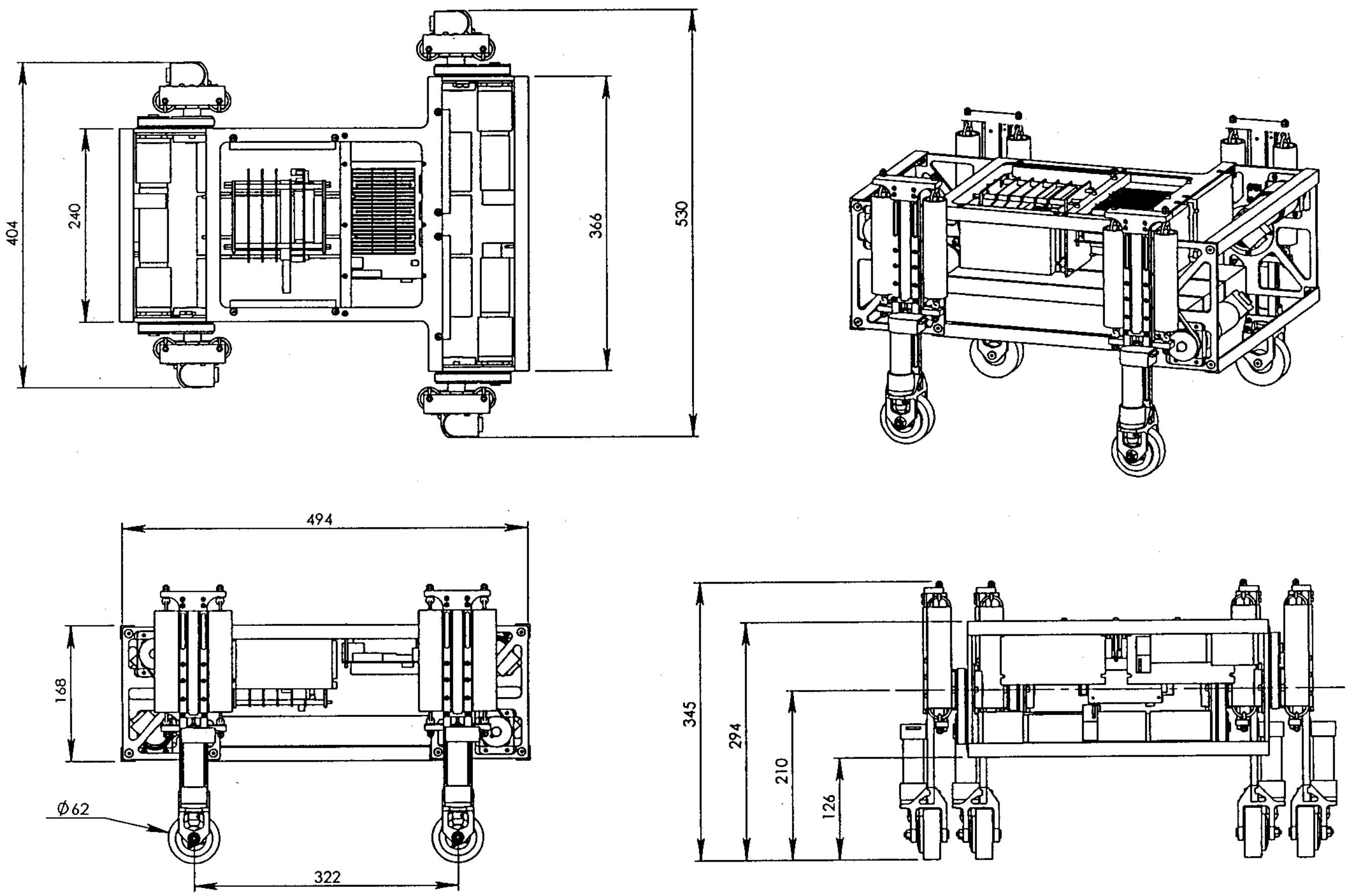

SolidWorks Educational License
Instructional Use Only

DIMENSIONS ARE IN mm
TOLERANCES:
ANGULAR:
MACH± 0.5°
BEND ± 1°
ONE PLACE DECIMAL ± .1
TWO PLACE DECIMAL ± .03

MATERIAL
—

FINISH
—

APPLICATION
ANT 1.0

	NAME	DATE
DRAWN	C STEEVES	2002/09/01
CHECKED	X	YYYY/MM/DD
ENG APPR.	X	YYYY/MM/DD

DO NOT SCALE DRAWING

COMMENTS:

McGILL UNIVERSITY
DEPT. OF MECHANICAL ENGINEERING
CENTRE FOR INTELLIGENT MACHINES
AMBULATORY ROBOTICS LAB

SIZE	DWG. NO.	REV.
A	PLATFORM DIMENSIONS	NC

WEIGHT:

SHEET 1 OF 1

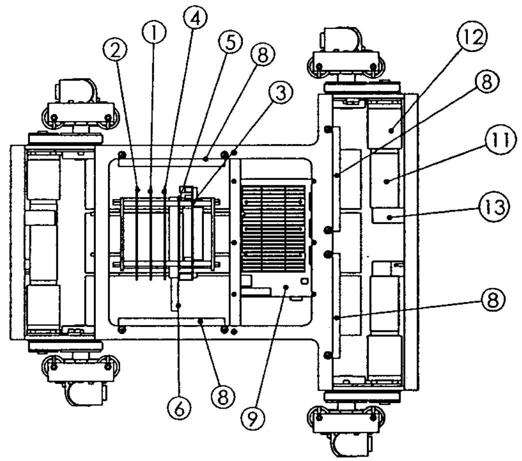

ITEM	QUAN.	NAME	DESCRIPTION
1	1	PC/104 POWER SUPPLY	RTD EPWR104HR-25/25W
2	1	PC/104 QUAD. DECODER	MICROCOMPUTER SYSTEMS MSI-P400
3	1	PC/104 COMPUTER BOARD	LIPPERT COOLROAD RUNNER II
4	1	PC/104 CUSTOM I/O BOARD	CUSTOM INTERFACE CARD
5	1	PC/104 PCMCIA ADAPTER BOARD	VERSALOGIC PCM-3115
6	1	PCMCIA WIRELESS ETHERNET CARD	ORINOCO GOLD 11 MBITS/S
7	8	SPRING	SPEC E1125-125-5000 M
8	4	HIP SERVO AMPLIFIER	AMC 25A8 SERVO AMP
9	1	WHEEL DRIVER BOARD	CUSTOM BOARD WITH APEX SA60 CHIPS
10	3	BATTERY PACK	BATTLEPACK - 10 SANYO HRD CELLS
11	4	HIP MOTOR	MAXON RE 35 (118777)
12	4	HIP GEARHEAD	MAXON GP42C (203116)
13	4	HIP ENCODER	HP HEDS 5540 A11
14	4	WHEEL MOTOR	MAXON RE 25 (118751)
15	4	WHEEL GEARHEAD	MAXON GP32C (233147)
16	4	WHEEL ENCODER	HP HEDS 5540 A02
17	4	POTENTIOMETER	MIDORI LP-100FP 5KOHM

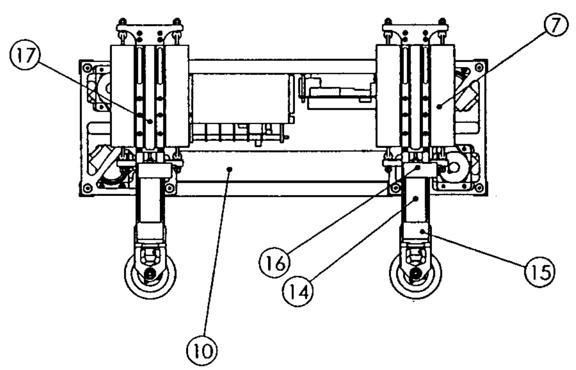

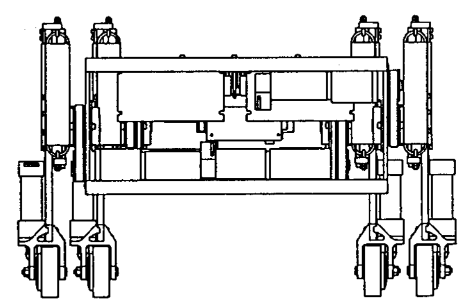

SolidWorks Educational License
Instructional Use Only

DIMENSIONS ARE IN mm TOLERANCES: ANGULAR: MACH ± 0.5° BEND ± 1° ONE PLACE DECIMAL ± .1 TWO PLACE DECIMAL ± .03		NAME	DATE
	DRAWN	C STEEVES	2002/09/01
	CHECKED	X	YYYY/MM/DD
	ENG APPR.	X	YYYY/MM/DD
	DO NOT SCALE DRAWING		
MATERIAL –	COMMENTS:		
FINISH –			
APPLICATION ANT 1.0			

McGILL UNIVERSITY
DEPT. OF MECHANICAL ENGINEERING
CENTRE FOR INTELLIGENT MACHINES
AMBULATORY ROBOTICS LAB

SIZE	DWG. NO.	REV.
A	PLATFORM COMPONENTS	NC

WEIGHT: SHEET 1 OF 1

ITEM	QUAN.	NAME	DESCRIPTION
1	4	HIP PLATE	AL 7075-T6
2	1	TOP BRACE	AL 7075-T6
3	1	BOTTOM BRACE	AL 7075-T6
4	2	FRONT BRACE	AL 7075-T6
5	2	REAR BRACE	AL 7075-T6
6	16	SOCKET BOLT M5 X 16 COUNTER SINK	DIN 7991-M5X16
7	16	NY LOC NUT M5	DIN 985 M5

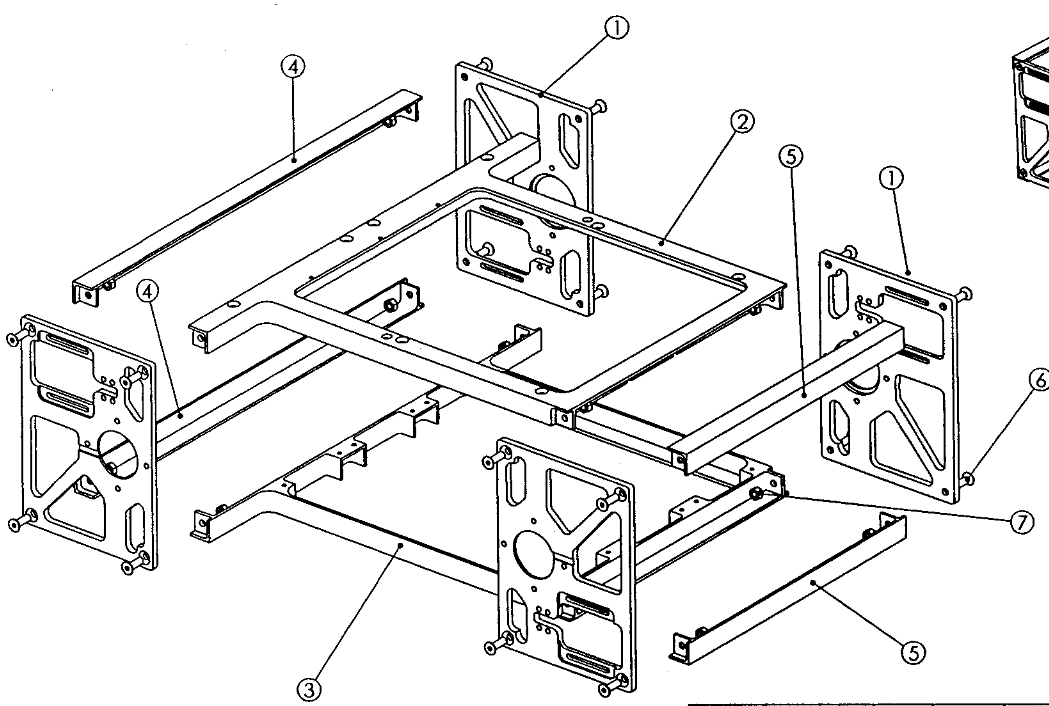

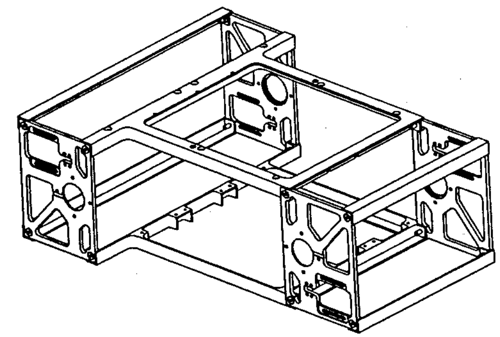

ASSEMBLED VIEW

SolidWorks Educational License
Instructional Use Only

DIMENSIONS ARE IN mm TOLERANCES: ANGULAR: MACH ± 0.5° BEND ± 1° ONE PLACE DECIMAL ± .1 TWO PLACE DECIMAL ± .03		NAME	DATE
	DRAWN	C. STEEVES	2002/09/01
	CHECKED	X	YYYY/MM/DD
	ENG APPR.	X	YYYY/MM/DD
	DO NOT SCALE DRAWING		
MATERIAL –	COMMENTS:		
FINISH –			
APPLICATION ANT 1.0			

McGILL UNIVERSITY
DEPT. OF MECHANICAL ENGINEERING
CENTRE FOR INTELLIGENT MACHINES
AMBULATORY ROBOTICS LAB

SIZE	DWG. NO.	REV.
A	FRAME ASSEMBLY	NC
	WEIGHT:	SHEET 1 OF 1

ITEM	QUAN.	NAME	DESCRIPTION
1	1	TOP BRACE	AL 7075-T6
2	1	AMPLIFIER BRACE	AL EXT. ARC. GRADE
3	4	HIP SERVO AMPLIFIER	AMC 25A8 SERVO AMP
4	8	SOCKET BOLT M4 X 16 COUNTER SINK	DIN 7991-M4X16
5	2	SOCKET BOLT M3 X 10 COUNTER SINK	DIN 7991-M3X10
6	8	NYLOC NUT M4	DIN 985 M4
7	2	NYLOC NUT M3	DIN 985 M3

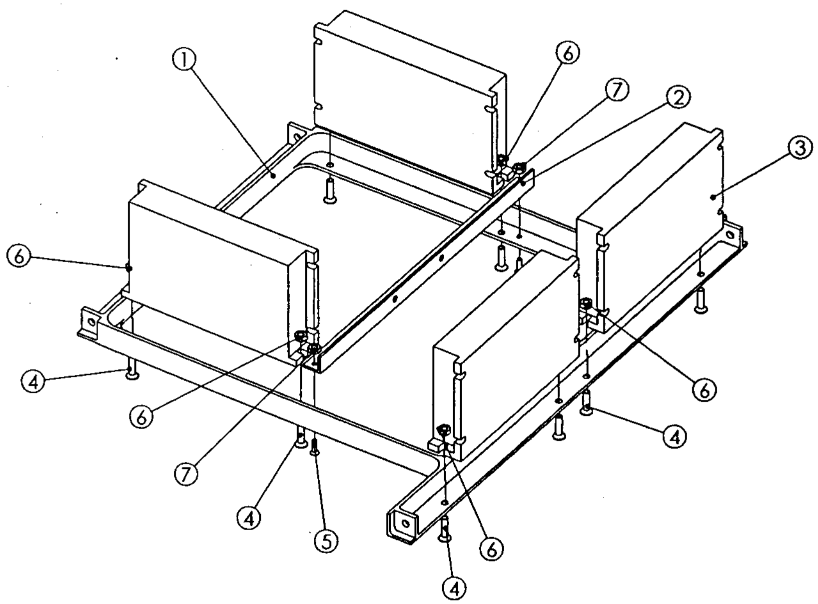

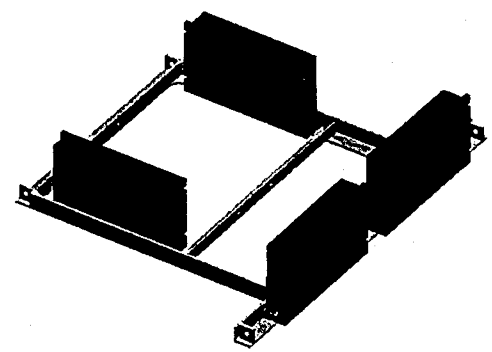

ASSEMBLED VIEW

SolidWorks Educational License
Instructional Use Only

DIMENSIONS ARE IN mm TOLERANCES: ANGULAR: MACH± 0.5° BEND ± 1° ONE PLACE DECIMAL ± .1 TWO PLACE DECIMAL ± .03		NAME	DATE	McGILL UNIVERSITY DEPT. OF MECHANICAL ENGINEERING CENTRE FOR INTELLIGENT MACHINES AMBULATORY ROBOTICS LAB
	DRAWN	C. STEEVES	2002/09/01	
	CHECKED	X	YYYY/MM/DD	
	ENG APPR.	X	YYYY/MM/DD	
	DO NOT SCALE DRAWING			
MATERIAL –	COMMENTS:			SIZE A · DWG. NO. TOP BRACE ASSEMBLY · REV. NC
FINISH –				
APPLICATION ANT 1.0				WEIGHT: · SHEET 1 OF 3

ITEM	QUAN.	NAME	DESCRIPTION
1	1	PC/104 POWER SUPPLY	RTD EPWR104HR-25/25W
2	1	PC/104 QUAD. DECODER	MICROCOMPUTER SYSTEMS MSI-P400
3	1	PC/104 COMPUTER BOARD	LIPPERT COOLROAD RUNNER II
4	1	PC/104 CUSTOM I/O BOARD	CUSTOM INTERFACE CARD
5	1	PC/104 PCMCIA ADAPTER BOARD	VERSALOGIC PCM-3115
6	1	PCMCIA WIRELESS ETHERNET CARD	ORINOCO GOLD 11 MBITS/S
7	1	WHEEL DRIVER BOARD	CUSTOM BOARD WITH APEX SA60 CHIPS
8	1	PC/104 STACK MOUNT 1	LEXAN 3 MM
9	1	PC/104 STACK MOUNT 2	LEXAN 3 MM
10	4	M3 THREADED ROD	DIN 975 M3 130 MM
11	28	PLASTIC STAND-OFF/SPACER	RICHCO R908-10
12	4	SOCKET BOLT M4 X 40 COUNTER SINK	DIN 7991-M4X40
13	12	NYLOC NUT M4	DIN 985 M4
14	26	NYLOC NUT M3	DIN 985 M3
15	1	AMPLIFIER BRACE	AL EXT. ARC. GRADE
16	1	TOP BRACE	AL 7075-T6
17	6	SOCKET BOLT M3 X 30	DIN 912-M3X30

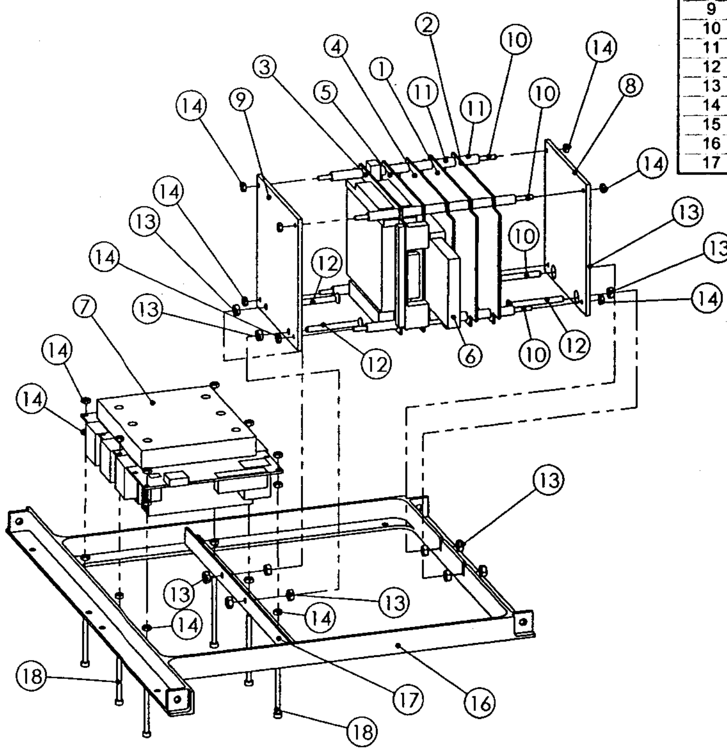

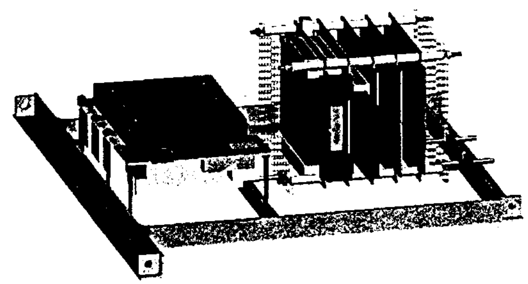

ASSEMBLED VIEW

SolidWorks Educational License
Instructional Use Only

DIMENSIONS ARE IN mm
TOLERANCES:
ANGULAR:
MACH ± 0.5°
BEND ± 1°
ONE PLACE DECIMAL ± .1
TWO PLACE DECIMAL ± .03

	NAME	DATE
DRAWN	C. STEEVES	2002/09/01
CHECKED	X	YYYY/MM/DD
ENG APPR.	X	YYYY/MM/DD

DO NOT SCALE DRAWING

MATERIAL
—
FINISH
—
APPLICATION
ANT 1.0

COMMENTS:

McGILL UNIVERSITY
DEPT. OF MECHANICAL ENGINEERING
CENTRE FOR INTELLIGENT MACHINES
AMBULATORY ROBOTICS LAB

SIZE A | DWG. NO. TOP BRACE ASSEMBLY | REV. NC

WEIGHT: | SHEET 2 OF 3

ITEM	QUAN.	NAME	DESCRIPTION
1	1	TOP BRACE	AL 7075-T6
2	1	AMPLIFIER BRACE	AL EXT. ARC. GRADE
3	4	HIP SERVO AMPLIFIER	AMC 25A8 SERVO AMP
4	1	PC/104 STACK	PC/104 FORM FACTOR STACK - 5 BOARDS
5	1	WHEEL DRIVER BOARD	CUSTOM BOARD WITH APEX SA60 CHIPS

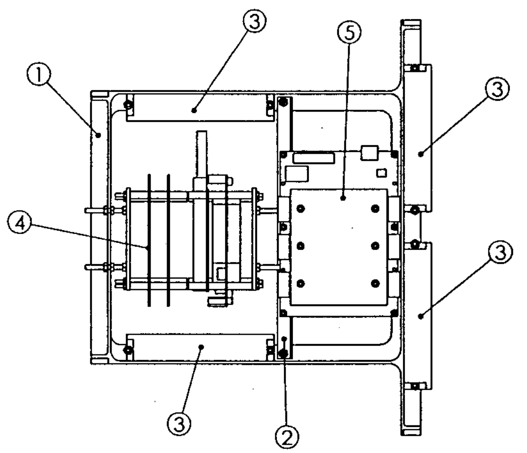

ASSEMBLED VIEW
(TOP VIEW)

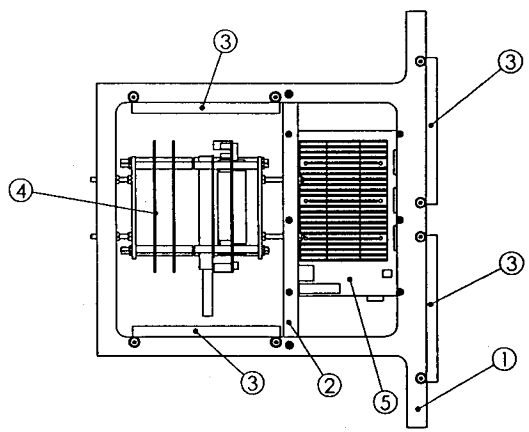

ASSEMBLED VIEW
(BOTTOM VIEW)

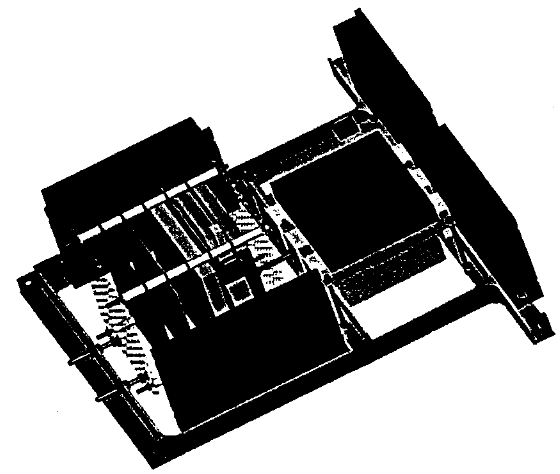

ASSEMBLED VIEW
(ISO VIEW)

SolidWorks Educational License
Instructional Use Only

DIMENSIONS ARE IN mm TOLERANCES: ANGULAR: MACH ± 0.5° BEND ± 1° ONE PLACE DECIMAL ± .1 TWO PLACE DECIMAL ± .03		NAME	DATE	McGILL UNIVERSITY DEPT. OF MECHANICAL ENGINEERING CENTRE FOR INTELLIGENT MACHINES AMBULATORY ROBOTICS LAB
	DRAWN	C. STEEVES	2002/09/01	
	CHECKED	X	YYYY/MM/DD	
	ENG APPR.	X	YYYY/MM/DD	
	DO NOT SCALE DRAWING			
MATERIAL –	COMMENTS:			SIZE: A — DWG. NO.: TOP BRACE ASSEMBLY — REV.: NC
FINISH –				
APPLICATION ANT 1.0				WEIGHT: — SHEET 3 OF 3

ITEM	QUAN.	NAME	DESCRIPTION
1	1	BOTTOM BRACE	AL 7075-T6
2	6	BATTERY BRACE	AL EXT. ARC. GRADE
3	12	SOCKET BOLT M3 X 8 COUNTER SINK	DIN 7991-M3X8
4	8	NYLOC NUT M3	DIN 985 M3

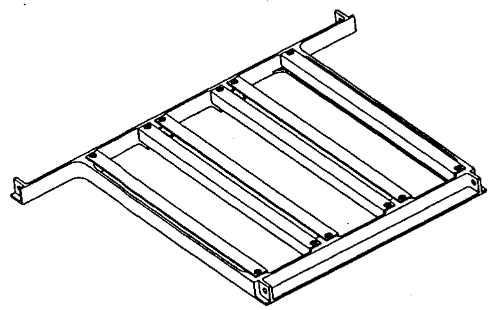

ASSEMBLED VIEW

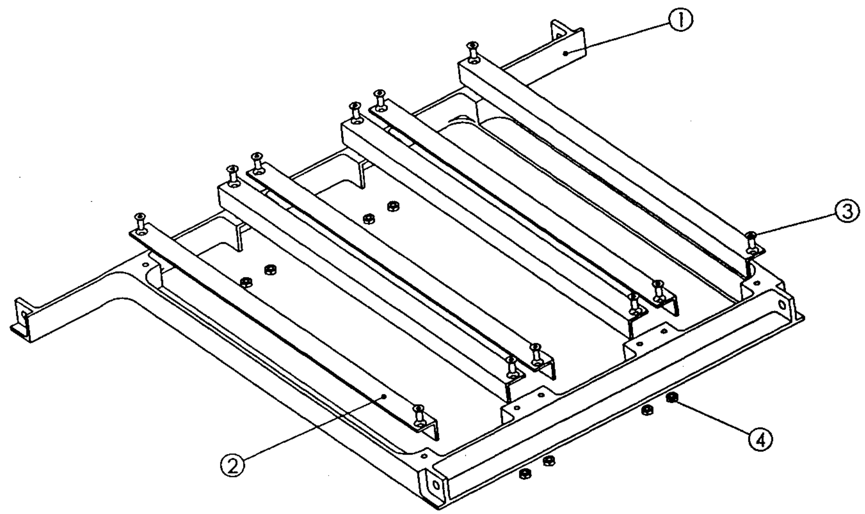

SolidWorks Educational License
Instructional Use Only

DIMENSIONS ARE IN mm
TOLERANCES:
ANGULAR:
MACH ± 0.5°
BEND ± 1°
ONE PLACE DECIMAL ± .1
TWO PLACE DECIMAL ± .03

	NAME	DATE
DRAWN	C. STEEEVS	2002/09/01
CHECKED	X	YYYY/MM/DD
ENG APPR.	X	YYYY/MM/DD

DO NOT SCALE DRAWING

MATERIAL –

FINISH –

APPLICATION ANT 1.0

COMMENTS:

McGILL UNIVERSITY
DEPT. OF MECHANICAL ENGINEERING
CENTRE FOR INTELLIGENT MACHINES
AMBULATORY ROBOTICS LAB

SIZE	DWG. NO.	REV.
A	BOTTOM BRACE ASSEMBLY	NC

WEIGHT:

SHEET 1 OF 1

ITEM	QUAN.	NAME	DESCRIPTION
1	1	TOP BRACE	AL 7075-T6
2	1	BOTTOM BRACE	AL 7075-T6
3	2	FRONT BRACE	AL 7075-T6
4	2	REAR BRACE	AL 7075-T6
5	4	HIP PLATE	AL 7075-T6
6	1	AMPLIFIER BRACE	AL EXT. ARC. GRADE
7	6	BATTERY BRACE	AL EXT. ARC. GRADE
8	1	PC/104 STACK	PC/104 FROM FACTOR COMP. - 5 BOARDS
9	4	HIP SERVO AMPLIFIER	AMC 25A8 SERVO AMP
10	1	WHEEL DRIVER BOARD	CUSTOM BOARD WITH APEX SA60 CHIPS
11	3	BATTERY PACK	BATTLEPACK - 10 SANYO HRD CELLS

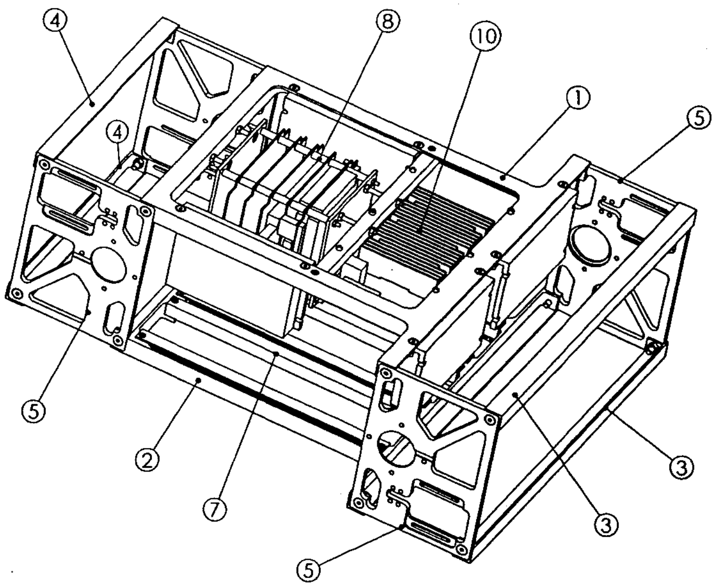

ISO VIEW
(NO BATTERIES)

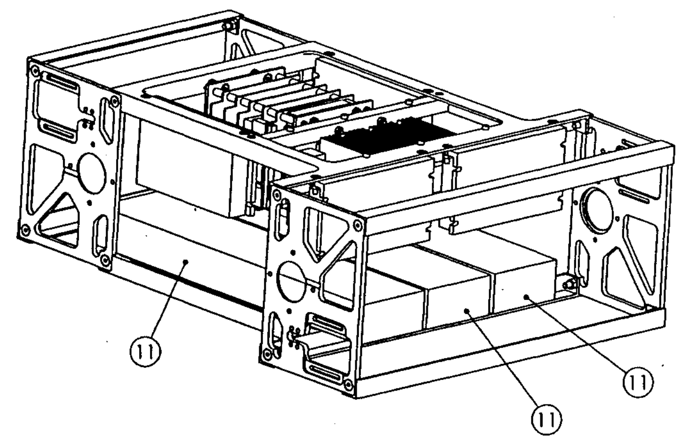

ISO VIEW
(WITH BATTERIES)

SolidWorks Educational License
Instructional Use Only

DIMENSIONS ARE IN mm
TOLERANCES:
ANGULAR:
MACH± 0.5°
BEND ± 1°
ONE PLACE DECIMAL ± .1
TWO PLACE DECIMAL ± .03

	NAME	DATE
DRAWN	C. STEEVES	2002/09/01
CHECKED	X	YYYY/MM/DD
ENG APPR.	X	YYYY/MM/DD

DO NOT SCALE DRAWING

MATERIAL
–

FINISH
–

APPLICATION
ANT 1.0

COMMENTS:

McGILL UNIVERSITY
DEPT. OF MECHANICAL ENGINEERING
CENTRE FOR INTELLIGENT MACHINES
AMBULATORY ROBOTICS LAB

SIZE A | DWG. NO. BODY ASSEMBLY | REV. NC

WEIGHT: | SHEET 1 OF 1

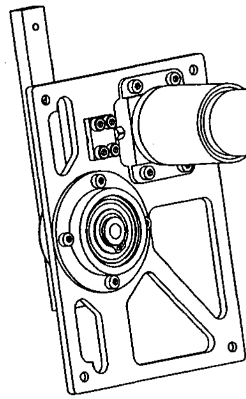

ASSEMELD VIEW
(REAR)

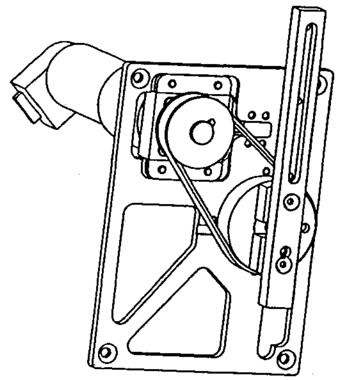

ASSEMBLED VIEW
(FRONT)

ITEM	QUAN.	NAME	DESCRIPTION
1	1	HIP MOTOR	MAXON RE 35 (118777)
2	1	HIP GEARHEAD	MAXON GP42C (203116)
3	1	HIP ENCODER	HP HEDS 5540 A11
4	1	HIP BEARING	SKF 6302-2RS1
5	1	LEG PULLEY	SDP A 6A25M032NF0908
6	1	HIP PULLEY	SDP A 6A25M022DF0908
7	1	HIP BELT	SDP A 6R25M054090
8	1	SLIDER RAIL	THK 210 LM CUSTOMIZED
9	1	HIP PLATE	AL 7075-T6
10	1	HIP SHAFT	AL 6061 T6
11	1	HIP MOTOR MOUNT	AL 6061 T6
12	1	HIP BEARING HOUSING	AL 6061 T6
13	2	MOTOR MOUNT CLAMP	ST 4140
14	1	TENSION BOLT HOUSING	AL 6061 T6
15	1	SQUARE HEAD BOLT M5 X 16	DIN 479-M5X16
16	14	SOCKET BOLT M4 X 8	DIN 912-M4X8
17	4	SOCKET BOLT M4 X 10	DIN 912-M4X10
18	1	SOCKET SET SCREW FLAT POINT M4 X 10	DIN 913 M4X10
19	1	MAGNET	HAMLIN H-33
20	1	RETAINING RING 15 MM	DIN 471 15X1.0

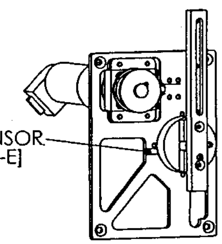

SLOT FOR HALL EFFECT SENSOR
[MICRONAS HAL 506UA-E]

ASSEMBLED VIEW
(FRONT - NO BELT)

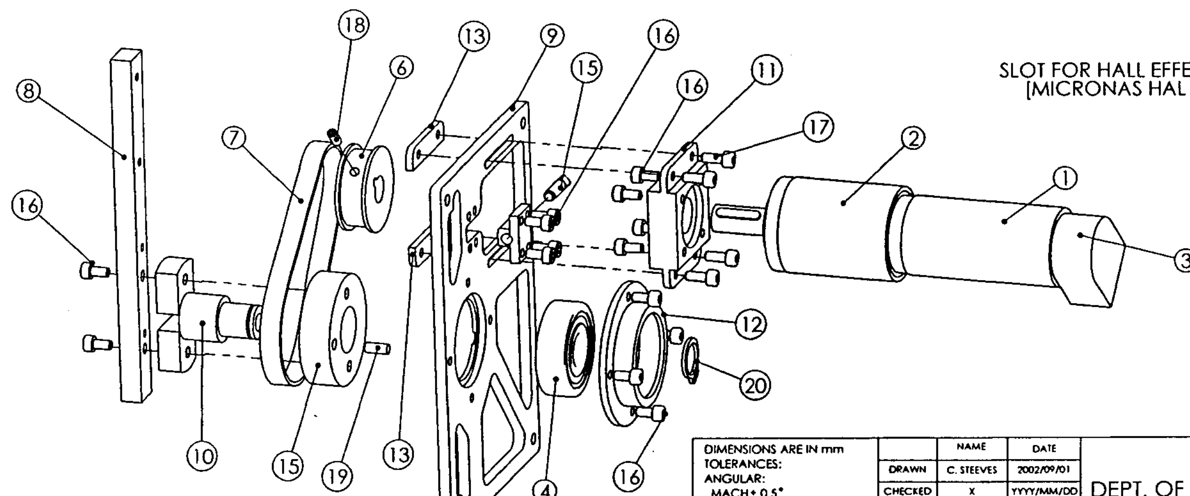

SolidWorks Educational License
Instructional Use Only

DIMENSIONS ARE IN mm
TOLERANCES:
ANGULAR:
MACH ± 0.5°
BEND ± 1°
ONE PLACE DECIMAL ± .1
TWO PLACE DECIMAL ± .03

	NAME	DATE
DRAWN	C. STEEVES	2002/09/01
CHECKED	X	YYYY/MM/DD
ENG APPR.	X	YYYY/MM/DD

DO NOT SCALE DRAWING

MATERIAL –

FINISH –

APPLICATION ANT 1.0

COMMENTS:

McGILL UNIVERSITY
DEPT. OF MECHANICAL ENGINEERING
CENTRE FOR INTELLIGENT MACHINES
AMBULATORY ROBOTICS LAB

SIZE A | DWG. NO. HIP ASSEMBLY | REV. NC

WEIGHT: | SHEET 1 OF 1

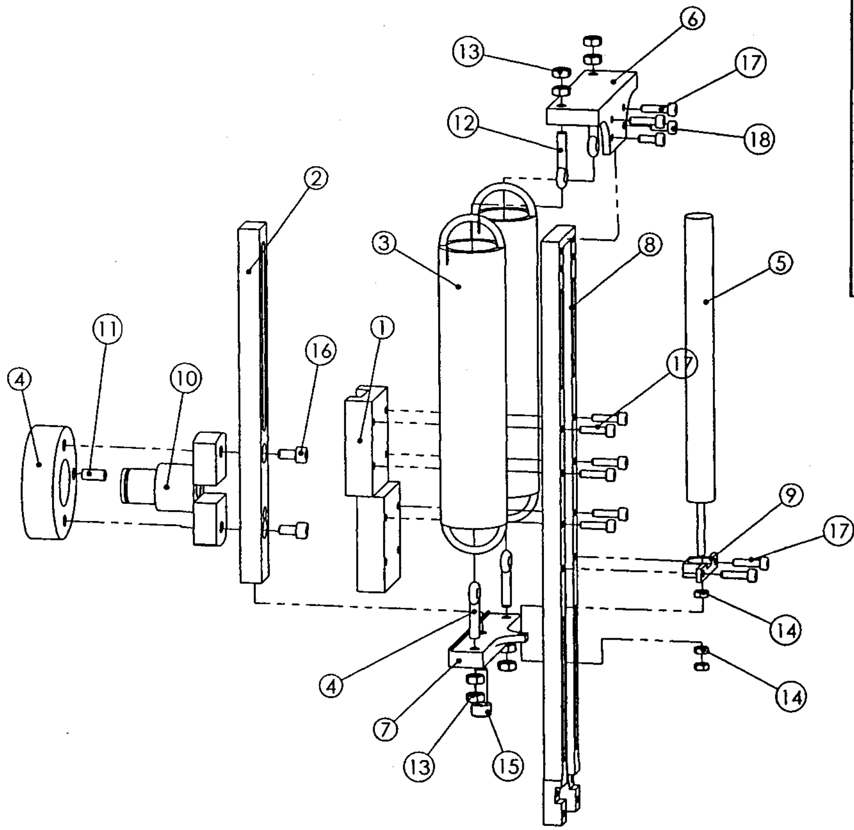

ITEM	QUAN.	NAME	DESCRIPTION
1	2	SLIDER BLOCK	THK 2 RSR15 VM SS
2	1	SLIDER RAIL	THK 210 LM CUSTOMIZED
3	2	SPRING	SPEC E1125-125-5000
4	1	LEG PULLEY	SDP A 6A25M032NF0908
5	1	POTENTIOMETER	MIDORI LP-100FP 5KOHM
6	1	SPRING MOUNT	AL 6061 T6
7	1	SLIDER STOPPER	AL 6061 T6
8	1	LEG	AL 7075-T6
9	1	POT MOUNT	AL 6061 T6
10	1	HIP SHAFT	AL 6061 T6
11	1	MAGNET	HAMLIN H-33
12	4	EYE BOLT M4 X 20 X 6	METRICAN 17420.042.006
13	8	NUT M4	ISO 4032 M4-D-N
14	3	NUT M3	ISO 4032 M3-D-N
15	1	SOCKET BOLT M5 X 16	DIN 912-M5X16
16	2	SOCKET BOLT M5 X 8	DIN 912-M5X8
17	10	SOCKET BOLT M3 X 12	DIN 912-M3X12
18	2	SOCKET BOLT M3 X 8	DIN 912-M3X8

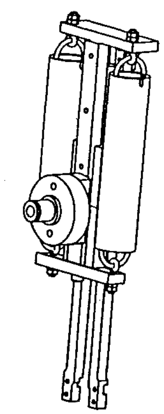

ASSEMBLED VIEW
(REAR)

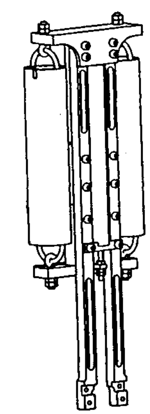

ASSEMBLED VIEW
(FRONT)

SolidWorks Educational License
Instructional Use Only

DIMENSIONS ARE IN mm
TOLERANCES:
ANGULAR:
MACH ± 0.5°
BEND ± 1°
ONE PLACE DECIMAL ± .1
TWO PLACE DECIMAL ± .03

	NAME	DATE
DRAWN	C. STEEVES	2002/09/01
CHECKED	X	YYYY/MM/DD
ENG APPR.	X	YYYY/MM/DD

DO NOT SCALE DRAWING

MATERIAL —
FINISH —
APPLICATION ANT 1.0
COMMENTS:

McGILL UNIVERSITY
DEPT. OF MECHANICAL ENGINEERING
CENTRE FOR INTELLIGENT MACHINES
AMBULATORY ROBOTICS LAB

SIZE A | DWG. NO. UPPER LEG ASSEMBLY | REV. NC

WEIGHT: | SHEET 1 OF 1

ITEM	QUAN.	NAME	DESCRIPTION
1	1	WHEEL MOTOR	MAXON RE 25 (118751)
2	1	WHEEL GEARHEAD	MAXON GP32C (233147)
3	1	WHEEL ENCODER	HP HEDS 5540 A02
4	1	LOWER LEG	AL 7075-T6
5	1	WHEEL MOTOR MOUNT	AL 6061 T6
6	1	LARGE BEVEL GEAR	SDP A 1C 3MYK10045
7	1	SMALL BEVEL GEAR	SDP A 1C 3MYK10015
8	1	SHOULDER BOLT (M5)6 X 4	ISO 7379 H8-12.9
9	1	FLANGE NUT M5	DIN 6923-M6-N
10	2	WHEEL BEARING	NSK 686DD
11	1	WHEEL HUB	AL 6061 T6
12	1	WHEEL TREAD	RUBBER
13	1	WHEEL SPACER DIA. 8 X 7	AL 6061 T6
14	1	WHEEL SPACER DIA. 8 X 10	AL 6061 T6
15	1	WHEEL SPACER DIA. 13 X 10	AL 6061 T6
16	1	WHEEL SPACER DIA. 8 X 4	AL 6061 T6
17	4	SOCKET BOLT M3 X 6 THIN	DIN 7984-M3X6
18	4	SOCKET BOLT M3 X 16	DIN 912-M3X16
19	4	SOCKET BOLT M3 X 8	DIN 912-M3X8
20	1	SOCKET SET SCREW DOG POINT M4 X 6	DIN 915-M4X6

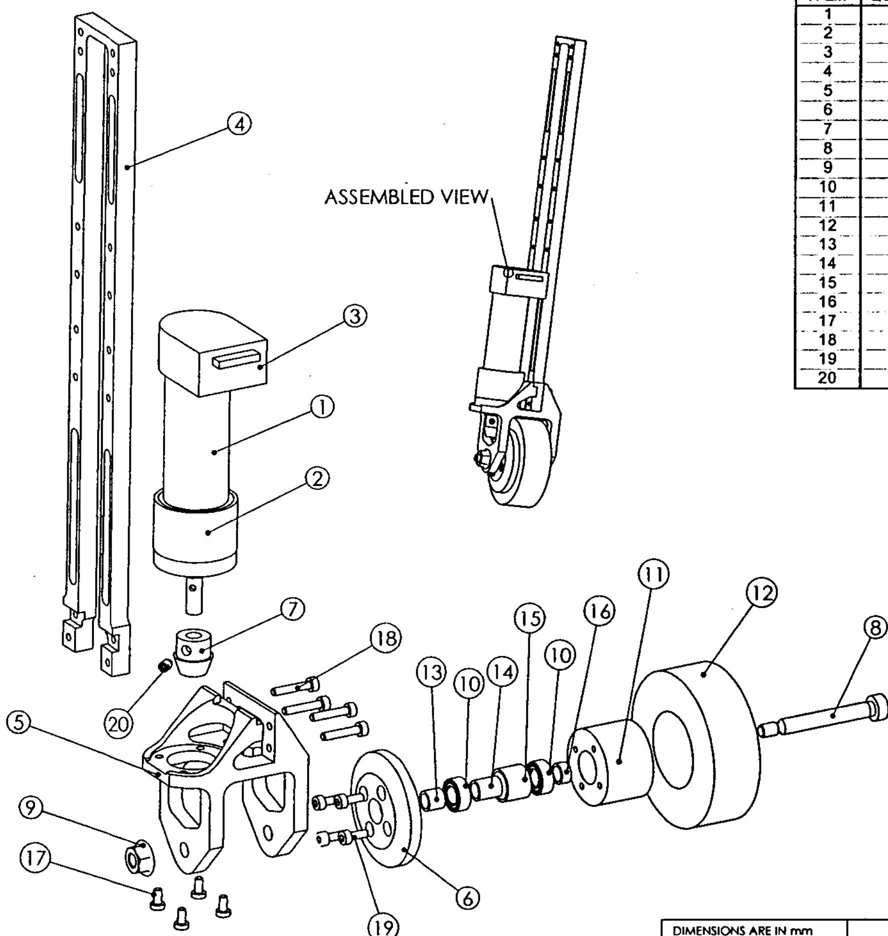

SolidWorks Educational License
Instructional Use Only

DIMENSIONS ARE IN mm
TOLERANCES:
ANGULAR:
MACH ± 0.5°
BEND ± 1°
ONE PLACE DECIMAL ± .1
TWO PLACE DECIMAL ± .03

	NAME	DATE
DRAWN	C. STEEVES	2002/09/01
CHECKED	X	YYYY/MM/DD
ENG APPR.	X	YYYY/MM/DD

DO NOT SCALE DRAWING

MATERIAL: --
FINISH: --
APPLICATION: ANT 1.0
COMMENTS:

McGILL UNIVERSITY
DEPT. OF MECHANICAL ENGINEERING
CENTRE FOR INTELLIGENT MACHINES
AMBULATORY ROBOTICS LAB

SIZE: A
DWG. NO.: LOWER LEG ASSEMBLY
REV.: NC
WEIGHT:
SHEET 1 OF 1

ITEM	QUAN.	NAME	DESCRIPTION
1	1	BODY	SEE BODY ASSEMBLY
2	1	FRONT RIGHT LEG ASSEMBLY	SEE UPPER AND LOWER LEG ASSEMBLY
3	1	FRONT LEFT LEG ASSEMBLY	SEE UPPER AND LOWER LEG ASSEMBLY
4	1	REAR RIGHT LEG ASSEMBLY	SEE UPPER AND LOWER LEG ASSEMBLY
5	1	REAR LEFT LEG ASSEMBLY	SEE UPPER AND LOWER LEG ASSEMBLY
6	4	HIP SHAFT	AL 6061 T6
7	4	HIP BELT	SDP A 6R25M054090
8	4	HIP BEARING	SKF 6302-2RS1
9	4	HIP BEARING HOUSING	AL 6061 T6
10	4	RETAINING RING 15 MM	DIN 471 15X1.0
11	1	LEG PULLEY	SDP A 6A25M032NF0908
12	1	HIP PULLEY	SDP A 6A25M022DF0908

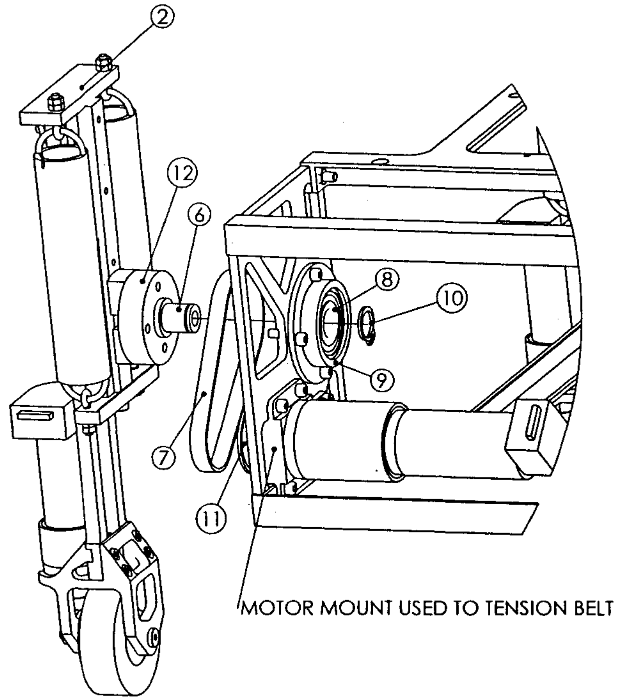

DETAIL A (1 : 3)

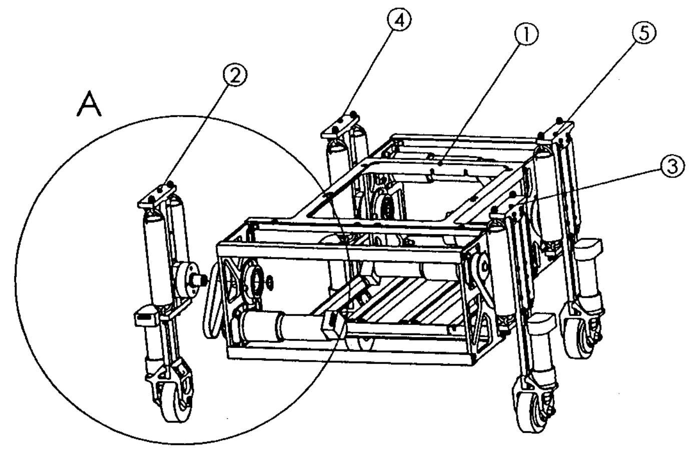

SolidWorks Educational License
Instructional Use Only

DIMENSIONS ARE IN mm
TOLERANCES:
ANGULAR:
MACH ± 0.5°
BEND ± 1°
ONE PLACE DECIMAL ± .1
TWO PLACE DECIMAL ± .03

	NAME	DATE
DRAWN	C. STEEVES	2002/09/01
CHECKED	X	YYYY/MM/DD
ENG APPR.	X	YYYY/MM/DD

DO NOT SCALE DRAWING

MATERIAL —
FINISH —
APPLICATION ANT 1.0
COMMENTS:

McGILL UNIVERSITY
DEPT. OF MECHANICAL ENGINEERING
CENTRE FOR INTELLIGENT MACHINES
AMBULATORY ROBOTICS LAB

SIZE	DWG. NO.	REV.
A	LEG TO HIP ASSEMBLY	NC

WEIGHT:
SHEET 1 OF 1

Appendix C

Bill of Materials and Cost Breakdown for Testbed

NOTES
All prices are in CAN funds (exchange rate: 1 US$ = 1.59 CAN$).
Prices do not include taxes, shipping, duty or brokerage fees.

BILL OF MATERIALS AND COST BREAKDOWN								
PART NAME	QTY.	DESCRIPTION	MASS (g)		MATERIAL COSTS		MACHINING COSTS	
			UNIT	TOTAL	UNIT	TOTAL	UNIT	TOTAL
PC/104 POWER SUPPLY	1	RTD EPWR104HR-25/25W	140	140	$469.05	$469.05	N/A	N/A
PC/104 QUAD. DECODER	1	MICROCOMPUTER SYSTEMS MSI-P400	48	48	$802.95	$802.95	N/A	N/A
PC/104 COMPUTER BOARD	1	LIPPERT COOLROAD RUNNER II	150	150	$850.65	$850.65	N/A	N/A
PC/104 CUSTOM I/O BOARD	1	CUSTOM INTERFACE CARD	90	90	$715.00	$715.00	N/A	N/A
PC/104 PCMCIA ADAPTER BOARD	1	VERSALOGIC PCM-3115	95	95	$300.51	$300.51	N/A	N/A
PCMCIA WIRELESS ETHERNET CARD	1	ORINOCO GOLD 11 MBITS/S	40	40	$126.85	$126.85	N/A	N/A
256 MB FLASH DISK	1	KINGSTON CF/256	5	5	$170.76	$170.76	N/A	N/A
256 MB SDRAM	1	LIPPERT S-SDRAM-256MB	0.5	0.5	$160.59	$160.59	N/A	N/A
SPRING	8	SPEC E1125-125-5000 M	136	544	$13.91	$111.28	N/A	N/A
HIP SERVO AMPLIFIER	4	AMC 25A8 SERVO AMP	270	1080	$280.00	$1,120.00	N/A	N/A
WHEEL DRIVER BOARD	1	CUSTOM BOARD WITH APEX SA60 CHIPS	440	440	$697.39	$697.39	N/A	N/A
BATTERY PACK	3	BATTLEPACK - 10 SANYO HRD CELLS	1890	5670	$267.12	$801.36	N/A	N/A
HIP MOTOR	4	MAXON RE 35 (118777)	340	1360	$268.07	$1,072.28	N/A	N/A
HIP GEARHEAD	4	MAXON GP42C (203116)	360	1440	$265.05	$1,060.20	N/A	N/A
HIP ENCODER	4	HP HEDS 5540 A11	34	136	$119.73	$478.92	N/A	N/A
WHEEL MOTOR	4	MAXON RE 25 (118751)	130	520	$315.93	$1,263.72	N/A	N/A
WHEEL GEARHEAD	4	MAXON GP32C (233147)	118	472	$273.08	$1,092.32	$13.50	$54.00
WHEEL ENCODER	4	HP HEDS 5540 A02	22	88	$144.30	$577.20	N/A	N/A
POTENTIOMETER	4	MIDORI LP-100FP 5KOHM	35	140	$211.47	$845.88	N/A	N/A
LEG	4	AL 7075-T6	90	360	**	**	$69.45	$277.80
WHEEL MOTOR MOUNT	4	AL 6061 T6	63	252	++	++	$150.45	$601.80

++ AL 6061-T6 material costs included as a whole
** AL 7075-T6 material costs included as a whole

BILL OF MATERIALS AND COST BREAKDOWN									
PART NAME	QTY.	DESCRIPTION	MASS (g)		MATERIAL COSTS		MACHINING COSTS	
			UNIT	TOTAL	UNIT	TOTAL	UNIT	TOTAL
LARGE BEVEL GEAR	4	SDP A 1C 3MYK10045	70	280	$46.68	$186.72	$51.75	$207.00
SMALL BEVEL GEAR	4	SDP A 1C 3MYK10015	12	48	$22.92	$91.68	$13.50	$54.00
HIP BEARING	4	SKF 6302-2RS1	82	328	$11.67	$46.68	N/A	N/A
WHEEL BEARING	8	NSK 686DD	27	216	$9.92	$79.36	N/A	N/A
WHEEL HUB	4	AL 6061 T6	32	128	++	++	$31.88	$127.52
WHEEL TREAD	4	RUBBER	28	112	$20.00	$80.00	N/A	N/A
WHEEL SPACER DIA. 8 X 7	4	AL 6061 T6	0.4	1.6	++	++	$8.69	$34.76
WHEEL SPACER DIA. 8 X 10	4	AL 6061 T6	0.6	2.4	++	++	$8.69	$34.76
WHEEL SPACER DIA. 13 X 10	4	AL 6061 T6	1	4	++	++	$8.69	$34.76
WHEEL SPACER DIA. 8 X 4	4	AL 6061 T6	0.25	1	++	++	$8.69	$34.76
SLIDER BLOCK	8	THK 2 RSR15 VM SS	69	552	$69.12	$552.97	N/A	N/A
SLIDER RAIL	4	THK 210 LM CUSTOMIZED	140	560	$162.00	$648.00	$37.50	$150.00
LEG PULLEY	4	SDP A 6A25M032NF0908	60	240	$20.59	$82.36	$40.50	$162.00
SPRING MOUNT	4	AL 6061 T6	41	164	++	++	$38.55	$154.20
SLIDER STOPPER	4	AL 6061 T6	23	92	++	++	$37.95	$151.80
POT MOUNT	4	AL 6061 T6	2.2	8.8	++	++	$27.90	$111.60
HIP SHAFT	4	AL 6061 T6	41	164	++	++	$56.55	$226.20
MAGNET	4	HAMLIN H-33	1.2	4.8	$3.98	$15.92	N/A	N/A
HALL EFFECT SENSOR	4	MICRONAS HAL 506UA-E	0.5	2	$1.85	$7.40	N/A	N/A
HIP PULLEY	4	SDP A 6A25M022DF0908	32	128	$16.20	$64.80	$50.63	$202.52
HIP BELT	4	SDP A 6R25M054090	8	32	$10.68	$42.72	N/A	N/A
HIP PLATE	4	AL 7075-T6	142	568	**	**	$105.00	$420.00
HIP MOTOR MOUNT	4	AL 6061 T6	48	192	++	++	$39.45	$157.80
HIP BEARING HOUSING	4	AL 6061 T6	23	92	++	++	$53.25	$213.00
MOTOR MOUNT CLAMP	8	ST 4140	9	72	++	++	$14.37	$114.96

++ AL 6061-T6 material costs included as a whole

** AL 7075-T6 material costs included as a whole

BILL OF MATERIALS AND COST BREAKDOWN								
PART NAME	QTY.	DESCRIPTION	MASS (g)		MATERIAL COSTS		MACHINING COSTS	
			UNIT	TOTAL	UNIT	TOTAL	UNIT	TOTAL
TENSION BOLT HOUSING	4	AL 6061 T6	6.5	26	++	++	$29.10	$116.40
TOP BRACE	1	AL 7075-T6	267	267	**	**	$408.00	$408.00
BOTTOM BRACE	1	AL 7075-T6	305	305	**	**	$408.00	$408.00
FRONT BRACE	2	AL 7075-T6	68	136	**	**	$70.50	$141.00
REAR BRACE	2	AL 7075-T6	46	92	**	**	$70.50	$141.00
BATTERY BRACE	6	AL EXT. ARC. GRADE	30	180	$1.95	$11.70	$24.30	$145.80
AMPLIFIER BRACE	1	AL EXT. ARC. GRADE	25	25	$1.95	$1.95	$47.40	$47.40
PC/104 STACK MOUNT 1	1	LEXAN 3 MM	50	50	$5.00	$5.00	$48.00	$48.00
PC/104 STACK MOUNT 2	1	LEXAN 3 MM	50	50	$5.00	$5.00	$48.00	$48.00
GYROSCOPE	1	MURATA GYROSTAR ENC-03JA	1	1	$11.30	$11.30	N/A	N/A
M3 THREADED ROD	4	DIN 975 M3 130 MM	9.7	38.8	$1.00	$4.00	N/A	N/A
PLASTIC STAND-OFF/SPACER	28	RICHCO R908-10	0.1	2.8	$0.10	$2.80	N/A	N/A
SHOULDER BOLT (M5)6 X 4	4	ISO 7379 H8-12.9	12.3	49.2	$1.83	$7.32	N/A	N/A
SQUARE HEAD BOLT M5 X 16	4	DIN 479-M5X16	3.2	12.8	$1.40	$5.60	N/A	N/A
EYE BOLT M4 X 20 X 6	16	METRICAN 17420.042.006	3.4	54.4	$0.23	$3.68	N/A	N/A
RETAINING RING 15 MM	4	DIN 471 15X1.0	1.3	5.2	$0.50	$2.00	N/A	N/A
SOCKET SET SCREW DOG POINT M4 X 6	4	DIN 915-M4X6	0.4	1.6	$0.19	$0.76	N/A	N/A
SOCKET SET SCREW FLAT POINT M4 X 10	4	DIN 913 M4X10	0.6	2.4	$0.36	$1.44	N/A	N/A
SOCKET BOLT M3 X 6 THIN	16	DIN 7984-M3X6	0.6	9.6	$0.28	$4.48	N/A	N/A
SOCKET BOLT M3 X 8	32	DIN 912-M3X8	0.9	28.8	$0.14	$4.48	N/A	N/A
SOCKET BOLT M3 X 12	40	DIN 912-M3X12	1.1	44	$0.16	$6.40	N/A	N/A
SOCKET BOLT M3 X 16	16	DIN 912-M3X16	1.3	20.8	$0.18	$2.88	N/A	N/A
SOCKET BOLT M3 X 30	6	DIN 912-M3X30	3.2	19.2	$0.13	$0.78	N/A	N/A
SOCKET BOLT M4 X 8	56	DIN 912-M4X8	1.8	100.8	$0.14	$7.84	N/A	N/A
SOCKET BOLT M4 X 10	16	DIN 912-M4X10	2	32	$0.12	$1.92	N/A	N/A

++ AL 6061-T6 material costs included as a whole

** AL 7075-T6 material costs included as a whole

BILL OF MATERIALS AND COST BREAKDOWN								
PART NAME	QTY.	DESCRIPTION	MASS (g)		MATERIAL COSTS		MACHINING COSTS	
			UNIT	TOTAL	UNIT	TOTAL	UNIT	TOTAL
SOCKET BOLT M5 X 16	4	DIN 912-M5X16	4.3	17.2	$0.07	$0.28	N/A	N/A
SOCKET BOLT M3 X 8 COUNTER SINK	12	DIN 7991-M3X8	0.5	6	$0.12	$1.44	N/A	N/A
SOCKET BOLT M3 X 10 COUNTER SINK	2	DIN 7991-M3X10	0.6	1.2	$0.15	$0.30	N/A	N/A
SOCKET BOLT M4 X 16 COUNTER SINK	8	DIN 7991-M4X16	1.8	14.4	$0.14	$1.12	N/A	N/A
SOCKET BOLT M4 X 40 COUNTER SINK	4	DIN 7991-M4X40	4.1	16.4	$0.25	$1.00	N/A	N/A
SOCKET BOLT M5 X 16 COUNTER SINK	16	DIN 7991-M5X16	2.8	44.8	$0.19	$3.04	N/A	N/A
NUT M3	12	ISO 4032 M3-D-N	0.4	4.8	$0.05	$0.60	N/A	N/A
NUT M4	32	ISO 4032 M4-D-N	0.8	25.6	$0.05	$1.60	N/A	N/A
NYLOC NUT M3	36	DIN 985 M3	0.4	14.4	$0.10	$3.60	N/A	N/A
NYLOC NUT M4	20	DIN 985 M4	1	20	$0.10	$2.00	N/A	N/A
NYLOC NUT M5	16	DIN 985 M5	1.5	24	$0.10	$1.60	N/A	N/A
FLANGE NUT M5	4	DIN 6923-M6-N	1.5	6	$0.05	$0.20	N/A	N/A
SKIN	1	LEXAN SHEET 1/32" THICK	N/A	150	N/A	$20.00	N/A	N/A
ALUMINUM 6061-T6 STOCK ++	1	STOCK USED FOR MACHINING	N/A	N/A	N/A	$130.00	N/A	N/A
ALUMINUM 7075-T6 STOCK **	1	STOCK USED FOR MACHINING	N/A	N/A	N/A	$709.00	N/A	N/A
VELCRO STRAPS	6	SPAENAUR 888-240	5	30	$0.50	$3.00	N/A	N/A
VELCRO LOOPS	6	SPAENAUR 122-725	1	5	$0.25	$1.50	N/A	N/A
RUBBER WHEATHER STRIPS	6	CANADIAN TIRE 1/2" STRIPS	N/A	5	$2.00	$10.00	N/A	N/A
ANODIZING COSTS	1	7075-T6 CORROSION PROTECTION	N/A	N/A	N/A	$90.00	N/A	N/A
WIRING AND CABLING	1	ASSORTED WIRING AND CABLING	N/A	1200	N/A	$300.00	N/A	N/A
TOTAL				20202		$15,987		$5,029

++ AL 6061-T6 material costs included as a whole
** AL 7075-T6 material costs included as a whole

Appendix D

Manufacture's Data Sheets

RE 35 ∅35 mm, Graphite Brushes, 90 Watt

maxon DC motor

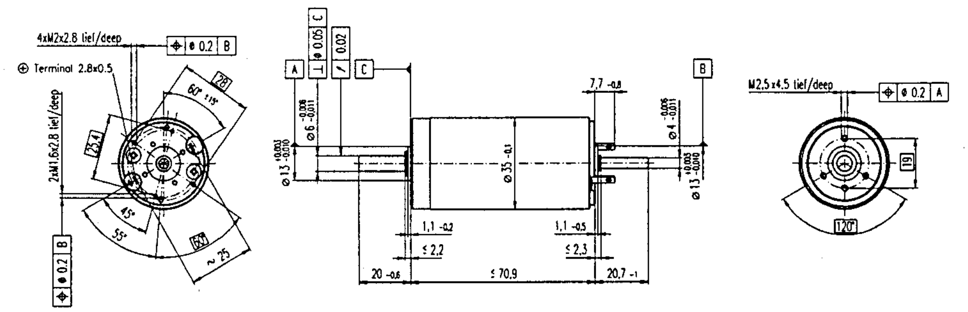

Stock program
Standard program
Special program (on request!)

Order Number

Motor Data		118776	118777	118778	118779	118780	118781	118782	118783	118784	118785	118786	118787	118788	118789	118790
1 Assigned power rating	W	90	90	90	90	90	90	90	90	90	90	90	90	90	90	90
2 Nominal voltage	Volt	15.0	30.0	42.0	48.0	48.0	48.0	48.0	48.0	48.0	48.0	48.0	48.0	48.0	48.0	48.0
3 No load speed	rpm	7070	7220	7530	7270	6650	5970	4750	3810	3140	2570	2100	1620	1290	1060	856
4 Stall torque	mNm	872	949	1070	966	878	766	613	493	394	320	253	194	155	125	99.5
5 Speed / torque gradient	rpm / mNm	8.45	7.77	7.17	7.63	7.68	7.89	7.88	7.84	8.09	8.19	8.47	8.55	8.54	8.80	8.94
6 No load current	mA	245	124	93	77	69	60	45	34	27	22	17	13	10	8	7
7 Starting current	A	44.9	24.4	20.3	15.5	12.9	10.1	6.43	4.16	2.74	1.83	1.18	0.704	0.448	0.298	0.193
8 Terminal resistance	Ohm	0.334	1.23	2.07	3.09	3.72	4.75	7.46	11.5	17.5	26.2	40.5	68.2	107	161	248
9 Max. permissible speed	rpm	8200	8200	8200	8200	8200	8200	8200	8200	8200	8200	8200	8200	8200	8200	8200
10 Max. continuous current	A	4.00	2.74	2.15	1.78	1.63	1.45	1.17	0.944	0.768	0.630	0.508	0.392	0.313	0.256	0.206
11 Max. continuous torque	mNm	77.7	107	113	111	111	110	111	112	111	110	109	108	108	107	106
12 Max. power output at nominal voltage	W	152	175	206	181	150	118	75.0	48.4	31.8	21.2	13.7	8.07	5.10	3.36	2.15
13 Max. efficiency	%	81	84	86	85	85	84	83	82	80	79	77	74	72	69	66
14 Torque constant	mNm / A	19.4	38.9	52.5	62.2	68.0	75.8	95.2	119	144	175	214	276	346	418	515
15 Speed constant	rpm / V	491	246	182	154	140	126	100.0	80.6	66.4	54.6	44.7	34.6	27.6	22.9	18.5
16 Mechanical time constant	ms	6	5	5	5	5	5	5	5	5	5	5	5	5	5	5
17 Rotor inertia	gcm²	65.5	65.5	69.6	65.0	64.5	62.7	62.8	62.8	60.7	59.9	57.9	57.2	57.2	55.5	54.5
18 Terminal inductance	mH	0.09	0.34	0.62	0.87	1.04	1.29	2.04	3.16	4.65	6.89	10.30	17.10	26.90	39.30	59.70
19 Thermal resistance housing-ambient	K / W	6.2	6.2	6.2	6.2	6.2	6.2	6.2	6.2	6.2	6.2	6.2	6.2	6.2	6.2	6.2
20 Thermal resistance rotor-housing	K / W	2.0	2.0	2.0	2.0	2.0	2.0	2.0	2.0	2.0	2.0	2.0	2.0	2.0	2.0	2.0
21 Thermal time constant winding	s	27	27	29	27	27	26	26	26	25	25	24	24	24	23	23

Specifications

- Axial play 0.05 - 0.15 mm
- Max. ball bearing loads
  axial (dynamic)
  not preloaded 5.6 N
  preloaded 2.4 N
  radial (5 mm from flange) 28 N
  Press-fit force (static) 110 N
  (static, shaft supported) 1200 N
- Radial play ball bearing 0.025 mm
- Ambient temperature range -20 / +100°C
- Max. rotor temperature +155°C
- Number of commutator segments 13
- Weight of motor 340 g
- Values listed in the table are nominal.
  For applicable tolerances (see page 43).
  For additional details please use the maxon selection program on the enclosed CD-Rom.

- Option: Hollow shaft as special design.

Operating Range

Comments

Details on page 49

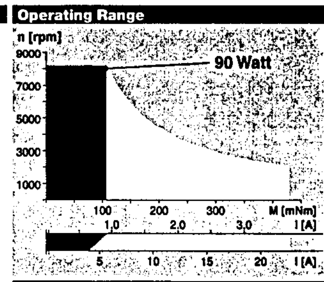

Recommended operating range

Continuous operation
In observation of above listed thermal resistances (lines 19 and 20) the maximum permissible rotor temperature will be reached during continuous operation at 25°C ambient.
= Thermal limit.

Short term operation
The motor may be briefly overloaded (recurring).

118783 Motor with high resistance winding
118776 Motor with low resistance winding

maxon Modular System

Planetary Gearhead
∅32 mm
0.75 - 4.5 Nm
Details page 184

Planetary Gearhead
∅32 mm
1.0 - 6.0 Nm
Details page 187

Planetary Gearhead
∅42 mm
3 - 15 Nm
Details page 191

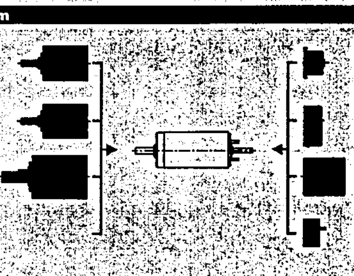

DC-Tacho
∅22 mm
0.52 V
Details page 213

Digital Encoder
HP HED_ 55_
500 CPT, 3 channels
Details page 205 / 207

Brake
∅40 mm
24 VDC, 0.4 Nm
Details page 236

Digital MR Encoder
256 - 1024 CPT,
3 channels
Details page 202

April 2002 edition / subject to change

Planetary Gearhead GP 42 C ∅42 mm, 3 - 15 Nm

Ceramicversion

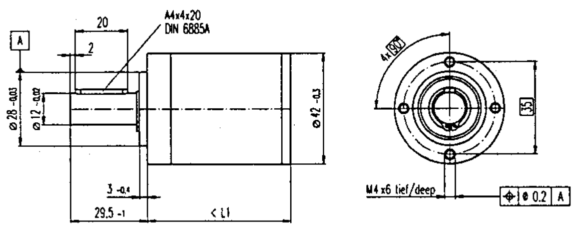

Technical Data	
Planetary Gearhead	straight teeth
Output shaft	stainless steel
Bearing at output	ball bearings
Radial play, 12 mm from flange	preloaded
Axial play	preloaded
Max. permissible axial load	150 N
Max. permissible force for press fits	300 N
Recommended input speed	< 8000 rpm
Recommended temperature range	-20 / +100°C

Number of stages	1	2	3	4
Max. perm. radial load 12 mm from flange	120 N	150 N	150 N	150 N

Stock program
Standard program
Special program (on request!)

Gearhead Data								
Order Number		203113	203115	203120	203125	203128	203134	203139
1 Reduction		3.5 : 1	12 : 1	43 : 1	91 : 1	150 : 1	319 : 1	546 : 1
2 Reduction absolute		7/2	49/4	343/8	91	2401/16	637/2	546
3 Mass inertia	gcm²	14	15	15	15	15	15	14
Order Number		203114	203116	203121	203126	203130	203135	203140
1 Reduction		4.3 : 1	15 : 1	53 : 1	113 : 1	186 : 1	353 :1	676 : 1
2 Reduction absolute		13/3	91/6	637/12	338/3	4459/24	28561/81	676
3 Mass inertia	gcm²	9.1	15	15	9.4	15	9.4	9.1
Order Number			203117	203122	203127	203131	203136	203141
1 Reduction			19 : 1	66 : 1	126 : 1	230 : 1	394 : 1	756 : 1
2 Reduction absolute			169/9	1183/18	126	8281/36	1183/3	756
3 Mass inertia	gcm²		9.4	15	14	15	15	14
Order Number			203118	203123	203129	203132	203137	203142
1 Reduction			21 : 1	74 : 1	156 : 1	257 : 1	441 : 1	936 : 1
2 Reduction absolute			21	147/2	156	1029/4	441	936
3 Mass inertia	gcm²		14	15	9.1	15	14	9.1
Order Number			203119	203124		203133	203138	
1 Reduction			26 : 1	81 : 1		285 : 1	488 : 1	
2 Reduction absolute			26	2187/27		15379/54	4394/9	
3 Mass inertia	gcm²		9.1	9.4		15	9.4	
4 Number of stages		1	2	3	3	4	4	4
5 Max. continuous torque at gear output	Nm	3.0	7.5	15	15	15	15	15
6 Intermittently permissible torque at gear output	Nm	4.5	11.3	22.5	22.5	22.5	22.5	22.5
7 Max. efficiency	%	90	81	72	72	64	64	64
8 Weight	g	260	360	460	460	560	560	560
9 Average backlash no load	°	0.3	0.4	0.5	0.5	0.5	0.5	0.5
10 Gearhead length L1	mm	41.0	55.5	70.0	70.0	84.5	84.5	84.5

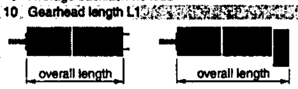

Combination:

+ Motor	Page	+ Tacho	Page	+ Brake	Page	Overall length [mm]						
RE 35, 90 W	76					112.0	126.5	141.0	141.0	155.5	155.5	155.5
RE 35, 90 W	76	MR Encoder	202			123.4	137.9	152.4	152.4	166.9	166.9	166.9
RE 35, 90 W	76	DC-Tacho 22	213			130.1	144.6	159.1	159.1	173.6	173.6	173.6
RE 35, 90 W	76	Digital Encoder HED_ 55__	205/207			133.0	147.5	162.0	162.0	176.5	176.5	176.5
RE 35, 90 W	76			Brake 40	236	148.1	162.6	177.1	177.1	191.6	191.6	191.6
RE 36, 70 W	77					112.3	126.8	141.3	141.3	155.8	155.8	155.8
RE 36, 70 W	77	MR Encoder	202			123.7	138.2	152.7	152.7	167.2	167.2	167.2
RE 36, 70 W	77	DC-Tacho 22	213			130.4	144.9	159.4	159.4	173.9	173.9	173.9
RE 36, 70 W	77	Digital Encoder HED_ 55__	205/207			132.3	146.8	161.3	161.3	175.8	175.8	175.8
RE 40, 150 W	78					112.1	126.6	141.1	141.1	155.6	155.6	155.6
RE 40, 150 W	78	MR Encoder	202			123.5	138.0	152.5	152.5	167.0	167.0	167.0
RE 40, 150 W	78	Digital Encoder HED_ 55__	205/207			132.8	147.3	161.8	161.8	176.3	176.3	176.3
RE 40, 150 W	78			Brake 40	236	148.2	162.7	177.2	177.2	191.7	191.7	191.7
RE 40, 150 W	78	Digital Encoder HED_ 55__	205/207	Brake 40	236	165.3	179.8	194.3	194.3	208.8	208.8	208.8
RE 40, 150 W	78	Digital Encoder HEDL 9140	209			166.2	180.7	195.2	195.2	209.7	209.7	209.7
RE 40, 150 W	78			Brake 28	237	156.2	170.7	185.2	185.2	199.7	199.7	199.7
RE 40, 150 W	78	Digital Encoder HEDL 9140	209	Brake 28	237	176.3	190.8	205.3	205.3	219.8	219.8	219.8
EC 40, 120 W	153					111.1	125.6	140.1	140.1	154.6	154.6	154.6
EC 40, 120 W	153	Digital Encoder HED_ 55__	206/208			129.5	144.0	158.5	158.5	173.0	173.0	173.0
EC 40, 120 W	153	Resolver 26	216			137.7	152.2	166.7	166.7	181.2	181.2	181.2
EC 40, 120 W	153			Brake 40	236	144.6	159.1	173.6	173.6	188.1	188.1	188.1
EC 45, 150 W	154					152.3	166.8	181.3	181.3	195.8	195.8	195.8
EC 45, 150 W	154	Digital Encoder HEDL 9140	209			167.9	182.4	196.9	196.9	211.4	211.4	211.4
EC 45, 150 W	154	Digital Encoder HEDL 9140	209	Brake 28	237	176.7	191.2	205.7	205.7	220.2	220.2	220.2
EC 45, 150 W	154	Resolver 26	216			152.3	166.8	181.3	181.3	195.8	195.8	195.8
EC 45, 150 W	154			Brake 28	237	167.9	182.4	196.9	196.9	211.4	211.4	211.4
EC 45, 250 W	155					185.1	199.6	214.1	214.1	228.6	228.6	228.6
EC 45, 250 W	155	Digital Encoder HEDL 9140	209			200.7	215.2	229.7	229.7	244.2	244.2	244.2
EC 45, 250 W	155	Digital Encoder HEDL 9140	209	Brake 28	237	209.5	224.0	238.5	238.5	253.0	253.0	253.0
EC 45, 250 W	155	Resolver 26	216			185.1	199.6	214.1	214.1	228.6	228.6	228.6
EC 45, 250 W	155			Brake 28	237	200.7	215.2	229.7	229.7	244.2	244.2	244.2

maxon DC motor

RE 25 Ø25 mm, Graphite Brushes, 20 Watt

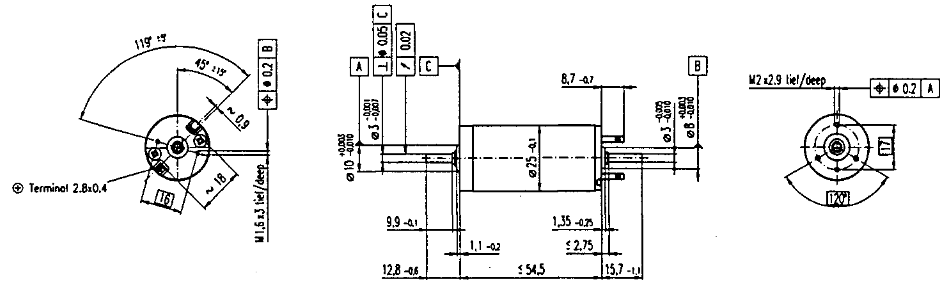

Stock program
Standard program
Special program (on request!)

			Order Number								
	Motor Data		118749	118750	118751	118752	118753	118754	118755	118756	118757
1	Assigned power rating	W	20	20	20	20	20	20	20	20	20
2	Nominal voltage	Volt	9.0	15.0	18.0	24.0	30.0	42.0	48.0	48.0	48.0
3	No load speed	rpm	10100	9760	10300	9660	9970	11200	10500	8320	5100
4	Stall torque	mNm	229	222	218	240	246	280	261	207	127
5	Speed/torque gradient	rpm/mNm	47.6	45.7	49.0	41.2	41.3	40.6	40.5	40.6	40.6
6	No load current	mA	111	62	55	37	31	26	20	15	9
7	Starting current	mA	29100	15700	13500	10300	8720	7940	6030	3810	1440
8	Terminal resistance	Ohm	0.309	0.953	1.33	2.32	3.44	5.29	7.96	12.6	33.4
9	Max. permissible speed	rpm	11000	11000	11000	11000	11000	11000	11000	11000	11000
10	Max. continuous current	mA	1500	1500	1500	1230	1030	841	695	560	350
11	Max. continuous torque	mNm	11.8	21.2	24.2	28.4	29.0	29.7	30.1	30.5	31.0
12	Max. power output at nominal voltage	mW	52800	52900	55600	58400	62200	80400	70200	44400	16800
13	Max. efficiency	%	77	82	83	85	86	87	87	87	84
14	Torque constant	mNm/A	7.88	14.1	16.1	23.2	28.2	35.3	43.3	54.4	88.7
15	Speed constant	rpm/V	1210	677	592	412	338	271	220	175	108
16	Mechanical time constant	ms	6	5	5	5	4	4	4	4	4
17	Rotor inertia	gcm²	11.3	10.00	9.11	10.3	10.1	10.1	10.00	9.96	9.91
18	Terminal inductance	mH	0.03	0.09	0.12	0.24	0.35	0.55	0.83	1.31	3.48
19	Thermal resistance housing-ambient	K/W	14	14	14	14	14	14	14	14	14
20	Thermal resistance rotor-housing	K/W	3.1	3.1	3.1	3.1	3.1	3.1	3.1	3.1	3.1
21	Thermal time constant winding	s	13	11	10	12	12	12	12	11	11

Specifications

- Axial play 0.05 - 0.15 mm
- Max. ball bearing loads
  axial (dynamic)
  not preloaded 3.2 N
  preloaded 3.2 N
  radial (5 mm from flange) 16 N
  Press-fit force (static) 64 N
  (static, shaft supported) 270 N
- Radial play ball bearings 0.025 mm
- Ambient temperature range -20/+100°C
- Max. rotor temperature +125°C
- Number of commutator segments 11
- Weight of motor 130 g
- Values listed in the table are nominal.
  For applicable tolerances (see page 43) and additional details please request out of the maxon selection program on the settled CD-Rom.

Operating Range

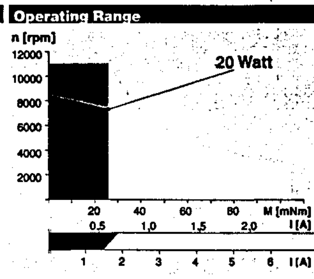

118755 Motor with high resistance winding
118751 Motor with low resistance winding

Comments

Details on page 49

Recommended operating range

Continuous operation
In observation of above listed thermal resistances (lines 19 and 20) the maximum permissible rotor temperature will be reached during continuous operation at 25°C ambient.
= Thermal limit.

Short term operation
The motor may be briefly overloaded (recurring).

maxon Modular System

Planetary Gearhead
Ø26 mm
0.2-1.8 Nm
Details page 184

Planetary Gearhead
Ø26 mm
0.5-2.0 Nm
Details page 185

Planetary Gearhead
Ø32 mm
0.75-6.0 Nm
Details page 187/190

Planetary Gearhead
Ø32 mm
0.4-2.0 Nm
Details page 193

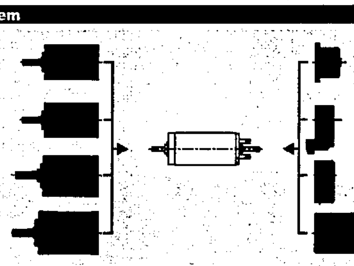

DC-Tacho
Ø22 mm
0.52 V
Details page 200

Digital Encoder
22 mm
100 CPT, 2 channels
Details page 202

Digital Encoder
HP HED_ 55__
500 CPT, 3 channels
Details page 204/206

Brake
Ø40 mm
24 VDC, 0.4 Nm
Details page 232

April 2001 edition / subject to change

Planetary Gearhead GP 32 C ∅32 mm, 1.0 - 6.0 Nm

Ceramicversion

maxon gear

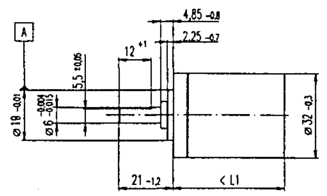

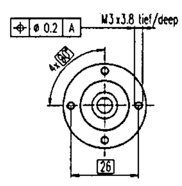

Technical Data

Planetary Gearhead	straight teeth
Output shaft	stainless steel*
Bearing at output	ball bearings
Radial play, 5 mm from flange	max. 0.14 mm
Axial play	max. 0.4 mm
Max. perm. radial load, 12 mm from flange	140 N
Max. permissible axial load	120 N
Max. permissible force for press fits	120 N
Recommended input speed	< 8000 rpm
Recommended temperature range	-15 / +80°C

*Option: shaft diameter 6 mm

Stock program
Standard program
Special program (on request!)

Order Number

Order Number		233146	233149	233154	233155	233160	233165	233170	233175	233178	233183	233188	233193
Gearhead Data													
1 Reduction		3.7 : 1	14 : 1	33 : 1	51 : 1	111 : 1	246 : 1	492 : 1	762 : 1	1181 : 1	1972 : 1	2829 : 1	4380 : 1
2 Reduction absolute		26/7	676/49	529/16	17576/343	13824/125	421824/1715	86112/175	19044/25	10123776/8575	8626176/4375	495144/175	109503/25
Order Number		233147	233150		233156	233161	233166	233171	233176	233179	233184	233189	233194
1 Reduction		4.8 : 1	18 : 1		66 : 1	123 : 1	295 : 1	531 : 1	913 : 1	1414 : 1	2189 : 1	3052 : 1	5247 : 1
2 Reduction absolute		24/5	624/35		16224/245	6877/56	101062/343	331776/625	36501/40	2425488/1715	536406/245	1907712/625	839523/160
Order Number		233148	233151		233157	233162	233167	233172	233177	233180	233185	233190	233195
1 Reduction		5.8 : 1	21 : 1		79 : 1	132 : 1	318 : 1	589 : 1	1093 : 1	1526 : 1	2362 : 1	3389 : 1	6285 : 1
2 Reduction absolute		23/4	299/14		3887/49	3312/25	389376/1225	20631/35	279841/256	9345024/6125	2066688/875	474513/140	6436343/1024
Order Number			233152		233158	233163	233168	233173		233181	233186	233191	
1 Reduction			23 : 1		86 : 1	159 : 1	411 : 1	636 : 1		1694 : 1	2548 : 1	3656 : 1	
2 Reduction absolute			576/25		14976/175	1587/10	359424/875	79488/125		1162213/686	7962624/3125	457056/125	
Order Number			233153		233159	233164	233169	233174		233182	233187	233192	
1 Reduction			28 : 1		103 : 1	190 : 1	456 : 1	706 : 1		1828 : 1	2623 : 1	4060 : 1	
2 Reduction absolute			138/5		3588/35	12167/64	89401/196	158171/224		2238912/1225	2056223/784	3637933/896	
3 Number of stages		1	2	2	3	3	4	4	4	5	5	5	5
4 Max. continuous torque at gear output	Nm	1	3	3	6	6	6	6	6	6	6	6	6
5 Intermittently permissible torque at gear output	Nm	1.25	3.75	3.75	7.5	7.5	7.5	7.5	7.5	7.5	7.5	7.5	7.5
6 Sense of rotation, drive to output		=	=	=	=	=	=	=	=	=	=	=	=
7 Max. efficiency	%	80	75	75	70	70	60	60	60	50	50	50	50
8 Weight	g	118	162	162	194	194	226	226	226	258	258	258	258
9 Average backlash no load	°	0.7	0.8	0.8	1.0	1.0	1.0	1.0	1.0	1.0	1.0	1.0	1.0
10 Mass inertia	gcm²	1.5	0.8	0.8	0.7	0.7	0.7	0.7	0.7	0.7	0.7	0.7	0.7
11 Gearhead length L1	mm	26.5	36.4	36.4	43.1	43.1	49.8	49.8	49.8	56.5	56.5	56.5	56.5

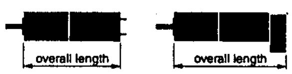

Combination:

+ Motor	Page	+ Tacho / Brake	Page	Overall length [mm]											
RE 25, 10 W	73			81.0	90.9	90.9	97.6	97.6	104.3	104.3	104.3	111.0	111.0	111.0	111.0
RE 25, 10 W	73	MR Encoder	201	92.0	101.9	101.9	108.6	108.6	115.3	115.3	115.3	122.0	122.0	122.0	122.0
RE 25, 10 W	73	DC-Tacho 22	213	103.4	113.3	113.3	120.0	120.0	126.7	126.7	126.7	133.4	133.4	133.4	133.4
RE 25, 10 W	73	Digital Encoder 22	203	95.0	104.9	104.9	111.6	111.6	118.3	118.3	118.3	125.0	125.0	125.0	125.0
RE 25, 10 W	73	Digital Encoder HED_ 55__	205/207	101.8	111.7	111.7	118.4	118.4	125.1	125.1	125.1	131.8	131.8	131.8	131.8
RE 25, 20 W	74			81.0	90.9	90.9	97.6	97.6	104.3	104.3	104.3	111.0	111.0	111.0	111.0
RE 25, 20 W	74	MR Encoder	201	92.0	101.9	101.9	108.6	108.6	115.3	115.3	115.3	122.0	122.0	122.0	122.0
RE 25, 20 W	74	DC-Tacho 22	213	103.4	113.3	113.3	120.0	120.0	126.7	126.7	126.7	133.4	133.4	133.4	133.4
RE 25, 20 W	74	Digital Encoder 22	203	95.0	104.9	104.9	111.6	111.6	118.3	118.3	118.3	125.0	125.0	125.0	125.0
RE 25, 20 W	74	Digital Encoder HED_ 55__	205/207	101.8	111.7	111.7	118.4	118.4	125.1	125.1	125.1	131.8	131.8	131.8	131.8
RE 25, 20 W	74	Brake 40	236	115.1	125.0	125.0	131.7	131.7	138.4	138.4	138.4	145.1	145.1	145.1	145.1
RE 26, 18 W	75			85.3	95.2	95.2	101.9	101.9	108.6	108.6	108.6	115.3	115.3	115.3	115.3
RE 26, 18 W	75	MR Encoder	201	96.3	106.2	106.2	112.9	112.9	119.6	119.6	119.6	126.3	126.3	126.3	126.3
RE 26, 18 W	75	DC-Tacho 22	213	106.3	116.2	116.2	122.9	122.9	129.6	129.6	129.6	136.3	136.3	136.3	136.3
RE 26, 18 W	75	Digital Encoder 22	203	102.7	112.6	112.6	119.3	119.3	126.0	126.0	126.0	132.7	132.7	132.7	132.7
RE 26, 18 W	75	Digital Encoder HED_ 55__	205/207	103.7	113.6	113.6	120.3	120.3	127.0	127.0	127.0	133.7	133.7	133.7	133.7
A-max 26	113-120			71.2	81.1	81.1	87.8	87.8	94.5	94.5	94.5	101.2	101.2	101.2	101.2
A-max 26	113-120	MR Encoder	201	32.3	42.2	42.2	48.9	48.9	55.6	55.6	55.6	62.3	62.3	62.3	62.3
A-max 26	113-119	Digital Magnetic Encoder 13	212	78.3	88.2	88.2	94.9	94.9	101.6	101.6	101.6	108.3	108.3	108.3	108.3
A-max 26	114-120	Digital Encoder 22	204	85.7	95.6	95.6	102.3	102.3	109.0	109.0	109.0	115.7	115.7	115.7	115.7
A-max 26	114-120	Digital Encoder HED_ 55__	206/208	89.6	99.5	99.5	106.2	106.2	112.9	112.9	112.9	119.6	119.6	119.6	119.6
RE-max 29	141-144			71.2	81.1	81.1	87.8	87.8	94.5	94.5	94.5	101.2	101.2	101.2	101.2
RE-max 29	141/143	MR Encoder	201	80.3	90.2	90.2	96.9	96.9	103.6	103.6	103.6	110.3	110.3	110.3	110.3

Twicell Sanyo Nickel-Metal Hydride Rechargeable Batteries SANYO

Cell Type HR-D

Specifications

Dimensions (with tube)

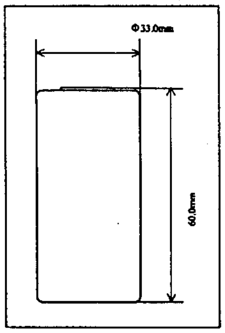

Type : Nickel-Metal Hydride Battery			Size : D
Capacity [1]		Typical	7500mAh
		Minimum	6900mAh
Nominal Voltage			1.2V
Charging Current x Time		Fast Charge [2]	mA x aboutHr.
Ambient Temperature	Charge	Fast Charge	C°
	Discharge Condition		0~50°C
	Storage Condition	~30days	-20~50°C
		30~90days	-20~40°C
		90days~1year	-20~30°C
Internal Impedance [3] (after discharge to E.V. = 1.0V)			About 3mOhms (at 1000Hz)
Weight [4]			About 172g
Size : (Diameter) x (Height)			33.0(D) x 60(H)mm

1) Charge
2) Use recommended charging system
3) After a few charge and discharge cycles under the aboe 1) condition
4) With tube

Typical Characteristics

Charge

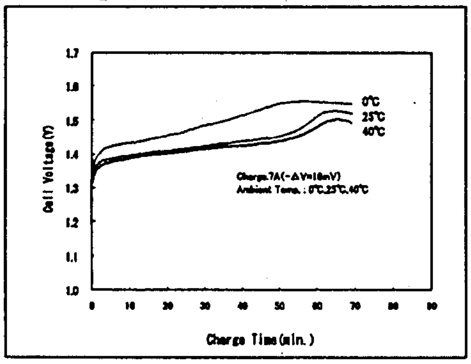

Discharge